Adjustment of Swelling Characteristics of Hydrogels via Microstructural Control Assisted by Droplet-Based Microfluidics

Dissertation

zur Erlangung des Grades „Doktor der Naturwissenschaften“ im Promotionsfach Chemie

am Fachbereich Chemie, Pharmazie, Geographie und Geowissenschaften
der Johannes Gutenberg-Universität Mainz

Torsten Gereon Linder
geboren in Böblingen

Mainz, 2024

Die vorliegende Arbeit wurde im Zeitraum vom Juli 2020 bis November 2024 im Rahmen des von der Deutschen Forschungsgemeinschaft (DFG) geförderten Graduiertenkollegs GRK 2516 „Structure Formation of Soft Matter at Interfaces“ im Arbeitskreis von Herrn Prof. [redacted] [redacted] am Department Chemie der Johannes Gutenberg-Universität Mainz angefertigt.

1. Gutachter: [redacted]
2. Gutachter: [redacted]

Tag der mündlichen Prüfung:

Eigenständigkeitserklärung

Hiermit versichere ich, Torsten Gereon Linder, dass ich die vorliegende Arbeit selbstständig verfasst und keine anderen als die angegebenen Quellen und Hilfsmittel benutzt habe. Ich erkläre ferner, dass ich keine KI-basierten Anwendungen oder Werkzeuge genutzt habe. Sämtliche wörtlichen oder sinngemäßen Übernahmen und Zitate sind kenntlich gemacht und nachgewiesen. Ich versichere, dass ich keine Hilfsmittel verwendet habe, deren Nutzung die Prüferin oder der Prüfer explizit ausgeschlossen hat. Mit Abgabe der vorliegenden Leistung übernehme ich die Verantwortung für das eingereichte Gesamtprodukt. Die Richtigkeit übernommener Aussagen und Inhalte habe ich nach bestem Wissen und Gewissen geprüft. Mir ist bekannt, dass ein Verstoß gegen die genannten Punkte prüfungsrechtliche Konsequenzen hat und insbesondere dazu führen kann, dass die Promotionsleistung als mit „nicht bestanden" bewertet wird. Die Einschreibung kann für bis zu zwei Jahre widerrufen werden, wenn Studierende zweimal oder häufiger bei Prüfungsleistungen täuschen (§ 69 Abs. 4 und 5 HochSchG).

____
(Ort, Datum)

____
(Unterschrift)

„Research means that you don’t know,

but are willing to find out.”

— Charles F. Kettering —

Danksagung

Zuallererst geht ein großer Dank an [redacted] für das interessante Forschungsthema und seine große persönliche und fachliche Unterstützung bei den Herausforderungen der unterschiedlichen Projekte.

Des Weiteren geht ein großer Dank an [redacted] für das Übernehmen der Zweitkorrektur und für seine Bereitschaft jederzeit zu wissenschaftlichen Diskussionen zur Lösungshilfe.

Beim Arbeitskreis [redacted] will ich mich auch herzlich bedanken, bei [redacted] für ihre stets gute Laune und ihren administrativen Support, der jederzeit zur Verfügung stand. Bei [redacted] für all die Hilfe bei den Besorgungen von Labormaterialien des Alltags und bei [redacted] für den technischen Support und der stetigen guten Laune und den aufmunternden Worten. Unserem akademischen Rat [redacted] für den wissenschaftlichen Support und die mutmachenden Gespräche. Vielen Dank auch an alle aktuellen und ehemaligen Mitglieder der Arbeitsgruppe, insbesondere [redacted] für deine Einführung in die Mikrofluidik, deine stete Bereitschaft zu helfen und die mutmachenden Worte, wenn die Mikrofluidik ihren Launen freien Lauf ließ. Des Weiteren möchte ich mich herzlich bedanken bei dem Chaosbüro / der Holzklasse, namentlich [redacted], für all die unvergesslichen und sprachlos machenden Momente sowohl beim Mittagsessen als auch im täglichen Verlauf, die so manch eine Reality TV-Show in den Schatten stellen konnten. Eure stets aufmunternden Worte milderten so manchen Rückschlag in der Forschung und gaben mir stets Kraft weiter zu machen. Auch [redacted] will ich besonders danken für ihre Hilfe und Zusammenarbeit bei den unterschiedlichen Projekten der Arbeit.

Den Mitgliedern des GRK 2516 will ich danken, für den Support und die schöne gemeinsame Zusammenarbeit, im Besonderen [redacted], meinem GRK-Partner für die gute Zusammenarbeit und die große Hilfe beim Verstehen der Simulationen innerhalb des Projektes und seine große Hilfe beim Erlernen des Programmierens mithilfe von Python. Ein großer Dank geht auch an [redacted] für die unvergesslichen Abende bei der ECIS 2022.

Auch will ich mich bei [redacted] für all die Unterstützung über die Jahre bedanken, den Rückhalt den ihr mir stets gabt und die aufmunternden Worte, wann immer ich sie brauchte. Bei [redacted] für die vielen Grillabende und entspannenden Zeiten bei hohen Temperaturen im kalten Pool.

Bei allen Korrekturlesenden dieser Arbeit will ich mich zusätzlich bedanken für all eure Mühen. Der Deutschen Forschungsgemeinschaft (DFG) will ich meinen Dank ausdrücken, für ihre finanzielle Unterstützung.

Allgemeine Anmerkungen

Die nachfolgende Arbeit ist gegliedert in eine theoretische Einführung, in der der wissenschaftliche Hintergrund und die verwendeten Analysemethoden beschrieben werden, eine Zielsetzung und einen wissenschaftlichen Hauptteil mit abschließender Zusammenfassung und Fazit. Im wissenschaftlichen Hauptteil werden drei Projekte sowie zwei Nebenprojekte beschrieben.

Die Arbeit beschäftigt sich hierbei projektübergreifend mit der Technik der tröpfchenbasierten Mikrofluidik und deren Optimierung sowie in insgesamt drei Hauptprojekten mit der Herstellung unterschiedlicher Hydrogel-Mikropartikel und deren Charakterisierung.

Das Projekt II (Kapitel 4 – 7) wurde im Rahmen des GRK 2516 „Structure Formation of Soft Matter at Interfaces“ durchgeführt. Das GRK 2516 besteht aus vier Teilprojekten: Teilprojekt A – Nanopartikel, Teilprojekt B – Supramoleküle, Teilprojekt C – Suprapartikel und Teilprojekt D – Mikropartikel. Das Projekt II beschreibt dabei die Arbeit im Teilprojekt D, welches zusammen mit dem Partner aus der Theorie [redacted] angefertigt wurde.

Die Ergebnisse des Projekts III (Kapitel 8), welches sich mit dem Einfluss der Hydrophobie des Vernetzers auf das Quellverhalten der Hydrogele beschäftigt, wurden bereits unter Macromol. Chem. Phys. 2024, 225, 2400138 (doi: 10.1002/macp.202400138) publiziert und mit Erlaubnis der Autoren und des Verlags in dieser Arbeit adaptiert.

Zusätzlich zu den Hauptprojekten werden im Kapitel 9 zwei kleinere Nebenprojekte dargestellt, wobei hervorzuheben ist, dass Kapitel 9.1 die Ergebnisse des Projekts III um eine strukturelle Betrachtung der entsprechenden Hydrogele komplementiert.

Zusammenfassung

Die Eigenschaften von Hydrogelen werden bestimmt durch ihre Synthesemethode und Zusammensetzung. Als Synthesemethode wird in dieser Arbeit die tröpfchenbasierte Mikrofluidik verwendet, da mit ihr monodisperse Hydrogel-Mikropartikel von sogenannten „Designer-Emulsionen“ synthetisiert werden können. Diese Mikropartikel können dann auf das Zusammenspiel von Zusammensetzung und Eigenschaften hin untersucht werden.

Ein entscheidender Nachteil der tröpfchenbasierten Mikrofluidik ist die geringe Ausbeute an Mikrogelen der Methode. Diese wird hauptsächlich durch die Flussraten der beiden Phasen durch die Mikrofluidik-Einheit, in der die Emulsion entsteht, bestimmt. Daher wird im ersten Teil dieser Arbeit ein existierender Mikrofluidik Experimentalaufbau modifiziert, in dem die Mikrogele mithilfe eines Fotoinitiators und UV-Strahlung hergestellt werden. Je nach Initiierung der Polymerisationsmethode (thermisch- oder foto-initiiert) müssen entsprechende Teile des Aufbaus modifiziert und optimiert werden.

Im zweiten Teil dieser Arbeit liegt der Fokus auf der Synthese von Kern-Schale Partikeln, mit einem temperatursensiblen Kern und einer nicht temperatursensiblen Schale, deren Konnektivität variiert. Hierfür werden in einem ersten Schritt Poly(*N*-isopropylacrylamid) Mikropartikel mithilfe der tröpfchenbasierten Mikrofluidik als spätere Kerne für die Kern-Schale Partikel synthetisiert. Zur Synthese werden unterschiedliche Mikrofluidik-Einheiten genutzt, um möglichst monodisperse Partikel in ausreichender Menge zu erhalten. Zudem wird untersucht, ob die erhaltenen Mikropartikel als Kerne verwendbar sind. Als Analysemethode wird die optische Mikroskopie verwendet.

Anschließend wird auf die Synthese des Schalenvorläuferpolymers eingegangen. Dieses ist ein Copolymer aus Acrylamid (AAm) und *N*-(2-(3,4-dimethyl-2,5-dioxo-2,5-dihydro-1H-pyrrol-1-yl)ethyl)acrylamid (DMMIAAm). DMMIAAm dient der späteren Vernetzung der linearen Polymerketten mithilfe von UV-Strahlung in Gegenwart von Thioxanthone-2,7-disulfonate (TXS), einem Fotosensibilisator, der ebenfalls als Teil dieser Arbeit synthetisiert wird.

Nachdem sowohl die Kerne, als auch das Schalenvorläuferpolymer vorbereitet sind, wird im Anschluss die Kern-Schale Partikelsynthese mithilfe der tröpfchenbasierten Mikrofluidik fokussiert. Hierbei werden die Herausforderungen der Synthese ermittelt und gelöst. Des Weiteren, werden Aufbaumodifikationen entwickelt, um die Vernetzung von Kern und Schale zu kontrollieren. In diesem Zusammenhang wird auch die Diffusion von linearen Ketten in ein

Polymernetzwerk, im Rahmen eines Tandemprojekts mit [redacted], simuliert. Hierbei steht im Fokus der Diffusionsmechanismus für ein besseres Verständnis dessen und die Entwicklung weiterer Ideen, wie die Konnektivität von Kern und Schale kontrolliert werden kann.

Im dritten Teil der Arbeit liegt der Fokus auf Mikrogelen aus vernetzter Poly(acrylsäure) und dem Einfluss der Hydrophobie des Vernetzers auf deren Quellkinetik. Hierfür werden zunächst mithilfe der Mikrofluidik Mikrogele synthetisiert, da hierdurch der Einfluss der Synthesemethode auf die Gelnetzwerkbildung minimiert wird. Nach der Synthese werden die Mikrogele mit den verschieden hydrophoben Vernetzern in Quellkinetik-Versuchen analysiert. Um sicherzugehen, dass die Vernetzer auch ähnlich in das Polymernetzwerk eingebaut werden, werden zudem von den Vernetzer-analogen n-Alkylacrylamiden die Co-Polymerisationsparameter bestimmt.

Der letzte Teil der Arbeit behandelt zwei kleinere Seitenprojekte. Unter anderem Lichtstreuversuche an Makrogelen derselben Zusammensetzung wie die der Mikrogele aus dem vorherigen Teil. Hierbei liegt der Fokus auf der Bestimmung der Heterogenität der Gele. Im zweiten Seitenprojekt wird ein Mikrofluidik Aufbau für die Synthese von Carbomer974p-Agarose Hydrogelen vernetzt mit Hyaluronsäure erstellt. Hierbei bestand die Herausforderung in der Erwärmung signifikanter Teile des experimentellen Aufbaus auf ca. 80 °C mit möglichst geringen Temperaturschwankungen, da diese den Versuch scheitern lassen würden.

Abstract

The properties of hydrogels result from both the synthesis method and their composition. In the present work droplet-based microfluidics is used as the main synthesis method. It allows the creation of monodisperse hydrogel microparticles from designed emulsions. These hydrogel microparticles can in the following be investigated to determine the interplay of the composition and properties of the resulting hydrogel microparticles.

Nonetheless, one major drawback of droplet-based microfluidics is its output. Which is mainly determined by the flowrates of the two fluids through the microfluidic device, creating the emulsion. Thus, in the first part of this work an existing microfluidic experimental setup is modified to maximize the yields. To polymerize the droplets a photo-initiator and UV-radiation is used, thereby determining the area of improvement in the microfluidic setup.

The second study focuses on the creation of core-shell particles with a temperature sensitive core and a temperature non-sensitive shell with different degrees of interconnectivity of the two. Therefore, in a first step thermo-responsive poly(*N*-isopropylacrylamide) microgels are synthesized via droplet-based microfluidics, which are later used as cores in core-shell particles. To gain monodisperse core-particles in sufficient quantities different microfluidic setups are investigated. The resulting cores are analyzed concerning their usability for the synthesis of core-shell particles with a controlled interface between core and shell. For the analysis of the cores optical microscopy is used.

As shell-precursor polymer a linear copolymer, made of acrylamide (AAm) and *N*-(2-(3,4-dimethyl-2,5-dioxo-2,5-dihydro-1H-pyrrol-1-yl)ethyl)acrylamide (DMMIAAm) is synthesized. DMMIAAm allows the controlled crosslinking of the linear shell-precursor polymer via UV-irradiation in the presence of the photosensitizer thioxanthone-2,7-disulfonate (TXS) which is also synthesized as part of this work.

After successful preparation of core-particles and shell-precursor polymer the core-shell synthesis using droplet-based microfluidics is focused on. Challenges during the synthesis of the core-shell particles are identified and resolved. Furthermore, methods are developed to gain control over the interpenetration depth of the shell and core. Lastly diffusion simulations of linear polymer strands into a polymer gel network are analyzed in a tandem-project with [redacted] [redacted] to gain insight into the diffusion mechanism and further ideas on how to control the interface between core and shell.

In the third part of the thesis the focus shifts to microgels made of crosslinked poly(acrylic acid) containing different hydrophobic crosslinkers. The microgels are synthesized using droplet-based microfluidics to keep the influence of the synthesis method on the polymer network as minimal as possible. In swelling experiments, the effect of the hydrophobicity of the crosslinker on the swelling kinetics of the microgels is then analyzed. To further ensure the comparability of the different microgel crosslinkers the reactivity ratios of the corresponding n-alkyl acrylamides are determined.

The last part of the thesis presents two side-projects. The first of which is about light scattering experiments done on macro gels with similar composition, as the microgels of the previous part to determine the heterogeneity of the different gels.

In the second side-project a microfluidic experimental setup for the synthesis of carbomer974p-agarose hydrogels crosslinked with hyaluronic acid is developed. Since the polymerization reaction is initiated prior to the start of the microfluidic experiment it poses a unique challenge to the experimental setup.

Table of contents

1. Theoretical Background

1.1 A brief look into the history and impact of hydrogels

Whilst usually the time when humans first started to use certain items or aspects can be determined quite well, in the case of hydrogels this proves to be a lot more difficult. The challenge hereby lies in the natural examples of hydrogels as for example gelatin.[1] Its use can be detected for thousands of years all around the world. Used often for example as glue for pigments in both ancient Rome and Greece or as ingredient in ancient Chinese medicine.[2] Even the origin of the name collagen can be traced back to the ancient Greek word “κόλλα”.[2] The term “hydrogel” itself was first used by Lee, Kwon and Park in 1894, describing in their publication colloidal gels made with inorganic salts.[3] Non-natural polymer hydrogels on the other hand took until 1936 to be published for the first time by scientists of DuPont.[4] However, though mentioning poly(2-hydoxyethyl methacrylate) (polyHEMA) they regarded it as unimportant. This changed in 1960 when Wichterle and Lim rediscovered polyHEMA describing it as a soft water swollen polymer,[5] further describing already first steps into the fields of biomedical applications.[5]

Since 1960, the research into hydrogels has significantly increased both on natural hydrogels as for example collagen and hyaluronic acid to name a few as well as synthetic hydrogels as poly(acryl amides) or poly(ethylene glycol). Further the fields of application of hydrogels also have significantly increased including the aforementioned biomedical applications with products as for example Gengigel® by Oraldent Ltd. containing Hyaluronan[6], but also farming, where hydrogels are used both as water-holding reservoirs as well as for nutrient mobilisation.[7] Further fields of applications are hygiene products as for example Pampers® Baby Dry™[8] and even building applications as cement additives[9] are being researched on.

The term “hydrogel” was defined in 2007 by the International Union of Pure and Applied Chemistry (IUPAC), as a polymer network “in which the swelling agent is water”[10], which though in essence extremely broad is today used in most publications about the topic.

Whilst in the IUPAC definition of hydrogels there is no mentioning of the shape of the hydrogel, in many applications hydrogels are in the form of microgels. The term microgel, first introduced by W. J. Elford in 1930[11], is defined by IUPAC as “particles of gel of any shape with an equivalent diameter of approximately 0.1 to 100 µm”.[10] This definition is mostly to distinguish microgels from nanogels which have diameters from 1 to 100 nm.[10] In the following the focus is on the different synthesis methods for hydrogels in the form of microgels. With one being a top-down approach and the other bottom-up approaches.

1.1.1 Microgel synthesis via ball milling

Also known as a top-down approach, one method to synthesize microgels is the milling of larger gels down to microgel sizes. As the polymer gel is milled the polymer-chains are torn, with the degradation rate of the polymer in ball milling experiments dependent on the probability of chain scission, i.e., the probability of polymer being captured between the colliding balls and the rate at which the balls within the mill collide. Increasing the mass of polymer within the mill does not increase the rate due to the powder cushioning effect.[12,13] As the scission of polymer chains takes place an unwanted side effect can alter the properties of the gel itself. For example, in the case of the lower critical solution temperature (LCST) of poly(*N*-isopropylacrylamide) (poly-NIPAM), which was found to be differently influenced, once increasing and one time decreasing, by the milling process in two publications.[12,14]

Furthermore, the particles resulting from this top-down approach do not have a uniform shape, instead, jagged shapes of all sizes are obtained.[15]

1.1.2 Microgel synthesis via emulsion polymerization

In contrast to a top-down approach, the emulsion polymerization is a bottom-up approach.[16] This means that the polymer is built from the monomers up, therefore allowing control over the colloidal and physical properties of the microgels.[17] During an emulsion polymerization a solution of the monomer is emulsified in a non-miscible second phase. The emulsion polymerization itself can hereby be divided into three separate intervals. During the first interval of the polymerization the particle nucleation takes place. To achieve a narrow particle size distribution, the nucleation interval should be kept as short as possible with the conversion of the monomer between 0 – 5% as the growth rate of smaller droplets is increased in comparison to larger droplets. Thus, the particle size distribution also is the largest at the end of this initial interval. During the second interval the polymerization rate remains constant as monomer droplets are used up growing the polymer gels. Once the droplets are used up, usually at around 40% conversion, the final interval of the emulsion polymerization starts. During this interval the polymerization rate decreases continuously until the monomer is completely used up.[17,18]

One big advantage of the emulsion polymerization, besides monodisperse particles sizes, is the transfer of the reaction heat to the surrounding phase. However, one drawback is the occurrence of auto-acceleration during the last step especially for the homo-polymerization of acrylates. A further limitation of the emulsion polymerization is that in order to obtain narrow size distributions the second and third intervals are necessary, thus limiting the minimum particle size.[18]

1.1.3 Microgel synthesis via droplet-based microfluidics

Similarly to the previously described emulsion polymerization, droplet-based microfluidics is a bottom-up method, allowing the creation of microgels from emulsions.[16] The main aim of the method is the creation of emulsions,[19,20] a colloidal system with one liquid dispersed in a second liquid.[10] As the design of the microfluidic setup determines the resulting emulsion the term designer emulsion can be used.[19,20] Due to this advantage in controlling the resulting emulsion, droplet-based microfluidics will be the main method used in this work.

1.1.3.1 Basic idea and design of droplet-based microfluidics

As mentioned, the basic idea of droplet-based microfluidics is the creation of a designer emulsion. Therefore at least two fluids are pumped through a system of microchannels and meet at an intersection. At the intersection shear forces between the two fluids lead to the segmentation of one of the fluids, the so-called dispersed phase in a surrounding phase called the continuous phase.[20,21] As important factors for the droplet formation in microfluidics can be made time constant, the size distribution of the droplets in microfluidics is very narrow.[20] Three designs are generally used in droplet-based microfluidics, as depicted in **figure 1.1**.

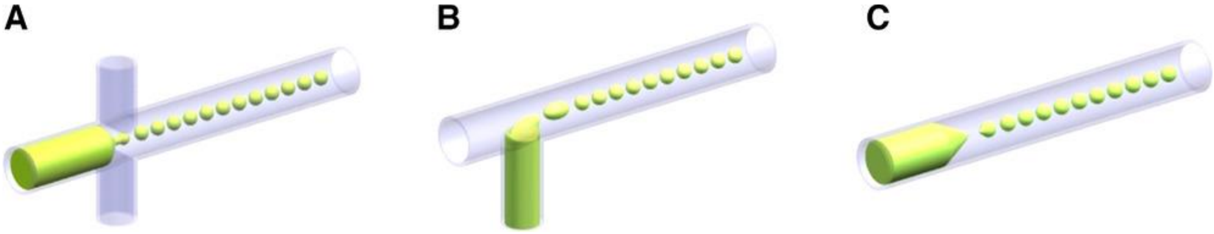

Figure 1.1: Different versions of microfluidic devices with the dispersed phase in green and the clear continuous phase. (A) depicts the flow-focusing device. (B) is a T-junction device and (C) depicts the co-flow device setup. [22]

The flow-focusing microfluidic device setup (figure **1.1A**) is among today's most popular devices. It consists of a simple cross-junction with the dispersed phase entering from the left and the continuous phase entering from the top and bottom. Its main advantage is the maximization of the shear forces between the two immiscible fluids making it easier to tone and control the droplet sizes.[22]

Figure **1.1B** depicts the T-junction microfluidic setup in which the dispersed phase is forced into a flow of the continuous phase. T-junction devices are usually used for low viscosity dispersed phases, as a high viscosity dispersed phase is prone to create unwanted satellite droplets with this setup.[22]

The final common design of a microfluidic setup is the co-flow design (figure **1.1C**). In this case, both the continuous and the dispersed phase enter the device from the same direction, with the dispersed phase enclosed by the continuous phase at the junction.[22]

Whilst each of the designs from figure 1.1 can produce simple emulsions, droplet-based microfluidics is not limited to these. For example, by chaining multiple devices more complex double emulsions can be created. An example would be two flow-focusing devices in a row as shown in **figure 1.2**.

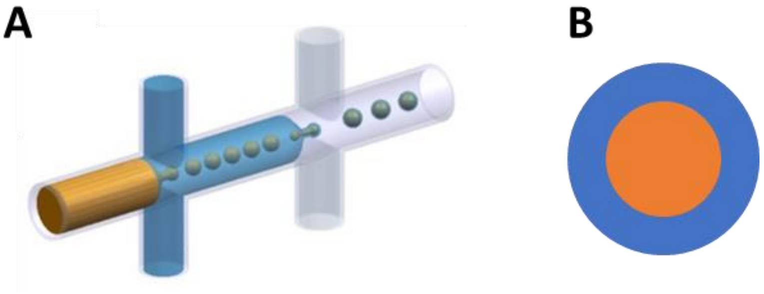

Figure 1.2: Double emulsion flow focused microfluidic setup, with a first dispersed phase in orange forming droplets in the second dispersed phase colored blue. At the second cross-section double emulsion droplets are created containing the first dispersed phase in the core and the second dispersed phase as a shell (A). (B) depicts a cross-section of the resulting double emulsion of the droplet-based microfluidic setup A.[22]

Regardless of the droplet-based microfluidic design used, the critical part of microfluidics is the droplet formation, the theoretical background of which is the subject of the following.

1.1.3.2 Theoretical background of the droplet formation

The droplet formation in microfluidics can be described using three dimensionless quantities known as the Reynolds number (*Re*), the Capillary number (*Ca*), and the Weber number (*We*). The first describes the flow type in microfluidics, whilst the latter two determine the behavior of the droplet formation.[20,23,24]

The Reynolds number *(Re)* delimits and quantifies the different types of fluid-flow in microfluidics. Its equation is:[20]

$$Re = \frac{\text{inertial forces}}{\text{viscous forces}} = \frac{\rho \cdot v_x \cdot L_0}{\eta} \tag{1.1}$$

With ρ the fluid density, v_x the flow speed in a specific direction, here *x*, L_0 the characteristic size over which the interplay interaction of the inertial and viscous forces is to be calculated, in microfluidics this in most cases is the channel diameter, and η being the dynamic viscosity.

Reynolds numbers beneath 250 indicate a laminar flow, while Reynolds numbers of above 2300 usually indicate turbulent flows in pipeline-type systems. In the case of microfluidics, the Reynolds number are in the range of 10^{-6} to 10^{1}, suggesting that the viscous forces outweigh the inertia, leading to laminar flows with a parabolic radial profile also known as Poiseuille flow, due to drag. The Poiseuille flow is the usual velocity profile in microfluidics.[20]

In microfluidics, the droplet creation is often determined by a combination of shear and pressure effects. The behavior of the droplet formation can be determined by both the Capillary number (*Ca*) and the Weber number (*We*). The Capillary number relates to the shear forces on the dispersed phase by the continuous phase to its surface tension. Mathematically, it can be expressed as:[20]

$$Ca = \frac{\text{viscous forces}}{\text{interfacial tension}} = \frac{\eta \cdot v_\mathrm{x}}{\gamma_\mathrm{IF}} \tag{1.2}$$

With η as the dynamic viscosity, v_x the fluid flow speed in direction x and γ_IF the interfacial tension.

The Weber number in contrast, reflects the balance of the inertial forces of the dispersed phase pushing the droplet forward and the surface tension resisting this flow. Its equation is:[20]

$$We = \frac{\text{interfacial forces}}{\text{surface tension}} = \frac{\rho \cdot v_\mathrm{x}^2 \cdot L_0}{\gamma_\mathrm{IF}} \tag{1.3}$$

To obtain the desired mono-disperse emulsions in microfluidics both the Capillary and Weber number, as well as their sum, should be below one. In this case, droplets are continuously created and a balance between the interfacial forces of the forming droplet and the shear forces of the continuous phase exists. In this case the radius of a droplet can be expressed using the Capillary number as follows.[20]

$$r_\mathrm{droplet} = \frac{\gamma_\mathrm{IF} \cdot h}{\eta \cdot |v_\mathrm{x}|} = \frac{h}{Ca} \tag{1.4}$$

With *h* being the height of the microchannel.

However, if the Capillary or Weber number or its sum approximates one, jetting may occur as depicted in the following image.

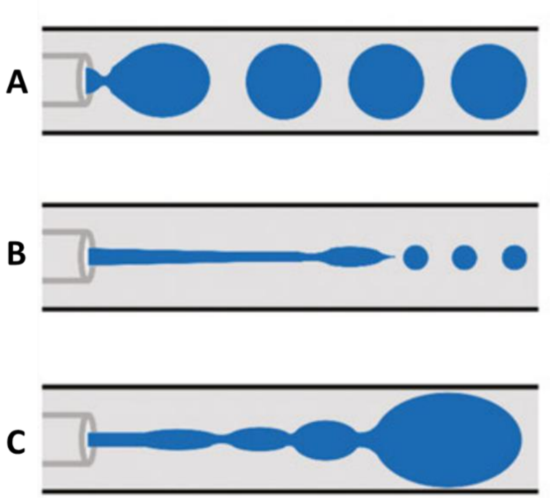

Figure 1.3: Droplet formation in microfluidics. (A) shows optimal droplet creation, while both (B) and (C) show jetting of the dispersed phase.[20]

There are two different reasons for jetting. In the first case, the jet is formed by the flow rate of the continuous phase exceeding a critical limit, thereby decreasing the droplet size of the dispersed phase until a thin jet is created at the tip of which the droplet breakup occurs (see figure **1.3B**).[20]

The second reason for jet-formation is an increase in the flow rate of the dispersed phase over a critical limit. In this case the jet also eventually breaks up into droplets, due to the Rayleigh-Plateau instability, which is driven by the surface tension's drive to minimize the surface area. This drive alongside tiny perturbations in liquid jets, which in some cases grow into sinusoidal waves, finally pinches off droplets. (see figure **1.3C**)[20]

Both cases are unwanted in droplet-based microfluidics as the two jetting effects lead to significant decreases in the mono-dispersity of the resulting droplets of the emulsion.

1.1.3.3 Droplet stabilization in droplet-based microfluidics

Once the droplets of an immiscible dispersed phase are formed in the continuous phase the microfluidic emulsion is created. Compared to a fully separated two-phase system, the interfacial area between the two phases is enlarged. Thus, an emulsion is an out-of-equilibrium system, meaning the system will try to reach equilibrium by minimizing the interfacial area again. This is achieved through the coalescence of the droplets into larger drops.[20]

To counteract the coalescence of the droplets, which impedes the microfluidics aim of creating designer emulsions, surface active agents, or in short surfactants are used to stabilize the emulsions.[25,26] In general, a surfactant is a molecule containing a hydrophilic part, often regarded as the head group, and a hydrophobic part, made up of a hydrocarbon or fluorocarbon chain. Depending on the type of hydrophilic head, surfactants can be distinguished into four distinct groups as depicted in **figure 1.4**.[20]

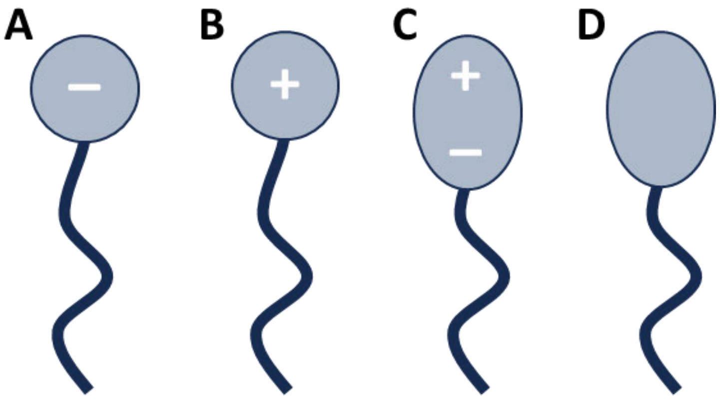

Figure 1.4: Four different classes of surfactants each one containing a hydrophilic head (grey circle) and a hydrophobic tail (black line). Surfactants (A) and (B) are both ionic surfactants. Surfactants depicted in (C) are called amphoteric surfactants and contain both a negative and a positive charge. (D) is a schematic of a non-ionic surfactant.[20]

Among the charged surfactants depicted in figure 1.4 are the cationic **1.4B** and the anionic **1.4A** surfactants. In the case of anionic surfactants, the hydrophilic head is often composed of a deprotonated acid or sulfate group, while cationic head groups most commonly are positively charged quaternary ammonium groups. In the case of amphoteric surfactants **1.4C**, the head group contains both a positive as well as a negative charge and in the case of nonionic surfactants **1.4D** no charge is in the hydrophilic head group and instead a hydrophilic polymer for example is used.[20]

Independently of which surfactant is used, a surfactant stabilizes an emulsion in two ways. Firstly, it reduces the surface tension of the corresponding droplets. This effect increases with the concentration of the surfactant until the critical micelle concentration (CMC) is reached. At the CMC the surface area between the dispersed and the continuous phase is covered with the surfactant. Once the CMC is surpassed micelles will form and no further lowering of the surface tension is possible.[20,26]

Secondly surfactants can hinder the coalescence of the droplets for steric reasons, for example in the case of hydrophilic droplets in a hydrophobic continuous phase or due to electrostatic repulsion in the case of hydrophobic droplets in a hydrophilic continuous phase (see **figure 1.5**).[26,27]

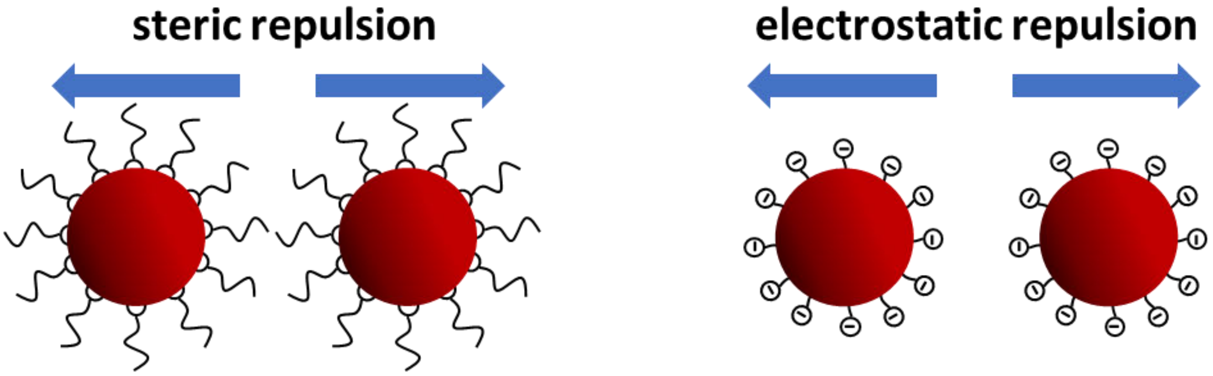

Figure 1.5: On the left, the steric repulsion of the surfactants hinders particle coalescence, while on the right the charge of the surfactant leads to particles not coalescing.

Besides the coalescence of the droplets, the Ostwald ripening effect can further decrease the mono-dispersity of the droplets in a microfluidic emulsion. During Ostwald ripening, the interfacial area is reduced as smaller particles disappear and their material is added to larger droplets through diffusion of the dispersed fluid through the continuous phase. This effect can be reduced if the solubility of the dispersed phase is virtually nonexistent in the continuous phase or by using additives, which are insoluble in the other phase and exert osmotic pressures counteracting the Oswald ripening.[20,28]

1.1.3.4 Microfluidic device fabrication

At the time of their invention, microfluidic devices were often made of silicon quartz or glass materials with channels etched into the materials.[29–33] This made the fabrication of microfluidic devices expensive and time-consuming. Today, most microfluidic devices are composed of poly(dimethylsiloxane) silicone or, in short, PDMS, which is commercially available as a kit from Sylgard®, reducing the cost and time of device fabrication.[20,34] In the following the device fabrication using PDMS and glass capillaries will be discussed in more detail.

One common method of creating microfluidic devices made of PDMS is by using photolithography. This method depicted in **figure 1.6** involves multiple steps. In the first step, a thin layer of photoresist is spread on a silicon wafer (substrate) via spin coating, for example. An example of a photoresist is SU-8, containing a bisphenol A Novolak epoxy with eight reactive epoxy functionalities for polymerization.[34,35] The thickness of the photoresist hereby defines the later height of the microfluidic channels. Therefore, it is crucial to have both a defined and uniform photoresist thickness. After evaporation of the photoresist solvent during soft baking of the wafer at 95 °C, a photomask of the microfluidic device is put on top, and the non-covered photoresist is polymerized via UV-radiation. Following a further post baking of the silicon wafer, the unpolymerized photoresist is removed to obtain the microfluidic master device. The photomask thereby determines both the overall shape of the microfluidic channels and the channel width of the microfluidic master. This master is then covered with the PDMS mixture and the PDMS is cured. Once fully cured, the PDMS-slab can be cut and peeled from the master. After punching holes through the PDMS as access points to connect the device with the rest of the experiment, the PDMS is sealed against a glass surface using plasma activated bonding. The microfluidic device is ready for use once the PDMS is bonded to the glass.[20,34]

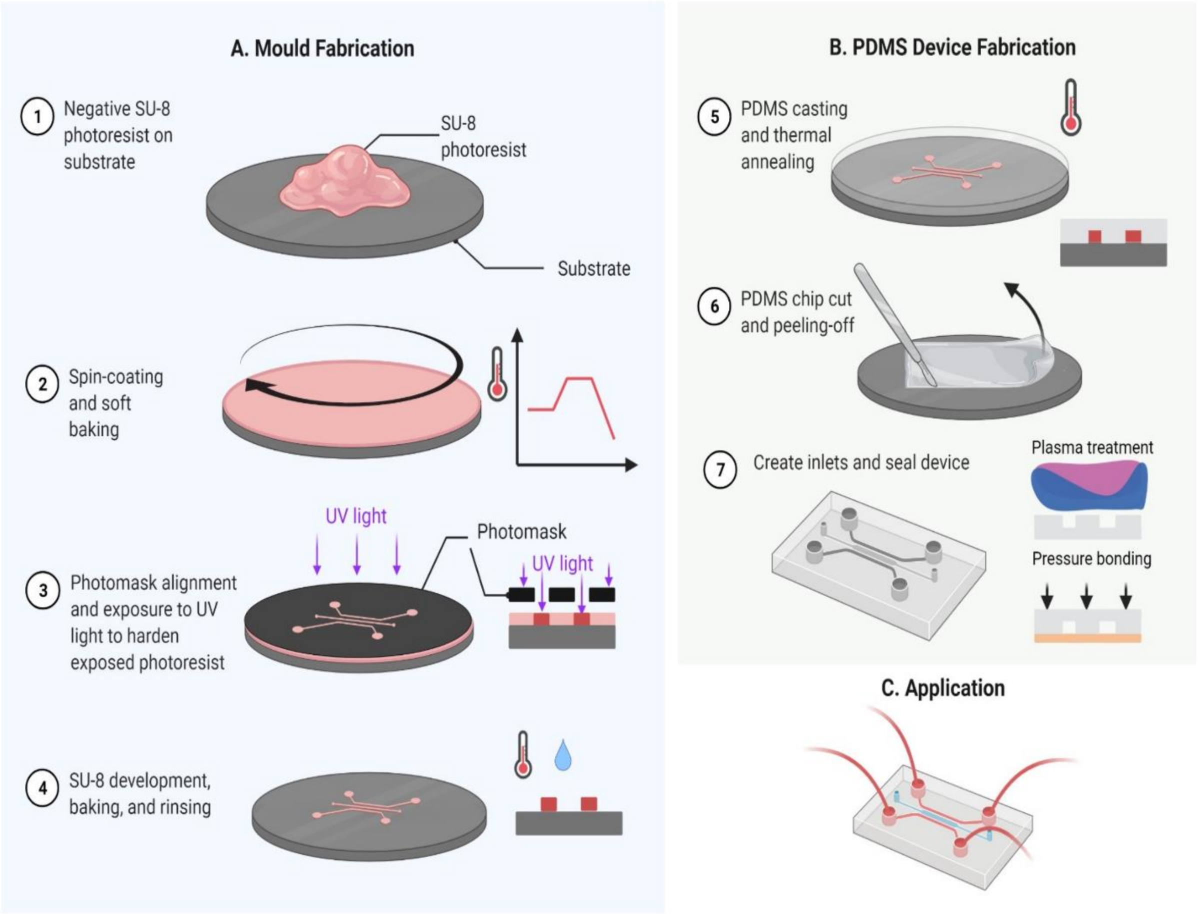

Figure 1.6: Photolithography method to create a PDMS device. On the left the microfluidic master is first created, with which afterwards PDMS devices are fabricated in several steps as shown on the right.[34]

PDMS microfluidic devices employ many advantages among which are the possibility to create many different types of setups using corresponding photomasks. Furthermore, multiple microfluidic setups can be placed next to one another on the master as backups if one setup may be clogged. It is also possible to reuse the master after the PDMS is peeled off to create further microfluidic devices.[20]

Despite all these advantages, there are also some disadvantages that can limit the usefulness of PDMS microfluidic devices. One major disadvantage is that many organic solvents can swell

PDMS, making them unsuitable for microfluidic experiments due to channel size deformation. Possible further reasons for channel deformations can be the overall softness of PDMS, especially at high aspect ratios of the design. Further, it is challenging to make PDMS devices with a three-dimensional flow profile (see figure **1.1C**), meaning the dispersed phase is equally influenced by the continuous phase on all sides during the droplet creation, as such a three-dimensional flow would require masters with different height profiles for the corresponding channels.[20,34]

Using glass microcapillaries to make microfluidic devices can circumvent these disadvantages. To fabricate a glass-capillary microfluidic device, a circular glass capillary with a tapered geometry is made using a pipette puller. The circular capillary is carefully inserted into a square capillary with a slightly larger inner diameter than the outer diameter of the circular capillary. To connect the microfluidic device with the rest of the experiment, syringe tips are placed at the inlets of the corresponding capillaries, and the device is placed on a glass slide and sealed using epoxy glue. Depending on the arrangement of the glass capillaries it is possible, to make co-flow or flow-focusing devices or even combinations thereof (for reference see **figure 1.7**).[20]

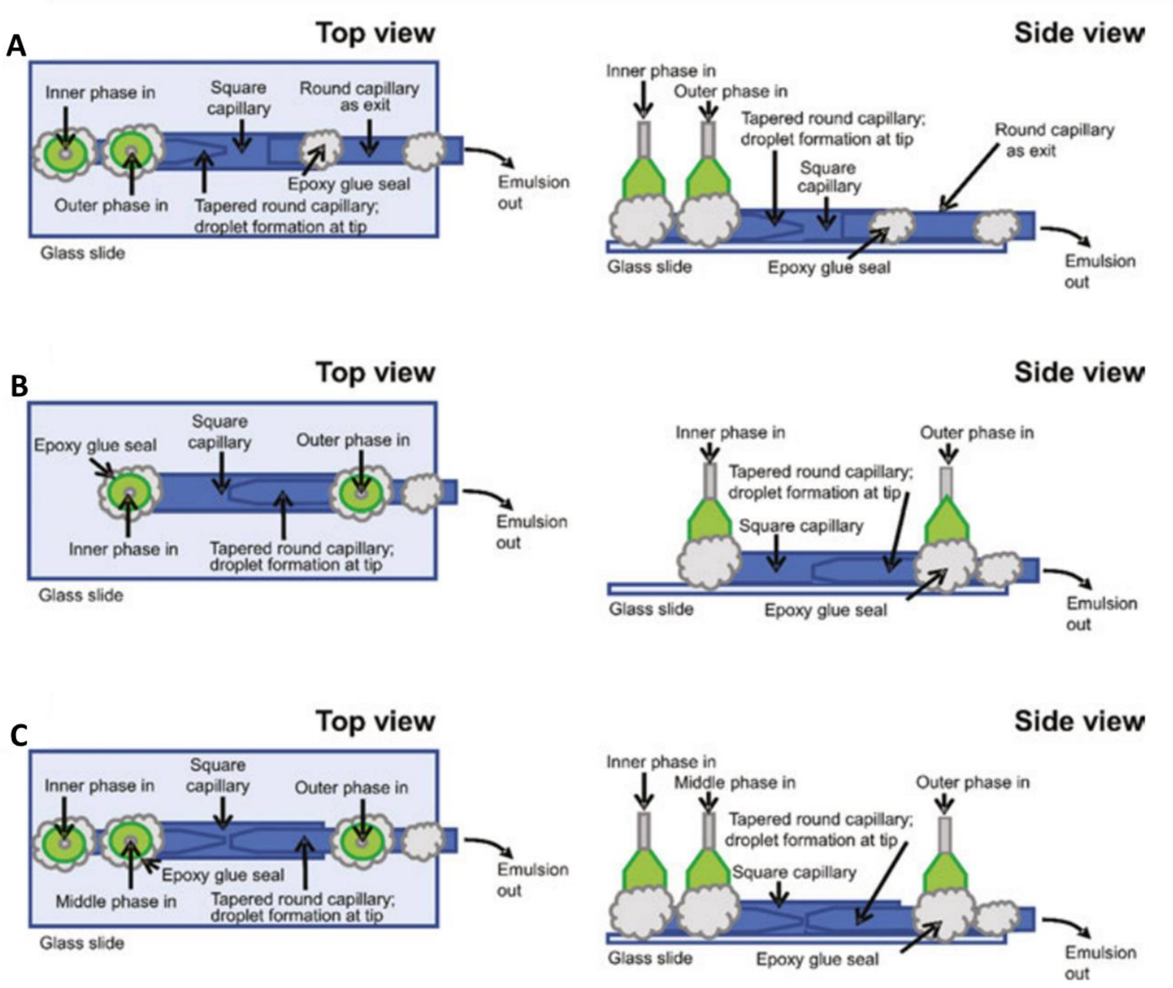

Figure 1.7: Design variations of glass microfluidic devices, with a co-flow glass microfluidic device schematic shown in (A) and a flow-focusing device shown in (B). (C) is a double emulsion glass microfluidic device combining both co-flow and flow focusing to create double emulsions.[20]

Though glass microfluidic devices can be made with cross-sections of much larger sizes than with PDMS, one drawback lies in the fabrication method of the tapered circular capillary, as it is almost impossible to reproduce a glass-capillary microfluidic device accurately.

During this work, both PDMS and glass microfluidic devices were used. PDMS devices were used due to the large number of easily crafted microfluidic setups and the possibility of easily creating more complex microfluidic setups. Glass microfluidics was used in those instances where larger cross-sections and larger flow rates were targeted.

1.1.3.5 Basic build of a microfluidic experiment

In its most basic build, a microfluidic experiment throughout this work will be divided into three segments as depicted in **figure 1.8**. These three segments are the transport segment, the mixing segment and the collection segment.

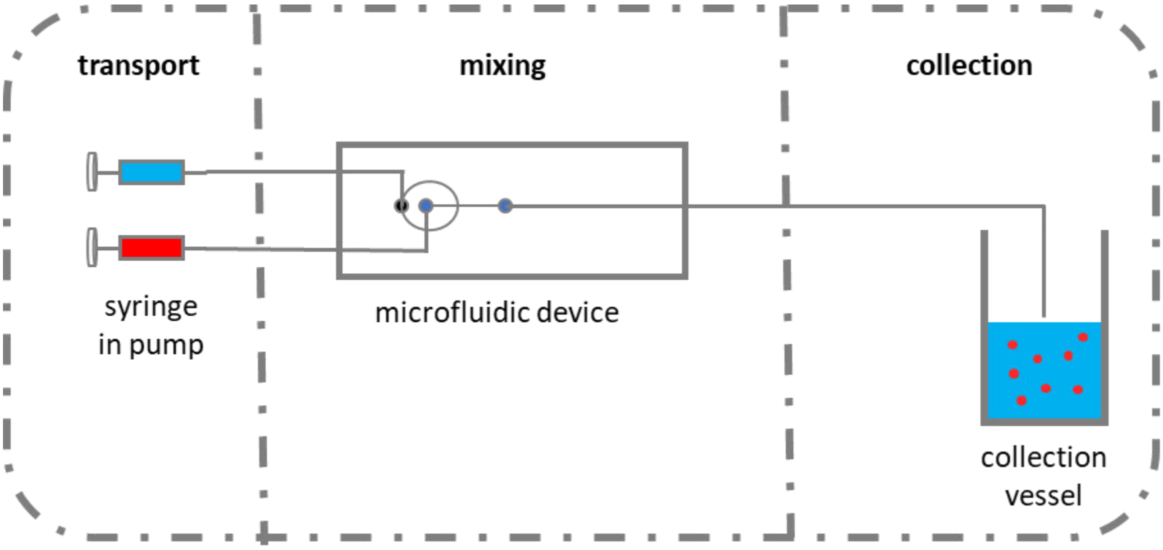

Figure 1.8: Basic build of a microfluidic experiment. In the transport segment the reservoirs for both the dispersed (red) and the continuous (blue) phases are situated. From the transport segment the two immiscible liquids flow to the mixing segment, where the microfluidic device is located. Here depending on the device, the corresponding designer emulsion is created and in the following collection segment collected.

The first segment mainly controls the fluid flow of the dispersed and continuous phase in the microfluidic experiment, and thus, in this work, it will be referred to as the transport segment. The transport of both phases through the experiment can be achieved in multiple ways, for example, via entropy or other gradients such as temperature. In this section, the focus is on pressure-driven flow, as this will be the main method used throughout this work.[20,36] Pressure-driven fluid flow, for example, can be accomplished through the usage of syringe pumps. Such setups are both simple as well as easy to use but come with some drawbacks, for example, the slow response time when changing the flowrate of one of the microfluidic phases. In most syringe pumps the built-in motor can be a further drawback, as at low flowrates, flow oscillations may occur due to the motor itself, thereby limiting the range of flowrates that the syringe pump can continuously uphold. Furthermore, the experimental time is limited by the maximum volume of the syringes, which fit into the syringe pumps. Hermetically sealed liquid tanks connected to a gas input to generate pressure, and a flow controller can be used instead to overcome the limitations of syringe pumps. In this case, the volume of the two phases can be significantly increased, however the setup also becomes more complex.[20]

The second segment in a basic microfluidic experiment is the mixing segment, in which the microfluidic device is situated. In this segment the designer emulsion is created and thus, it is of crucial importance to be able to observe the droplet formation closely. Thus, this part of the experimental setup is often placed under microscopes to observe the forming of the micro-droplets better. Depending on the style of microscope used in the experiment, the microfluidic-device may be placed on a spacer to allow the microscope's objective to directly observe droplet-formation through the glass slide of the microfluidic device. Due to the extremely fast rate at which droplets are created in microfluidic experiments it is furthermore common to equip the microscope with fast shutter cameras of $50 - 100$ fps.[20]

The third segment of a basic microfluidic experiment is the collection segment, in which the emulsion is collected. This is often done in a simple glass vial or beaker.

All three segments are connected together using flexible tubing, of the appropriate size to avoid leakage.

If microparticles are to be obtained from a microfluidic experiment instead of an emulsion, a fourth segment, the reaction segment, is needed, in which the droplets react to form the microparticles. The reaction segment can be situated right after the droplet creation, reaching all the way to the collection segment, with the gelation continuing in the collected emulsion, as depicted schematically in **figure 1.9**. [37,38]

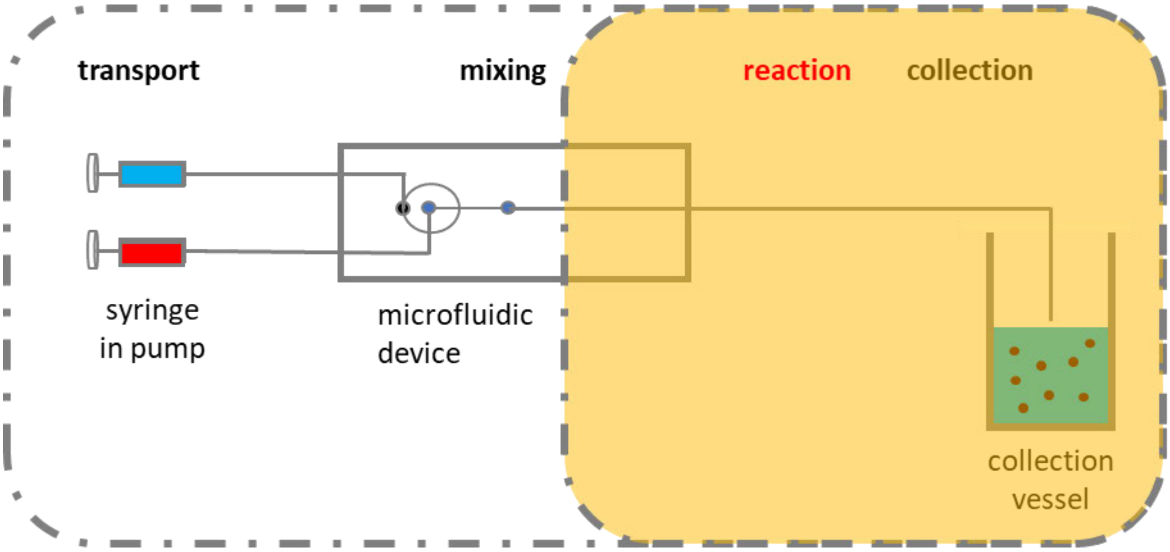

Figure 1.9: Reaction section in a basic microfluidic setup creating microgels instead of an emulsion. The reaction section can be situated anywhere from just after the droplets are created even still within the device all the way to the collection vessel itself.

1.1.3.6 Droplet to microgel transition via free radical polymerization

With microfluidics narrowly distributed polymer microgel particles can be synthesized by free radical polymerization, whereby the precursor micro-droplets act as the confined space in which polymerization proceeds. In this case, the dispersed phase must consist of at least one type of monomer, an initiator for the polymerization, and a crosslinker.[37,39,40] A monomer is defined as "a molecule which can undergo polymerization, thereby contributing constitutional units to the essential structure of a macromolecule"[10], and a crosslinker is necessary for the emergence of the polymeric 3D-network.[10]

The free radical polymerization is one of the simplest polymerization methods. It is dependent on an initiation reaction in which an initiating radical creates a propagating polymer-chain radical. If the propagating radical incorporates a monomer with multiple polymerizable moieties, also known as a chemical crosslinker, a polymer network can be formed. Due to the absence of any outside control during free radical polymerization, termination reactions can take place at any time during the polymerization process. There are two termination reactions possible: the recombination reaction of two radicals and the radical disproportionation reaction, forming an alkane and alkene from two radicals. The resulting polymer networks from free radical polymerizations are prone to have defects due to these terminations in the form of dangling chains as well as polymer loops. A visualization of the different reactions during free radical polymerization is depicted in **figure 1.10**.[41,42]

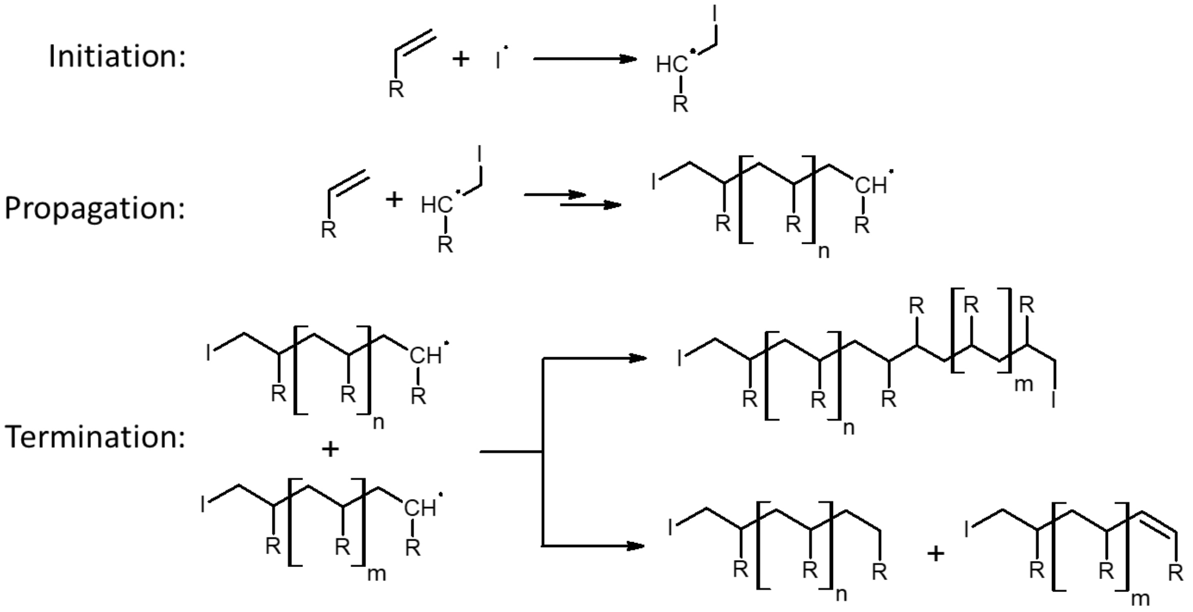

Figure 1.10: Polymerization mechanism during a free radical polymerization.

To create the initiating radical for the free radical polymerization there are two common approaches. In case of a thermal initiation an initiator is used, which will decompose into an initiating radical at a certain temperature. This initiation temperature can be further influenced by additives. An example is the initiator ammonium persulfate (APS) which on itself initiates a polymerization at temperatures exceeding 60 °C, but in combination with *N,N,N',N'*-tetramethylethylenediamine (TEMED) the initiation temperature can be reduced to room temperature. The reaction creating the initiating radicals is displayed in the following **figure 1.11**.[39,41,43]

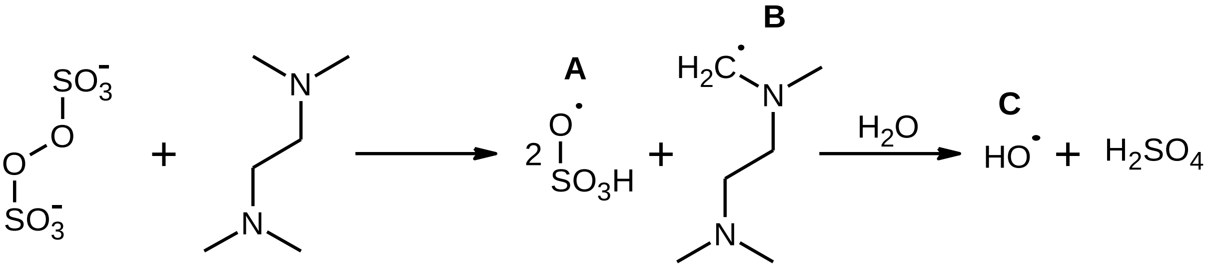

Figure 1.11: Reaction mechanism of APS and TEMED at room temperature, leading to the three initiating radicals, the TEMED radical (B) and the bisulfate radical (A), which further reacts with water to form a hydroxyl radical (C).

Due to the positional limitations of the polymerization in a microfluidic experiment, as described in section 1.1.3.5 and the low initiation temperature of the combination of APS and TEMED, the two components cannot be within the same phase in a microfluidic experiment. Therefore, due to the hydrophilic nature of APS and the hydrophobic nature of TEMED, APS is often part of aqueous dispersed phase and TEMED part of the organic continuous phase. The initiation of the microfluidic droplets, in this case, is dependent on the diffusion rate of the TEMED into the droplets.[39]

A different initiation method of free radical polymerization is the photo-initiation using electromagnetic radiation. In this case the initiator can be directly added to the dispersed phase. Photoactivated initiators have the further advantage, that the moment and place of initiation can be determined by the experimental setup. Furthermore, since the temperature is not critical for the polymerization's initiation the reaction temperature of the polymerization can be varied. An example of a photoactivated initiator is 2,2'-azobis(2-methylpropionamidine) dihydrochloride also known as V-50. Once irradiated with UV-radiation with a wavelength of 365 nm, the initiator decomposes into two initiating radicals, as depicted in **figure 1.12**.[41,44]

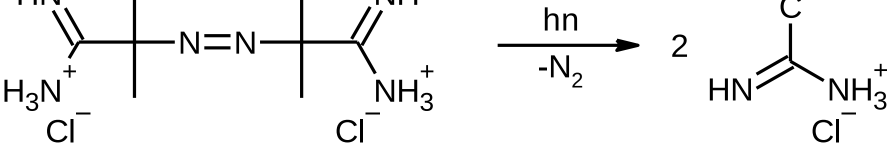

Figure 1.12: Decomposition of V-50 after irradiation with UV-light. During the decomposition Nitrogen gas is released and the two initiating radicals are formed.

1.2 Classifications of hydrogels

As mentioned in 1.1 the definition of the term “hydrogel” is extremely broad. And so, as research into the field intensified the classification of hydrogels became more based on the different properties of the hydrogels themselves. In the following, a few of these classifications are described in more detail as they are relevant for the present work. It is further important to mention that a hydrogel not necessarily will fall into a single classification but may be part of multiple.[45]

1.2.1 The Source of the monomer as classification

The classification of hydrogels via the source of the monomer includes two possible subclasses: natural hydrogels and synthetic hydrogels.[3,45]

Natural hydrogels are hydrogels made from monomers or even polymers found in nature. Among these are collagen, fibrin, hyaluronic acid as well as alginate. Though their natural abundance can be seen as a major advantage, natural hydrogels often suffer two main drawbacks. First, the mechanical properties and their dependence on both the polymerization and gelation conditions, are not always fully understood. Secondly, as they are of natural origin compositions may vary from batch to batch, making the properties and reproducibility of natural hydrogels in some cases difficult to control.[3]

Synthetic hydrogels are, for example, polyethylene glycol, polyacrylates and polyacrylamides. Though the physical and chemical properties of synthetic hydrogels also are highly dependent on the synthesis methods, in general they are more easily tunable than in the case of natural hydrogels.[3]

During the course of this work mainly synthetic hydrogels are synthesized. However, in one smaller project, a mix of both natural and synthetic polymers will be used to form a hydrogel.

1.2.2 Crosslinking of the hydrogel as classification

Classifying a hydrogel by its crosslinks separates hydrogels into physically crosslinked and chemically crosslinked hydrogels.[45]

Physically crosslinked hydrogels, in general, use physical processes, such as complexations, to crosslink the polymer into a three-dimensional network. An example of this would be the crosslinking of alginate via calcium ions.[46]

Chemically crosslinked hydrogels in contrast, use covalent bonds to create the three-dimensional polymer network. Therefore, it is important to either use a monomer with multiple possible reaction sites or a chemical crosslinker such as *N,N'*-methylenebisacrylamide.[37,47]

In this work, all the synthesized hydrogel microgels are chemically crosslinked.

1.2.3 Hydrogel classification by response to stimuli

Hydrogel classification using the responsiveness to certain stimuli is among the most common classifications today. The stimuli hereby are both chemically, for example, pH responsiveness or biochemical in the sense of antigens or enzymes responsiveness or physically, for example, temperature or light responsiveness.[45,48–52]

In this work the synthesized hydrogels consist of acrylic acid or *N*-isopropylacrylamide as monomers. Poly acrylic acid hydrogels can be classified as pH responsive via the neutralization degree of the individual acid groups allowing such polymers to be used as sensors for example.[53,54] Besides being used as possible sensors poly acrylic acid is also commonly used in superabsorbent polymers (SAPs).[37,55,56] The swelling of the SAPs is hereby dependent on several different influences. One of the chapters of this work will discuss the influence of the crosslinker's hydrophobicity.[37] Other influences have already been researched previously, for example, the size and shape [57,58], pH, and other comonomers to name a few.[59,60]

Poly(*N*-isopropylacrylamide) (poly-NIPAM) on the other hand is well known for its thermo-responsiveness and is often used in research for biomedical applications.[61–63] The thermo-response is the result of the lower critical solution temperature (LCST) of poly(*N*-isopropylacrylamide). Poly-NIPAM's LCST lies at 32 °C at which point the polymer transforms from a coil formation to a globule formation. The basis of the LCST behavior lies in the hydrophobic effect of the binary system composed of the solvent, in this case, water, and the polymer. And can be understood via the Gibbs free energy equation ΔG.[63]

$$\Delta G = \Delta H - T\Delta S \tag{1.5}$$

As long as the temperature T is below the LCST the enthalpy of mixing ΔH is negative. This is because of hydrogen bonds between the solvent molecules and the amide groups. The enthalpy, in this case, outweighs the negative effect of the entropy ΔS due to the higher ordered state. However, as the temperature reaches the LCST, the hydrogen bonds are disrupted and break leading to the dominance of the entropy term $T\Delta S$. This, in turn, leads to the phase separation and therefore, the formation of globules.[63] In the case of poly-NIPAM gels the LCST behavior results in a deswelling of the previously swollen polymer gel at temperatures above the LCST.[38]

1.3 Analytical Methods

In this chapter the analytical methods, used during the different projects, are discussed in more detail. Among these are the optical light microscopy, the nuclear magnetic resonance (NMR) spectroscopy and lastly light scattering on gels. Throughout the majority of the work optical light microscopy is of great importance not only as part of the experimental setup as already discussed in **1.1.3.5** but also in the analysis of the synthesized microgels, for example in determining their sizes. NMR spectroscopy is mainly used as reaction control and in the determination of the composition of synthesized polymers. Lastly in one side project the polymer gel structure is analyzed using light scattering.

1.3.1 Optical Light Microscopy

Optical light microscopy is among the oldest analytical methods known to mankind. With the earliest optical microscopes already present at the end of the 16th century.[64] At the advent of optical light microscopy the main problems faced by scientists were optical aberrations, blurred images and poor lens design.[65] Optical aberrations can be divided into spherical aberrations stemming from the shape of the optical lenses as well as chromatic aberration because of the different wavelengths of light both leading to blurred images. However with the production of apochromatic objectives following the works of Ernst Abbe and Carl Zeiss in 1886 the optical aberration could be reduced.[65] In 1893 Professor August Köhler solved the problems of illumination thereby optimizing photomicrography.[65] As proper illumination of the specimen is extremely crucial most modern microscopes are designed to use the Köhler illumination, with both the lighting path and the image path shown in **figure 1.13**.[65]

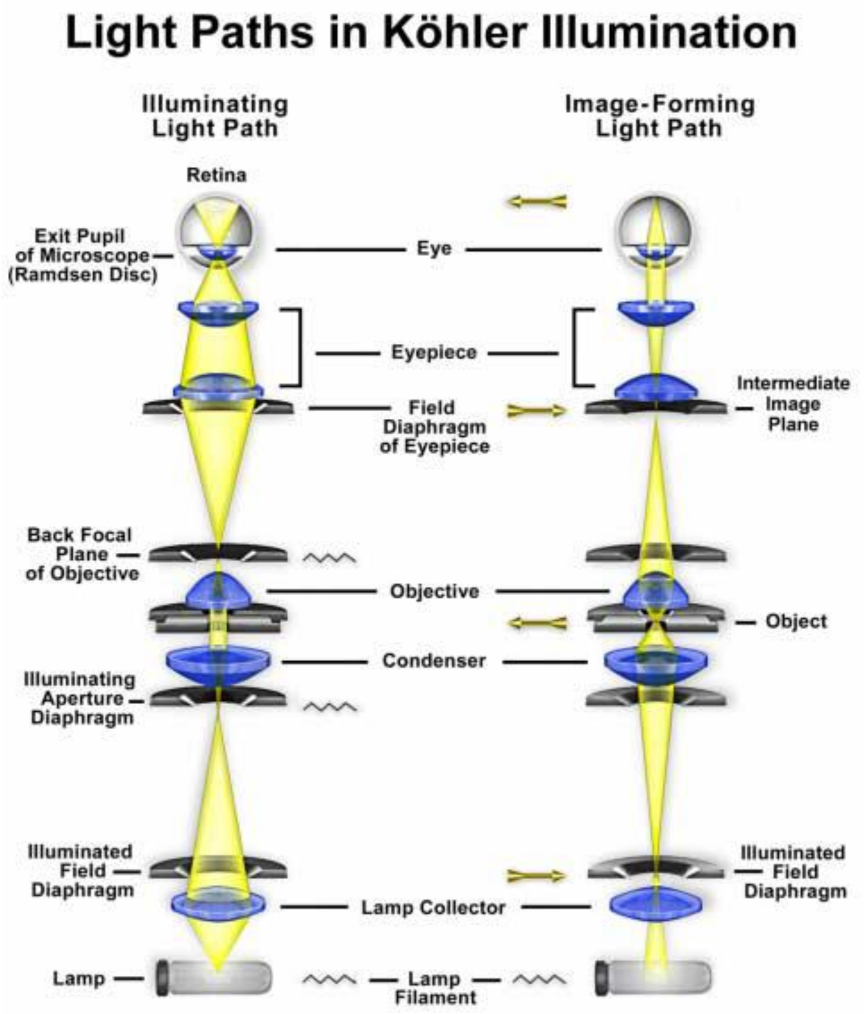

Figure 1.13: Illumination and image forming light paths of the Köhler illumination. On the left the path of the illuminating light and on the right the image forming path.[65]

Over the course of this work mainly the inverted microscope Axio Vert.A1 from Zeiss with objectives N-Achroplan 5x/0,15 Ph1 M27 and N-Achroplan 10x/0,25 M27 was used to investigate both the droplet creation during the microfluidic experiments as well as to determine the sizes of the synthesized microgels.[66,67] Therefore, it is important that the resolution limit of the optical microscopes used is sufficient. In 1873 Professor Abbe from the university of Jena first verbally defined the resolution limit using lattices. Later the Abbe limit was defined mathematically as follows:[65,68]

$$d_{\mathrm{Abbe}} = 0.5 \cdot \frac{\lambda}{n \cdot \sin\alpha} = 0.5 \cdot \frac{\lambda}{NA} \tag{1.6}$$

With λ being the wavelength of the light, n the refractive index of the medium between the objective and the specimen and α the maximum of half the angle between the object and the objective lens. NA stands for the numerical aperture and is often given by the producers of the optical objectives.[65,68]

A few years later in 1896 Rayleigh also defined a resolution limit for optical microscopes. However, in contrast to Abbe he considered light emitting points for his evaluation. His research led to the Rayleigh limit defined as:[65,68]

$$d_{\text{Rayleigh}} = 0.61 \cdot \frac{\lambda}{n \cdot \sin \alpha} = 0.61 \cdot \frac{\lambda}{NA} \tag{1.7}$$

Using the Abbe limit to determine the resolution limit of the objective used for this work, as the hydrogel microparticles do not emit light, a resolution limit using 595 nm as an averaged wavelength of the white light used for illumination would be 1.9 µm for the 5x magnifying objective and 1.2 µm for the 10x magnifying objective. Both these limits are by far smaller than both the intended droplet-sizes as well as the microgels of this work, making the optical light microscopy a useful tool for the analysis of the microgels of this work.

1.3.2 Nuclear Magnetic Resonance (NMR) Spectroscopy

Ever since the discovery of the phenomenon of nuclear magnetic resonance (NMR) by Rabi, Purcell and Bloch the importance of this analytical method quickly became clear. Thus, within a few years both Bloch and Purcell were awarded the noble prize for their research.[69,70] Further research, discovering the chemical shift [71,72], the spin echo [70] and the development of techniques of the Fourier transformation [73] would make NMR spectroscopy a key analytical tool in modern chemical and biological research. In this work ^{1}H-NMR was solely used, therefore only the basics of the NMR spectroscopy will be discussed in more detail in the following.

There are two aspects that are important for the nuclear magnetic resonance. The first aspect is the precession of the magnetic moment within a magnetic field. As an analogy a rotating spinning top with a magnetic top can be used. As it spins the magnetic field causes a torque leading to a precession of the spinning top around its vertical axis. In the case of atomic nuclei this is similar if the nuclear spin I is not zero. In this case a nucleus acts just like a rotating magnet with a magnetic moment μ with a precession around the direction of the magnetic field B_0 (see **figure 1.14**). The frequency of the precession is also known as the Larmor frequency ω_{L}, which is only dependent on the outside magnetic field and the nuclei species in the form of the gyromagnetic ratio γ.[70]

$$\omega_{\text{L}} = \gamma \cdot B_0 \quad \text{or} \qquad \nu_{\text{L}} = \frac{\gamma \cdot B_0}{2\pi} \tag{1.8}$$

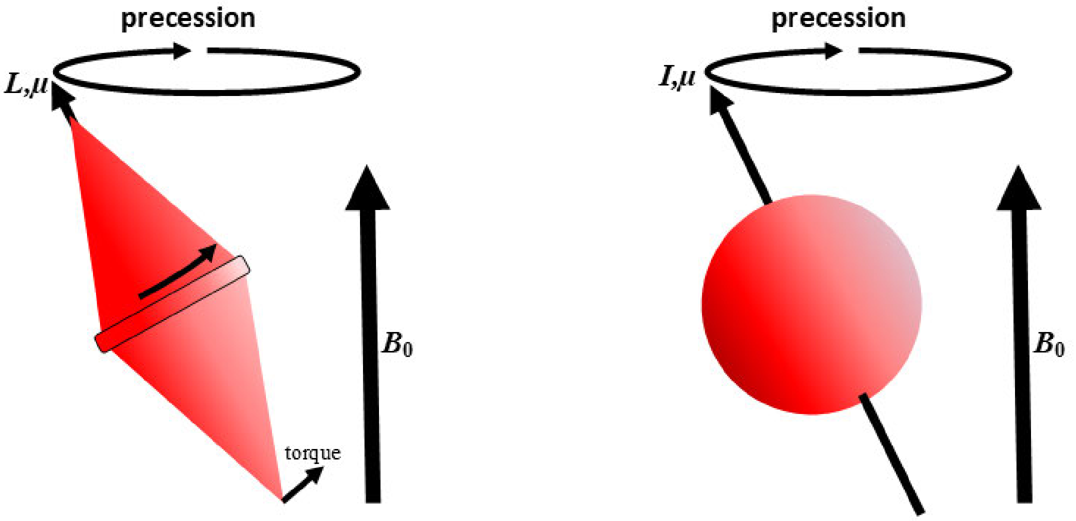

Figure 1.14: On the left spinning magnetic top, with its angular momentum L and magnetic moment μ inside an outside magnetic field B_0 *and on the right an atomic nucleus with its nuclear spin I and the resulting magnetic moment μ within an outside magnetic field* B_0*.*[70]

The second important aspect of NMR spectroscopy is the Zeeman effect. This effect results from the quantum mechanical properties of nuclei. As mentioned for a nucleus to be detectable via NMR spectroscopy the nuclear spin I has to be non-zero. The ^{1}H-nucleus for example has a spin of $I = \frac{1}{2}$. But as long as there is no outside magnetic field present this nuclear spin is not detectable as they would be arbitrarily aligned in space since all directions are energetically degenerated. If, however, there is an outside magnetic field present the interaction of the two leads to the creation of distinct energy levels. The number of distinct energy levels depends on the nuclear spin I which assumes $(2I + 1)$ states. This Zeeman effect for the case of the ^{1}H-nucleus is depicted in **figure 1.15**.[70]

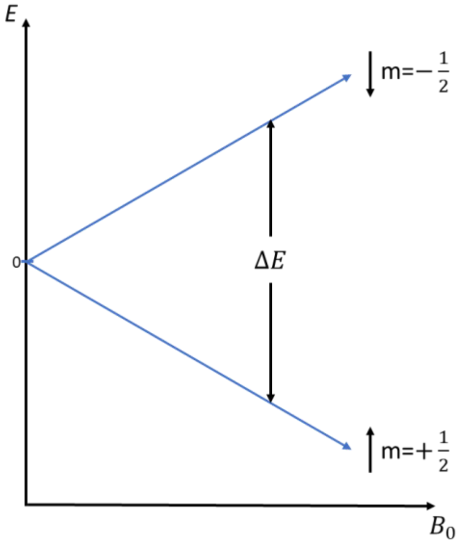

Figure 1.15: Zeeman effect of a nucleus with a nuclear spin of $\frac{1}{2}$ *as for example the* ^{1}*H-nucleus.*[74]

As depicted in figure 1.15 for the case of the ^{1}H-nucleus the Zeeman effect splits the former degenerated energy states into two distinct energy states. In one case the nuclear spin is aligned with the outer magnetic field B_0 and in the other case it is the opposite direction. As the spin orientation aligned with the outer magnetic field B_0 is energetically preferable this state will be slightly more populated in accordance with Boltzmann's law (equation 1.9).[70]

$$\frac{N_{m=-\frac{1}{2}}}{N_{m=+\frac{1}{2}}} = e^{-\frac{\Delta E}{k_\mathrm{b}T}} \tag{1.9}$$

This slight overpopulation of the spin aligned energy state results in a total magnetization M_0 parallel to B_0. During an NMR spectroscopy measurement, a magnetic pulse B_1 orientated 90° to B_0 flips the total magnetization M_0 by 90°. After the pulse the M_0 recovery is measured as a *Free Induction Decay* (FID) signal which is translated into a frequency via a Fourier transformation (FT) as depicted in **figure 1.16**.[70]

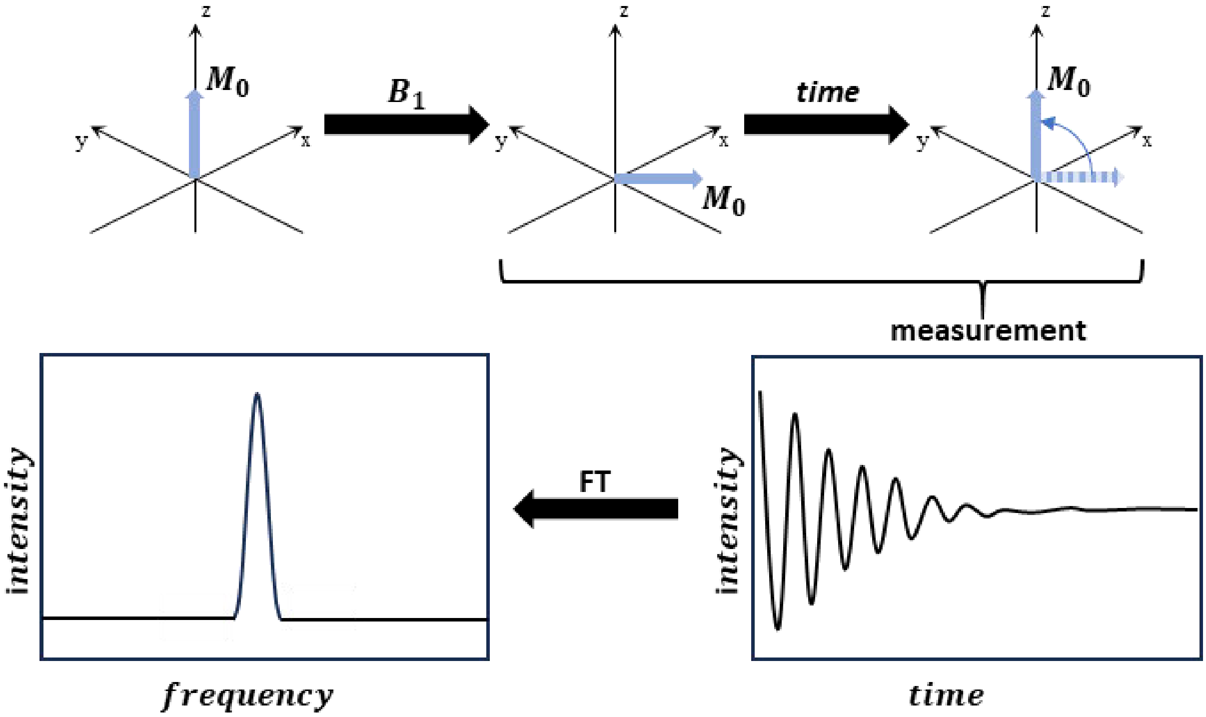

Figure 1.16: On the top the total magnetic moment M_0 in the direction of B_0 (z-direction) is flipped into the XY-plane by the magnetic pulse B_1. Afterwards the magnetic moment recovers which is measured and using a Fourier transformation (FT) transferred into a frequency signal.[70]

Using the chemical standard tetramethyl silane (TMS) the frequency can be translated into a chemical shift δ according to the equation 1.10.

$$\delta = \frac{\nu_r - \nu_0}{\nu_0} \cdot 10^6 \tag{1.10}$$

With ν_r being the Larmor frequency of the sample and ν_0 the Larmor frequency of the standard TMS. The chemical shift δ is further dependent on the environment of the nucleus allowing for example to analyze products of chemical reactions.[70]

1.3.3 Light scattering on gels

Ever since the 1870s first light scattering experiments were used to determine particle sizes by Tyndall and Rayleigh. In 1944 Debye would for the first time also use light scattering to determine the molecular weights of macromolecules via a technique now called static light scattering or SLS. From 1964 dynamic light scattering (DLS) would also start to gain popularity to determine hydrodynamic radii as well as diffusion coefficients. The main reason for the time delay between the emergence of SLS and DLS being technological, as DLS needs very monochromatic, intense and coherent light sources such as lasers, which would only be invented in 1960.[75]

Though in both SLS and DLS the intensity of the scattered light is measured, in the case of SLS the intensity measured is averaged over the time of the measurement, whilst in the case of DLS the focus is on the fluctuation of the measured intensity.[76]

A sketch of a basic setup of a light scattering experiment is depicted in **figure 1.17**. It includes a laser as light source, a toluene bath for the temperature control of the sample, the sample itself and the moveable detector, measuring the intensity of the scattered light at known angles Θ. The detector is further connected to correlators and a computer. [75]

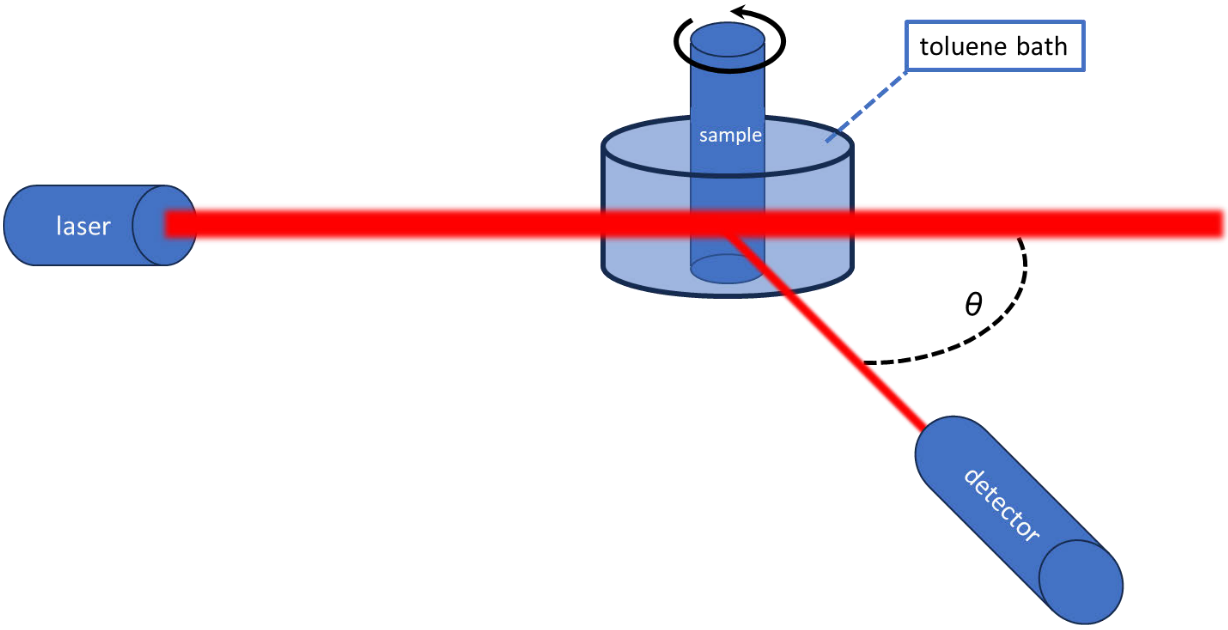

Figure 1.17: Sketch of a light scattering experimental setup including a temperature control of the sample, a light source and a moveable detector. The detector measures the intensity of the scattered light and forwards the information to correlators and a computer for future analysis.

The foundation of light scattering experiments independent if SLS or DLS is the interaction of the sample molecule with the oscillating electric field E_i of the incident light wave. This interaction leads to a dipole moment μ_ind, the strength of which is also dependent on the polarizability α of the sample itself. This dipole moment oscillates perpendicular to the incident beam and is called a Hertzian dipole which radiates light at the same frequency as the initiating radiation.[77]

$$E_\mathrm{i} = E_0 \cdot \sin(\omega t - kx) \tag{1.11}$$

$$\mu_\mathrm{ind} = \alpha \cdot E_\mathrm{i} \tag{1.12}$$

With E_0 the amplitude, ω the frequency and k the absolute value of the wave vector of the incident beam $\left(k = \frac{2\pi}{\lambda}\right)$. λ is the wavelength of the incident beam.

During light scattering experiments though only intensities I and not the electrical field strengths are measured. The two are however proportional to one another according to the following equation:[77]

$$I \sim |E|^2 \tag{1.13}$$

As however the measured scattering intensity I_S not only depends on the sample properties but also on the experimental setup, the absolute scattering intensity or also known as the Rayleigh ratio R is determined from the measured scattering intensities.[77]

$$R = \frac{4\pi^2}{\lambda_0^4} \cdot n_{\mathrm{D},0}^2 \cdot \left(\frac{\partial n_\mathrm{D}}{\partial c}\right)^2 \cdot \frac{cM}{N_\mathrm{L}} = (I_\mathrm{solution} - I_\mathrm{solvent}) \cdot \frac{r_\mathrm{D}^2}{V} \tag{1.14}$$

With λ_0 the wavelength of the incident beam, $n_{\mathrm{D},0}$ the refractive index of the solvent, $\left(\frac{\partial n_\mathrm{D}}{\partial c}\right)$ the refractive index increment, c the concentration of the sample, M the molar mass of the sample and N_L the Avogadro constant. r_D is the distance between the sample and the detector and V is the scattering volume.

Experimentally the Rayleigh ratio R is determined using a scattering standard I_std, which in most cases is toluene.[77]

$$R = (I_\mathrm{solution} - I_\mathrm{solvent}) \cdot \frac{I_\mathrm{std,abs}}{I_\mathrm{std}} \tag{1.15}$$

$I_\mathrm{std,abs}$ is the absolute scattering intensity of the standard, which can be found in reference tables.

If the sample particle size becomes larger than $\frac{\lambda}{20}$, then the intensity of the scattered light is further dependent on the angle Θ at which the scattered light is measured. In these cases, the scattering vector $\vec{q}$ is important. It is the difference between the vectors of the incident and scattered light. Its length is dependent on several factors, the scattering angle Θ, the wavelength of the incident beam λ and the refractive index of the solvent n_D.[77]

$$|\vec{q}| = q = \frac{4\pi \cdot n_\mathrm{D} \cdot \sin\left(\frac{\Theta}{2}\right)}{\lambda} \tag{1.16}$$

Over the course of this work all samples measured are polymer gels however. These have in contrast to equal monomer solutions, increased light scattering intensities. The reason for this is that the concentration fluctuations in polymer gels are the sum of the frozen concentration fluctuations $\delta c_C(\vec{r})$ from spatial inhomogeneous distributions of the crosslinking points of the gel itself and the dynamic thermal concentration fluctuations $\delta c_F(\vec{r})$ resulting from the polymer chains Brownian motion.[76,78]

The Rayleigh ratio of polymer gels R_{Gel} therefore is a superposition of the scattering intensity of the fluid contribution of the gel R_F and the excess scattering from the frozen gel concentrations R_{Ex}, as depicted in **figure 1.18**.[78]

$$R_{\mathrm{Gel}} = R_{\mathrm{F}} + R_{\mathrm{Ex}} \tag{1.17}$$

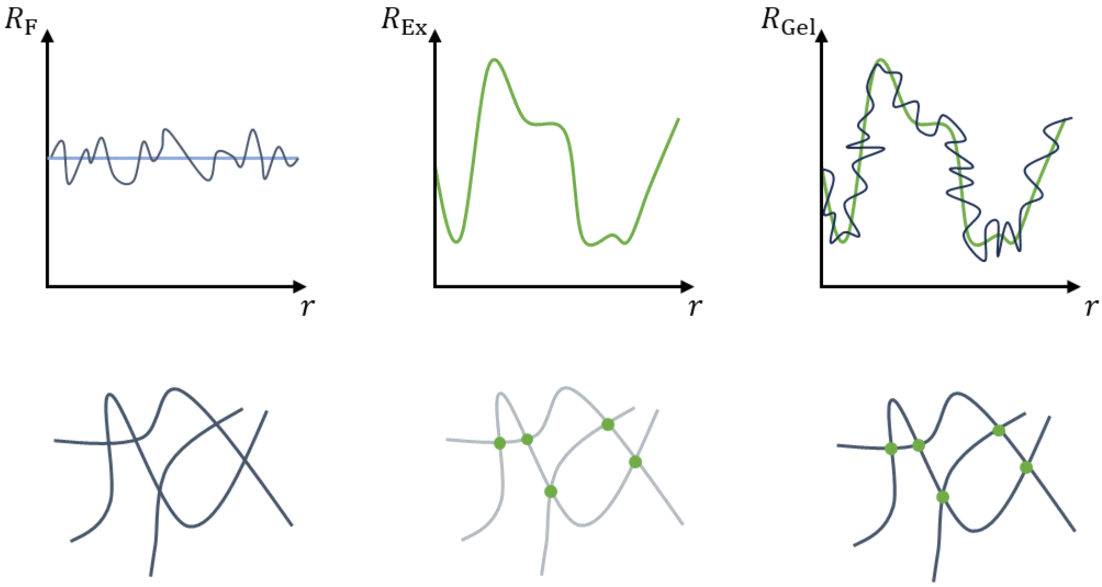

Figure 1.18: location dependent scattering intensity of the fluid contribution of the gel R_F *and excess scattering from the frozen gel concentrations* R_{Ex} *as well as their superposition as* R_{Gel}.[76]

Since the frozen concentration fluctuations are not spatially homogeneous, polymer gels are non-ergodic. This means that the average of the scattering intensity in one specific spot does not represent the average of the entire polymer gel. Therefore, it is necessary when measuring polymer gels to measure multiple points within the gel to gain adequate statistical values for the entire polymer gel. This is done by rotating the polymer gel between measurements using a rotary device. This creates a speckle pattern as shown in **figure 1.19**. Since each one of these so-called speckles is measured over a certain amount of time, both SLS and DLS are measured at the same time when investigating polymer gels.[78]

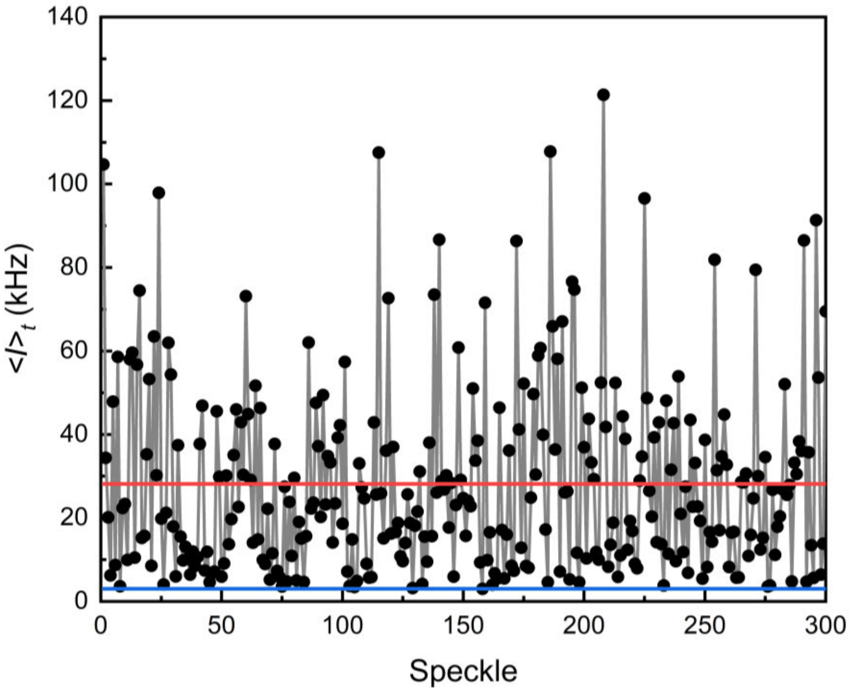

Figure 1.19: Light scattering measurement of a polymer gel. Each speckle (black dot) represents one position in the gel, measured at the same angle. With the red line resembling the ensemble value of the scattering intensity $\langle I \rangle_E$ and the blue line representing the fluid scattering intensity $\langle I_F \rangle_E$ as minimum.

Using the speckle ensemble, it is possible to determine the static correlation lengths Ξ of the polymer gel using three different methods. These methods are the Debye-Bueche method, the Guinier method and the Ornstein-Zernike method.[76] For all methods a variation of $\langle I \rangle_\mathrm{E}$ is plotted against q^2 and a linear fit made. The static correlation lengths Ξ is calculated from the incline m and y-intercept b of the linear fit as summarized in **table 1.1**.[76]

Table 1.1: Summary of the three methods to calculate the static correlation lengths Ξ after making a linear fit of the corresponding plots vs q^2.[76]

Method	**Debye-Bueche**	**Guinier**	**Ornstein-Zernike**
Plot vs q^2	$\langle I \rangle_\mathrm{E}^{-\frac{1}{2}}$	$\ln(\langle I \rangle_\mathrm{E})$	$\langle I \rangle_\mathrm{E}^{-1}$
$\Xi =$	$\left(\frac{m}{b}\right)^{\frac{1}{2}}$	$\lvert m \rvert^{\frac{1}{2}}$	$\left(\frac{m}{b}\right)^{\frac{1}{2}}$

The static correlation lengths Ξ is often used as a reference for the spatial inhomogeneity of the polymer network and is usually in the range of 10 to 100 nm in the case of a polymer network made via free radical polymerization.[76,79]

As each speckle shown in figure 1.19 includes an DLS measurement it is possible to also determine the dynamic correlation length ξ_dyn. In this work the partial heterodyne method according to Joosten et al. will be used. The partial heterodyne method suggests that the frozen fraction of the scattering medium superimposes its scattering onto the dynamic fraction, which is the dynamically interesting one.[76]

In the Joosten approach the fluctuating intensity of the scattered light is correlated using the following equation:[78]

$$g_{\mathrm{T,p}}^{(2)}(q,\tau) = \frac{\langle I(t)I(t+\tau)\rangle_{\mathrm{T,p}}}{\langle I(t)\rangle_{\mathrm{T,p}}^{2}} = X_{\mathrm{p}}^{2} \cdot g_{\mathrm{F}}^{(1)}(q,\tau)^{2} + 2X_{\mathrm{p}} \cdot \left(1 - X_{\mathrm{p}}\right) \cdot g_{\mathrm{F}}^{(1)}(q,\tau) + 1 \qquad (1.18)$$

$$X_{p} = \frac{\langle I_{\mathrm{F}}\rangle_{\mathrm{T}}}{\langle I\rangle_{\mathrm{T,p}}} \qquad (1.19)$$

With $g_{\mathrm{T,p}}^{(2)}(q,\tau)$ the second-order correlation function, $g_{\mathrm{F}}^{(1)}(q,\tau)$ the field correlation function and X_{p} the ratio of the intensity for the thermal fluctuations and the total intensity.[78]

Using monoexponential fitting of the correlation data using equation 1.20 and plotting the inverse of the averaged characteristic relaxation time τ against q^2 allows the determination of dynamic correlation length ξ_{dyn} according to equation 1.21.[78]

$$g_{\mathrm{F}}^{(1)}(q,\tau) = \exp(-D_{\mathrm{HT}} \cdot q^{2} \cdot \tau) \qquad (1.20)$$

$$\xi_{\mathrm{dyn}} = \frac{k_{\mathrm{b}}T}{6\pi \cdot \eta \cdot m} \qquad (1.21)$$

With η the viscosity, k_{b} the Boltzmann constant, T the temperature and m the slope of the linear fit of τ^{-1} vs q^2.

1.4 References

[1] S. Thomas, B. Sharma, P. Jain, S. Shekhar (Eds.), *Sustainable hydrogels: Synthesis, properties, and applications*, Elsevier, Amsterdam, Netherlands, Oxford, England, Cambridge, Massachusetts **2023**.

[2] T. Kubo, Z.-Z. Zhao, *Chinese Medicine and Culture* **2022**, *5*, 39.

[3] L. Yahia, N. Chirani, L. Gritsch, F. Leonardo M., S. Chirani, S. Faré, *J Biomed Sci* **2015**, *04*.

[4] B. D. Ratner, G. Zhang, in *Biomaterials science: An introduction to materials in medicine* (Eds.: W. Wagner, S. Sakiyama-Elbert, G. Zhang, M. J. Yaszemski), Academic Press, an imprint of Elsevier. London **2020**, p. 21.

[5] O. WICHTERLE, D. LÍM, *Nature* **1960**, *185*, 117.

[6] S. Cascone, G. Lamberti, *International journal of pharmaceutics* **2020**, *573*, 118803.

[7] S. D. Palanivelu, N. A. Z. Armir, A. Zulkifli, A. H. A. Hair, K. M. Salleh, K. Lindsey, M. H. Che-Othman, S. Zakaria, *Polymers* **2022**, *14*.

[8] *What's In A Pampers Diaper?* **2024**, https://www.pampers.com/en-us/about-us/quality-and-safety/article/whats-in-a-pampers-diaper.

[9] M. Hu, J. Guo, J. Du, Z. Liu, P. Li, X. Ren, Y. Feng, *Journal of colloid and interface science* **2019**, *538*, 397.

[10] V. Gold, *The IUPAC Compendium of Chemical Terminology*, International Union of Pure and Applied Chemistry (IUPAC), Research Triangle Park, NC **2019**.

[11] William J. Elford, *Proc. R. Soc. Lond. B.* **1930**, *106*, 216.

[12] G. I. Peterson, W. Ko, Y.-J. Hwang, T.-L. Choi, *Macromolecules* **2020**, *53*, 7795.

[13] A. P. Smith, J. S. Shay, R. J. Spontak, C. M. Balik, H. Ade, S. D. Smith, C. C. Koch, *Polymer* **2000**, *41*, 6271.

[14] J. Huling, S. Illner, N. Grabow, M. Teske, *Current Directions in Biomedical Engineering* **2021**, *7*, 531.

[15] Z. Mahdieh, A. Holian, *J of Applied Polymer Sci* **2020**, *137*.

[16] H. Alzanbaki, M. Moretti, C. A. E. Hauser, *Micromachines* **2021**, *12*.

[17] C. S. Chern, *Progress in Polymer Science* **2006**, *31*, 443.

[18] P. A. Lovell, F. J. Schork, *Biomacromolecules* **2020**, *21*, 4396.

[19] R. K. Shah, H. C. Shum, A. C. Rowat, D. Lee, J. J. Agresti, A. S. Utada, L.-Y. Chu, J.-W. Kim, A. Fernandez-Nieves, C. J. Martinez, D. A. Weitz, *Materials Today* **2008**, *11*, 18.

[20] S. Seiffert, J. Thiele, *Microfluidics: Theory and Practice for Beginners*, De Gruyter, Berlin, Boston **2020**.

[21] S.-Y. Teh, R. Lin, L.-H. Hung, A. P. Lee, *Lab on a chip* **2008**, *8*, 198.

[22] H. Feng, T. Zheng, M. Li, J. Wu, H. Ji, J. Zhang, W. Zhao, J. Guo, *Electrophoresis* **2019**, *40*, 1580.

[23] J. Zhang, S. Yan, D. Yuan, G. Alici, N.-T. Nguyen, M. Ebrahimi Warkiani, W. Li, *Lab on a chip* **2016**, *16*, 10.

[24] A. L. R. Costa, A. Gomes, R. L. Cunha, *Experimental Thermal and Fluid Science* **2017**, *85*, 167.

[25] D. N. Josephides, S. Sajjadi, *Langmuir the ACS journal of surfaces and colloids* **2015**, *31*, 1218.

[26] J.-C. Baret, *Lab on a chip* **2012**, *12*, 422.

[27] M. Xu, L. Xu, Q. Lin, X. Pei, J. Jiang, H. Zhu, Z. Cui, B. P. Binks, *Langmuir the ACS journal of surfaces and colloids* **2019**, *35*, 4058.

[28] Q. Zhu, Y. Pan, X. Jia, J. Li, M. Zhang, L. Yin, *Comprehensive reviews in food science and food safety* **2019**, *18*, 1660.

[29] D. J. Harrison, K. Fluri, K. Seiler, Z. Fan, C. S. Effenhauser, A. Manz, *Science (New York, N.Y.)* **1993**, *261*, 895.

[30] S. C. Jacobson, R. Hergenroeder, L. B. Koutny, J. M. Ramsey, *Anal. Chem.* **1994**, *66*, 2369.

[31] S. C. Jacobson, A. W. Moore, J. M. Ramsey, *Anal. Chem.* **1995**, *67*, 2059.

[32] C. M. Matzke, R. J. Kottenstette, S. A. Casalnuovo, G. C. Frye-Mason, M. L. Hudson, D. Y. Sasaki, R. P. Manginell, C. C. Wong, in *Micromachining and Microfabrication Process Technology IV* (Ed.: J. H. Smith), SPIE **1998**, p. 262.

[33] A. W. Moore, S. C. Jacobson, J. M. Ramsey, *Anal. Chem.* **1995**, *67*, 4184.

[34] S. M. Scott, Z. Ali, *Micromachines* **2021**, *12*.

[35] A. Del Campo, C. Greiner, *J. Micromech. Microeng.* **2007**, *17*, R81-R95.

[36] T. Bayraktar, S. B. Pidugu, *International Journal of Heat and Mass Transfer* **2006**, *49*, 815.

[37] T. G. Linder, A. Heinzelmann, J. Kamphus, S. Seiffert, *Macro Chemistry & Physics* **2024**, *225*.

[38] M. Seuss, W. Schmolke, A. Drechsler, A. Fery, S. Seiffert, *ACS applied materials & interfaces* **2016**, *8*, 16317.

[39] F. Di Lorenzo, S. Seiffert, *Macromol. React. Eng.* **2016**, *10*, 201.

[40] R. Seemann, M. Brinkmann, T. Pfohl, S. Herminghaus, *Reports on progress in physics. Physical Society (Great Britain)* **2012**, *75*, 16601.

[41] S. Koltzenburg, M. Maskos, O. Nuyken, *Polymere: Synthese, Eigenschaften und Anwendungen*, Springer Berlin Heidelberg, Berlin, Heidelberg **2024**.

[42] A. v. Herk, *Chemistry and technology of emulsion polymerisation*, John Wiley & Sons **2013**.

[43] T. Sun, P. Xu, Q. Liu, J. Xue, W. Xie, *European Polymer Journal* **2003**, *39*, 189.

[44] Z. Fang, X.-R. Cao, Y.-L. Yu, M. Li, *Colloids and Surfaces A: Physicochemical and Engineering Aspects* **2019**, *570*, 282.

[45] F. Ullah, M. B. H. Othman, F. Javed, Z. Ahmad, H. Md Akil, *Materials science & engineering. C, Materials for biological applications* **2015**, *57*, 414.

[46] J. Berg, S. Seiffert, *Journal of Polymer Science* **2023**, *61*, 2203.

[47] C. Bunk, N. Fribiczer, L. Lucas, M. Geisler, V. Brigitte, S. Seiffert, K. Saalwächter, M. Lang, F. Böhme, *Polymer* **2024**, *304*, 127149.

[48] F. Jianqi, G. Lixia, *European Polymer Journal* **2002**, *38*, 1653.

[49] P. Gupta, K. Vermani, S. Garg, *Drug discovery today* **2002**, *7*, 569.

[50] T. Miyata, N. Asami, T. Uragami, *Nature* **1999**, *399*, 766.

[51] H. Katono, A. Maruyama, K. Sanui, N. Ogata, T. Okano, Y. Sakurai, *Journal of Controlled Release* **1991**, *16*, 215.

[52] B. Jeong, A. Gutowska, *Trends in biotechnology* **2002**, *20*, 305.

[53] L. da Silva, F. E. da Silva, C. V. Franco, R. B. Nuernberg, T. Gomes, R. Miranda, M. M. da Silva Paula, *Materials Science and Engineering: C* **2009**, *29*, 599.

[54] C. Ruan, K. Zeng, C. A. Grimes, *Analytica Chimica Acta* **2003**, *497*, 123.

[55] Z. S. Liu, G. L. Rempel, *J of Applied Polymer Sci* **1997**, *64*, 1345.

[56] J. Bao, S. Chen, B. Wu, M. Ma, Y. Shi, X. Wang, *J of Applied Polymer Sci* **2015**, *132*.

[57] T. Tanaka, D. J. Fillmore, *The Journal of Chemical Physics* **1979**, *70*, 1214.

[58] Y. Li, T. Tanaka, *The Journal of Chemical Physics* **1990**, *92*, 1365.

[59] J. Jovanovic, B. Adnadjevic, A. Kostic, *J of Applied Polymer Sci* **2010**, *116*, 1036.

[60] K. Sunitha, R. Sadhana, D. Mathew, C. P. Reghunadhan Nair, *Designed Monomers and Polymers* **2015**, *18*, 512.

[61] X. Xu, Y. Liu, W. Fu, M. Yao, Z. Ding, J. Xuan, D. Li, S. Wang, Y. Xia, M. Cao, *Polymers* **2020**, *12*.

[62] A. Alexander, Ajazuddin, J. Khan, S. Saraf, S. Saraf, *European journal of pharmaceutics and biopharmaceutics official journal of Arbeitsgemeinschaft fur Pharmazeutische Verfahrenstechnik e.V* **2014**, *88*, 575.

[63] G. Pasparakis, C. Tsitsilianis, *Polymer* **2020**, *211*, 123146.

[64] T. ARAKI, *Mechanical Engineering Reviews* **2017**, *4*, 16-00242-16-00242.

[65] M. W. Davidson, M. Abramowitz, *Encyclopedia of imaging science and technology*, Wiley, New York, NY **2002-**.

[66] Carl Zeiss Microscopy Deutschland GmbH, *Objektiv N-Achroplan 10x/0,25 M27: Beschreibung Objektiv N-Achroplan 10x/0,25 M27 (a=6,5mm)*, https://www.micro-shop.zeiss.com/de/de/shop/objectives/420940-9901-000/Objektiv-N-Achroplan-10x-0,25-M27.

[67] Carl Zeiss S.p.A. con socio unico, *Objektiv N-Achroplan 5x/0,15 Ph1 M27: Beschreibung Objektiv N-Achroplan 5x/0,15 Ph1 M27 (a=12,0mm)*, https://www.micro-shop.zeiss.com/de/it/shop/objectives/420931-9911-000/Objektiv-N-Achroplan-5x-0,15-Ph1-M27.

[68] C. Cremer, *Physik in unserer Zeit* **2011**, *42*, 21.

[69] M. V. Silva Elipe, *LC-NMR and other hyphenated NMR techniques: Overview and applications*, John Wiley & Sons **2011**.

[70] L. Schröder (Ed.), *In vivo NMR imaging: Methods and protocols*, Humana Press, New York u.a. **2011**.

[71] W. G. Proctor, F. C. Yu, *Phys. Rev.* **1950**, *77*, 717.

[72] W. C. Dickinson, *Phys. Rev.* **1950**, *77*, 736.

[73] R. R. Ernst, W. A. Anderson, *Review of Scientific Instruments* **1966**, *37*, 93.

[74] R. S. Macomber, *A complete introduction to modern NMR spectroscopy*, Wiley, New York, NY u.a. **1998**.

[75] L. H. Øgendal, *Light scattering demystified* **2016**.

[76] S. Seiffert, *Progress in Polymer Science* **2017**, *66*, 1.

[77] W. Schärtl, *Light Scattering from Polymer Solutions and Nanoparticle Dispersions*, Springer Berlin Heidelberg; Imprint: Springer, Berlin, Heidelberg **2007**.

[78] M. Shibayama, *Bulletin of the Chemical Society of Japan* **2006**, *79*, 1799.

[79] A. Habicht, W. Schmolke, G. Goerigk, F. Lange, K. Saalwächter, M. Ballauff, S. Seiffert, *J Polym Sci B Polym Phys* **2015**, *53*, 1112.

2. Motivation and Scientific Goal

As mentioned in the introduction hydrogels have been present in human use for decades. However, with the fields in which hydrogels are employed expanding from older uses in glue or in personal hygiene products to the fields of medicine and agriculture their importance has significantly increased. It therefore is essential for research to focus on how to tune the properties of the hydrogels, which are a result of both their composition and their production method. Droplet-based microfluidics is ideal to analyze the interplay of composition and properties in hydrogels. The good heat exchange between the droplets and the continuous phase allows to examine the effects of even small changes to composition and with the extreme design adaptability of the microfluidic devices even more complicated hydrogels can be synthesized from the designed emulsions. Thus, this method will be used throughout this work to explore both the interplay of design and composition of hydrogels on their properties.

With all of these advantages droplet-based microfluidics still has one mayor drawback, its output of microgels. Therefore, in the first main project of this work the aim is to modify an already existing microfluidic experimental setup to increase its yield. With photo-initiation of the polymerization used the focus lies in the redesign of the reaction segment of the setup, to allow increased flowrates and with this also increase the microgel production.

The second main project is part of the research training group (RTG) 2516.The aim of this project in project area D – Microgels, is to synthesize core-shell microgels with a thermo-sensitive core and a non-temperature sensitive shell. To do so microfluidics is the method of choice, as with this method both the cores and core-shell particles can be created using the corresponding designed emulsions. Besides the successful synthesis of the core-shell particles the aim is to further control the interconnectivity of the shell and core. Through variation of the interconnectivity the change in the elastic modulus of the core-shell particles can be influenced. This switch-ability of the elasticity is beneficial for directing stem-cell differentiation, as it is influenced by the matrix elasticity on which the stem-cells are located. Furthermore, in a tandem project with the simulation-partner [redacted] diffusion simulations of linear polymers into simulated gel slabs are conducted and analyzed to enhance the knowledge of the theoretical side and on how to better control the core-shell interpenetration profile.

The third main project aims to investigate the influence of the crosslinker hydrophobicity on the swelling of microgels. In many commercial products the physical properties of the hydrogels are predetermined, however the crosslinker hydrophobicity is one possibility to influence the swelling of the microgels without influencing the physical properties to a large degree. As synthesis method microfluidics is to be used, as it limits the structural effects on the polymer network stemming from the polymerization method. Therefore, allowing the investigation of the influence of the crosslinker hydrophobicity on the swelling of the hydrogels. For this the composition of the microgels is to be kept constant while the crosslinker and its hydrophobicity is changing.

In addition to the third main project the effect of the crosslinker hydrophobicity on the gel structure is the aim of a first side project. For this macro gels identical in composition to the microgels of the third main project are analyzed using light scattering on polymer gels. The static and dynamic correlation lengths are to be determined and compared with the aim to further the understanding of the correlation of the gel structure and its composition.

In the second side project the goal is to create a microfluidic experimental setup accommodating the complex requirements to create carbomer974p-agarose hydrogels crosslinked with hyaluronic acid. Since the polymerization is initiated prior to the start of the microfluidic experiment large parts of the experimental setup need to be kept at high temperatures to keep the forming polymer network in its sol state. The corresponding microgels are especially interesting as possible future drug carriers in the field of medicine.

3. Project I: Improving the droplet-based microfluidic setup

3.1 Introduction and aim of the project

As described in the theoretical background, microfluidics is a common method to create microgels. The main aim of this project was to improve the already existing experimental microfluidic setup schematically depicted in **figure 3.1**.

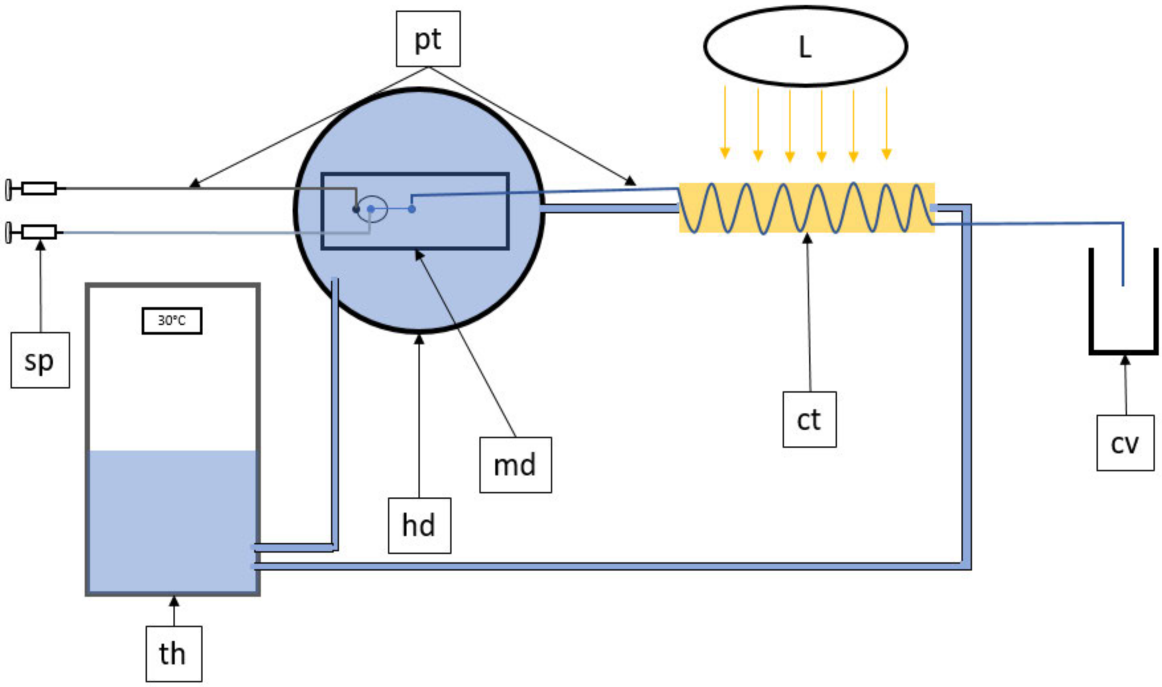

Figure 3.1: Sketch of the microfluidic setup to be improved. With (sp) being the syringes filled with the continuous phase and the dispersed phase. (Pt) is the polyethylene tubing connecting the syringes with the microfluidic chip (md) and the chip with the collection vessel (cv). The polymerization is initiated in the irradiated area by the Black-Ray B-100 AP High Intensity UV lamp (L). For temperature control a thermostat (th) is connected to the heating device for the microfluidic chip (hd) and the copper tubing (ct).

The experimental setup had been developed for previous research on microgels and the influence of the crosslinker hydrophobicity on the swelling capacity. It is fully temperature controlled during the droplet creation, via a microfluidic chip temperature control device and the droplet polymerization, by wrapping the polyethylene exit tube around a copper wire. For polymerization of the droplets and creating microgels the photo-initiator V-50 is used, which is initiated using a *Black-Ray B-100 AP High Intensity UV lamp* from *UVP*. The setup was used in previous own research creating microgels with flowrates of the dispersed phase of 100 $\frac{\mu\text{L}}{\text{h}}$ and 125 $\frac{\mu\text{L}}{\text{h}}$ for the continuous phase.

The limiting factor for the yield of the microfluidic experiment was the gelation of the microfluidic droplets, as they needed to be sufficiently irradiated for the gelation to occur. Increasing the flowrates of both the dispersed and the continuous phase using the above depicted microfluidic experimental setup was therefore hindered, as the gelation of the droplets would no longer occur. The device was self-made of PDMS with a channel size of 100 µm, as described in the theoretical background under **1.1.3.4.** As in essence the yield of a microfluidic experiment is closely tied to the flowrates of the experiment the main focus of this project was to modify the reaction segment of the setup to allow for increased flowrates, whilst still achieving gelation of the microfluidic droplets within the setup itself.

3.2 Areas of Improvement

As in previous own research it was proven, that the concentration of the initiator V-50 could not be increased, due to solubility issues thereof, the focus was on improving the main components of the reaction segment. This includes as depicted in figure 3.1 the radiation source and the polyethylene tubing wrapped around the copper tube.

3.2.1 Improving the radiation source

As radiation source in the original setup a *Black-Ray B-100 AP High Intensity UV lamp* from *UVP* was used. This lamp is capable to produce 100 Watt. To improve this aspect the lamp was switched to the *OmniCure series 1500* from *Excelitas technologies*. The two lamps are both depicted in **figure 3.2**.

Figure 3.2: On the left side the Black-Ray B-100 AP High Intensity UV lamp from UVP used in the original microfluidic setup. On the right the OmniCure series 1500 from Excelitas which replaced the left lamp in the improved microfluidic setup.

The *OmniCure series 1500* is a more powerful radiation source due to the *200-Watt-Intelli-Lamp*®.[1] Furthermore, in contrast to the *Black-Ray B-100 AP High Intensity UV lamp* the radiated area ($\emptyset \leq 12.5$ cm) could be much more focused due to glass-fiber cable ($\emptyset = 0.5$ cm) directing the radiation of the *OmniCure series 1500.* The lamp would be placed 4 – 6 cm above the droplets with the intensity level controllable via the control panel seen in figure 3.2. To protect the experimentalist from the high levels of UV-radiation a metal box and aluminum foil was used as depicted in **figure 3.3**.

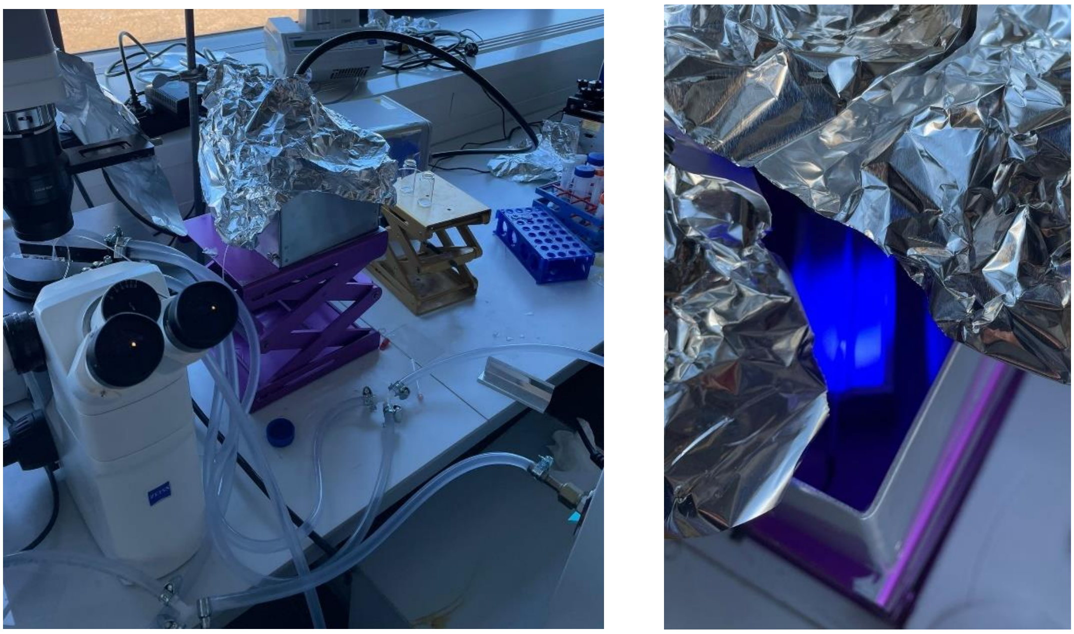

Figure 3.3: Metal box on purple lifting platform covered with aluminum foil to fully isolate the radiation chamber. On the right view inside radiation chamber showing the radiated area with the glass capillary in the center of it.

With an upgraded radiation source, the focus shifted to improving the polyethylene tubing on the copper tube.

3.2.2 Integration of glass capillaries

The polyethylene tubing from *Intramedic* was in general used to connect the different parts of the experimental setup with one another. However, due to the opacity of the tubing itself and its small diameter causing a very high curvature, the intensity of the UV-radiation reaching the droplets, initiating the free radical polymerization, was significantly reduced. To overcome these challenges caused by the polyethylene tubing within the irradiated area the idea was to replace the tubing with a glass capillary, thereby reducing the absorption and deflection of the UV-radiation. In the following different attempts to integrate varying types of glass capillaries and the challenges faced will be described in more detail.

3.2.2.1 Integration of a glass spiral

The first idea for a glass capillary was a glass spiral. It allows the radiation source to be placed at its center for continuous irradiation of the droplets. The glass spiral was further fitted with two needle connection-fits to connect it to the rest of the experimental setup. Both the glass capillary and the connection setup are visible in **figure 3.4**.

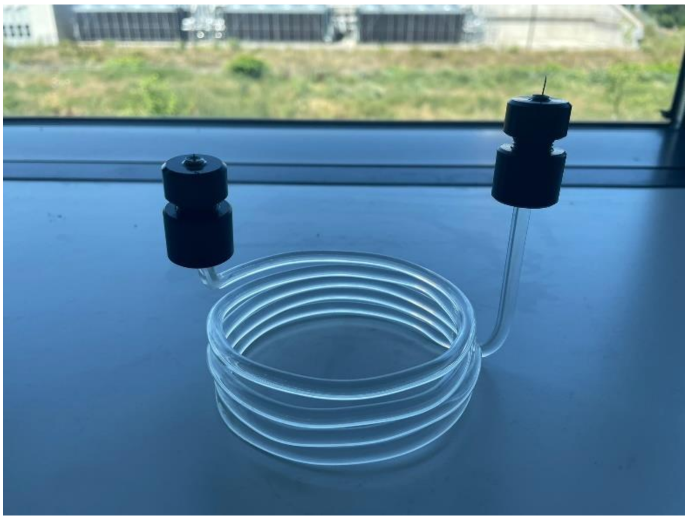

Figure 3.4: Glass spiral with its needle connection on both ends. The radiation source can be placed in the center to evenly irradiated the circling droplets.

After beginning the microfluidic experiments however challenges with the connection of the glass spiral to the rest of the experimental setup arose. Firstly, the needles, whilst easily connectable with the polyethylene tubing, started to leak during the experiment with no droplets entering the spiral. To seal the leakage at the connection of needle and tubing, epoxy glue is a possibility, however such a seal would be hard to break following the end of the experiment, thereby diminishing the reusability of the glass spiral for a second experiment. Further the large time investment needed to have one glass spiral fabricated exacerbated its lack of reusability.

With both of these challenges of the glass spiral limiting its usefulness an alternative was searched for, with increased reusability and availability. As a possible alternative fused silica capillaries were found and tried to be integrated next.

3.2.2.2 Integration of fused silica capillary

The fused silica capillary with an outer diameter of 435 µm and an inner diameter of 320 µm are purchasable from *"Chromatographie Handel Müller"* making them readily available. The capillaries size is ideal to simply insert the capillary into the polyethylene tubing of the experimental setup with the polyethylene tubing's inner diameter of 370 µm securing a leak free seal. Further the length of the capillary could be varied by using short polyethylene tubing stretches to create a ladder structure of glass capillaries linked with polyethylene tubing as depicted in **figure 3.5**.

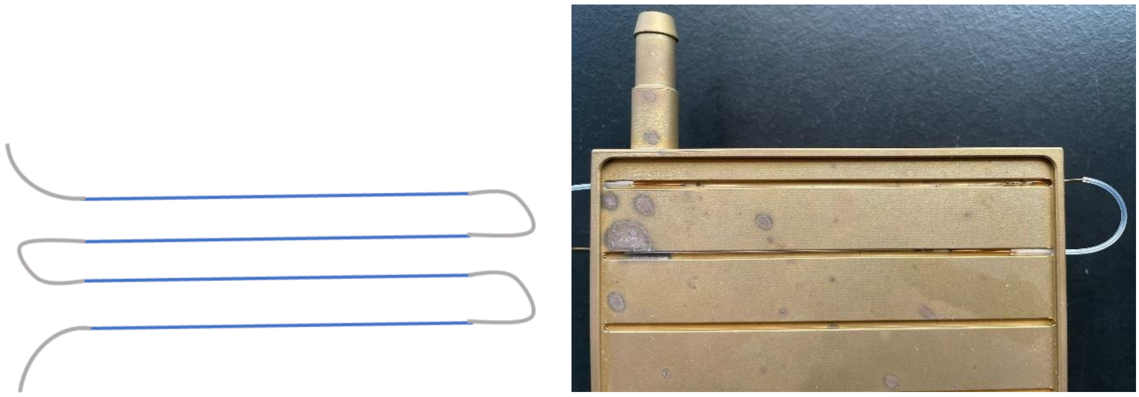

Figure 3.5: On the right a sketch of the ladder system with the fused silica capillary in blue and the polyethylene tubing in grey. On the right picture of two fused silica capillaries connected via polyethylene tubing in the ladder system. The two fused silica capillaries are within a temperature control device designed with and made in the workshop from brass metal.

To enable temperature control of this ladder system a temperature control device was designed and fabricated in house and is depicted in figure 3.5 on the right-hand side.

During experiments with the fused silica capillary integrated into the setup one severe challenge arose. Due to the capillary being inserted into the tubing the shear forces on the droplets during their entering of the fused silica capillary were too great, destroying the emulsion and creating instead segments of dispersed and continuous phase. These segments could no longer be polymerized without clogging the experimental setup.

To overcome this challenge the emulsion would have to be further stabilized for example by increasing the concentration of the surfactant, as long as the critical micelle concentration is not yet reached. In this case the shear forces acting on the droplets were however too great to overcome. Trying to initiate the polymerization prior to the droplets entering the first glass capillary would also have a stabilizing effect, however the entire point of the integration of the glass capillaries into the experimental setup was to initiate the reaction within the glass capillary.

In summary the fused silica capillary solved the problem of the leakage at both ends faced by the previously used glass spiral and was readily availability in comparison to the glass spiral. Nevertheless, it could not be successfully integrated into a working microfluidic experimental setup to create microparticles, as the shear forces acting on the emulsion upon entering the first fused silica capillary destroyed the emulsion. A challenge which was impossible to overcome by this type of capillary.

To minimize the shear forces on the droplets entering the capillary the size of the capillary would have to be large enough to allow the polyethylene tubing to be inserted into it, the opposite of what was done with the fused silica capillary. This would lead to the final approach of integrating a glass capillary with a large inner diameter into the microfluidic setup.

3.2.2.3 Integration of a glass capillary with a large inner diameter

As glass capillary a borosilicate glass capillary with an inner diameter of 1.18 mm was chosen. This allows the polyethylene tubing with an outer diameter of 1.09 mm to fit into the glass capillary, thus reducing the shear forces on the droplets prior to their polymerization. Overcoming this challenge however required a new solution to prevent any leakages at the connection points of the glass capillary and the polyethylene tubing. As seen in **figure 3.6**.

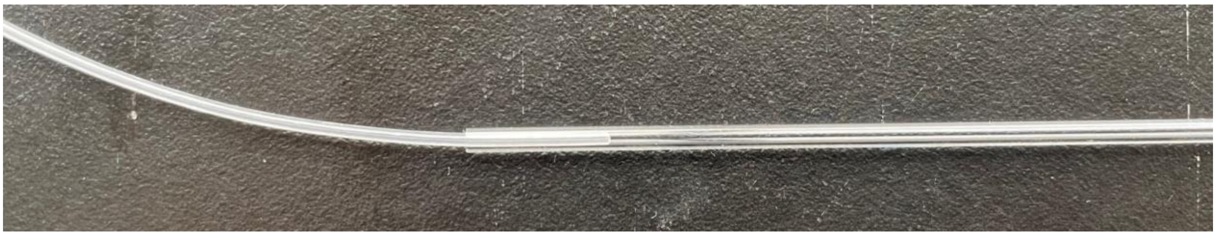

Figure 3.6: Glass capillary to be integrated into the microfluidic experimental setup. Its inner diameter is large enough to insert the polyethylene tubing, however the connection point has to be sealed.

One solution to seal the connection points is epoxy glue. These epoxy seals, as already used in the creation of glass microfluidic devices (see **1.1.3.4**) would prevent any leakage, however on the exiting side, the polymerizing droplets would again be exposed to extreme shear forces as the inner diameter would reduce from 1.18 mm of the glass capillary to the inner diameter of the polyethylene tubing of 0.38 mm. A viable solution to this challenge is heat shrink tubing. Heat shrink tubing from *Heidemann* would shrink from a diameter of 2 mm down to 0.75 mm, effectively sealing both the entering point of the polyethylene tubing into the glass capillary and the exit point further allowing the creation of a funnel at this end. This leads to a more gradual decline of the inner diameter down from 1.18 mm to the minimum inner diameter of the heated shrinking tubes of 0.75 mm. This reduces the final change of the diameter at the exit point of the glass capillary from 0.9 mm to 0.37 mm as sketched in **figure 3.7**.

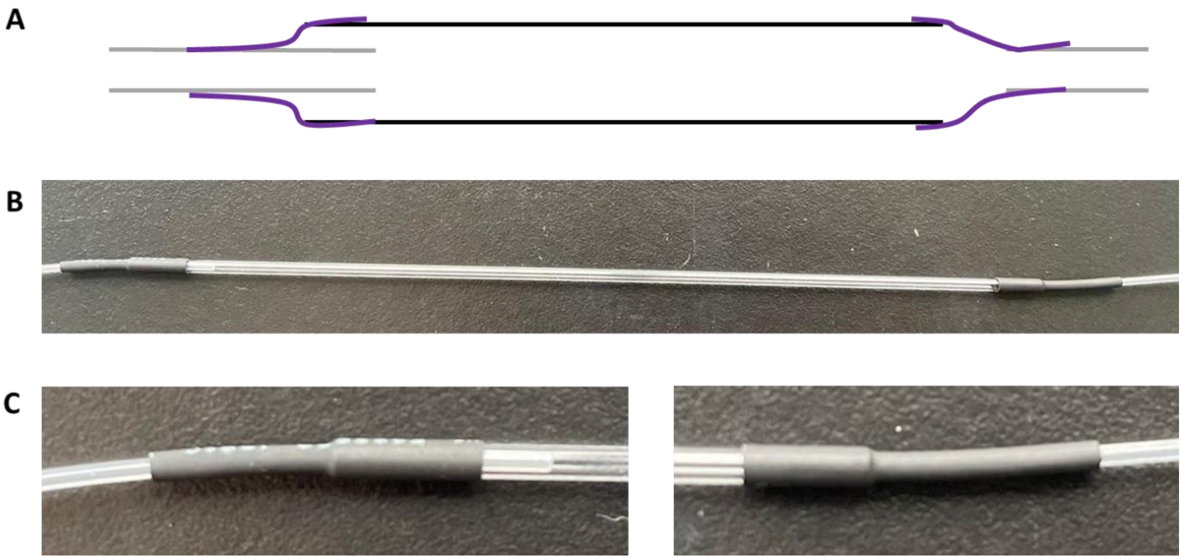

Figure 3.7: (A) Sketch of glass capillary (black), which is connected to the polyethylene tubing (grey) via shrinking tubes (purple). On the left side, where the droplets enter, the tubing is inserted into the glass capillary to reduce shear forces on the droplets. On the right side, where the polymerizing droplets exit the shrinking tube creates a sort of funnel reducing the shear forces while exiting the glass capillary. (B) Image of the glass capillary ready for use. (C) Close up of both ends of the glass capillary with the shrinking tubing attached.

With the glass capillary successfully integrated into the experimental setup the modified setup schematically was as depicted in **figure 3.8**.

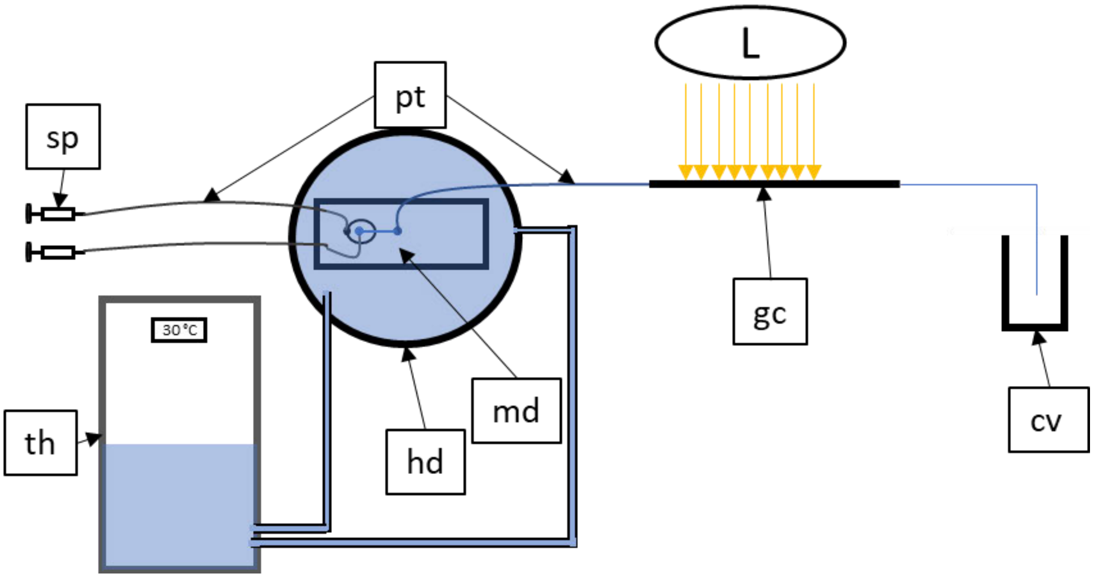

Figure 3.8: Sketch of modified microfluidic experimental setup. Including the OmniCure series 1500 from Excelitas as the new UV-source (L) and the glass capillary (gc). (sp) represents the syringes within the syringe pumps, (th) the thermostat, (hd) the microfluidic chip heating advice containing the microfluidic chip (md). (Pt) is the polyethylene tubing connecting the different parts of the device and (cv) the collection vessel.

During initial microfluidic experiments using the modified microfluidic setup the droplet creation was very stable during the beginning part of the experiments. However, once the irradiation of the droplets was initiated the droplet creation was majorly influenced by both the distance and resulting intensity of the UV-radiation. This instability of the droplet creation as depicted on the top right of **figure 3.9** resulted in jetting and wetting of the side of the device of the dispersed phase. This did not only decrease the monodispersity of the microgels but also led to the creation of segments of dispersed phase inside the polyethylene tubing. These segments once within the glass capillary formed spherical droplets, which once the polymerization was imitated became too rigid to exit the glass capillary again, resulting in a blockage. This blockage increased the pressure inside the glass capillary until one of the two seals of the shrinking tube ultimately ruptured, resulting in no yield of microparticles.

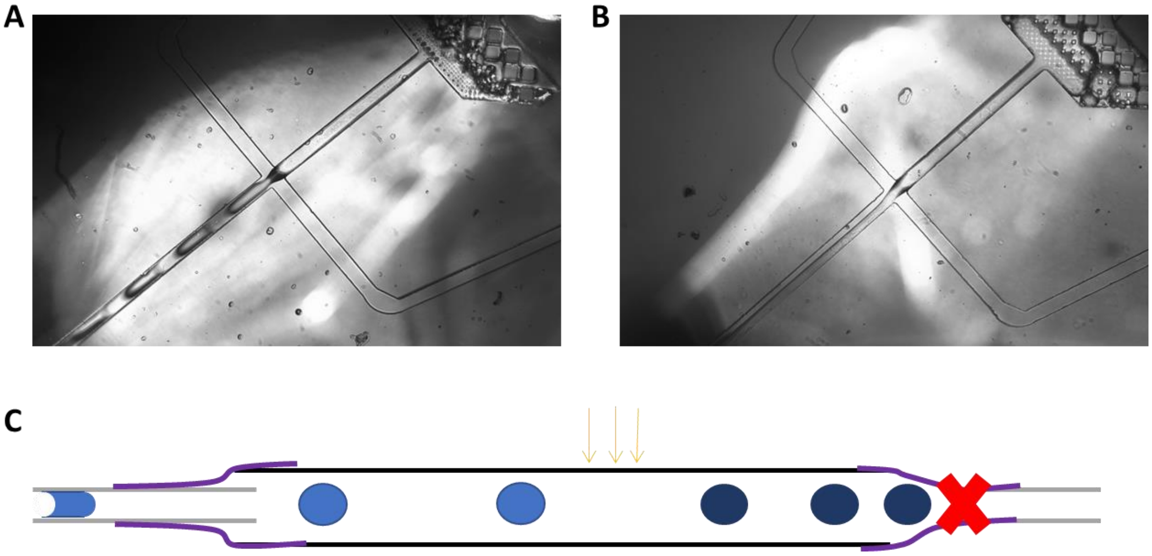

Figure 3.9: (A) stable droplet creation prior to irradiation of the droplets. (B) jetting of the dispersed phase and wetting on the right side of the exiting channel of the microfluidic device. (C) sketch of the effect of segments of the dispersed phase after irradiation. The segments can still enter the glass capillary forming droplets too large to exit the glass capillary once they have been irradiated (dark blue) leading to a buildup of pressure that eventually breaks the seal on the right.

Whilst jetting is, as described in the theoretical background, a result of imperfect flowrate ratios of both the continuous and dispersed phase, wetting can be caused due to the hydrophilic nature of both the dispersed phase and the PDMS microfluidic device. Though PDMS is naturally hydrophobic and the glass slide is hydrophilic during the oxygen plasma bonding of the device, part of the PDMS surface becomes hydrophilic in the form of silanol groups. These then react with the glass to form Si–O–Si bonds fusing PDMS and glass together as depicted in **figure 3.10**.[2] However, the micro-channel walls of the PDMS do not bond to the glass surface resulting in the PDMS to gain a partially hydrophilic nature in PDMS devices.

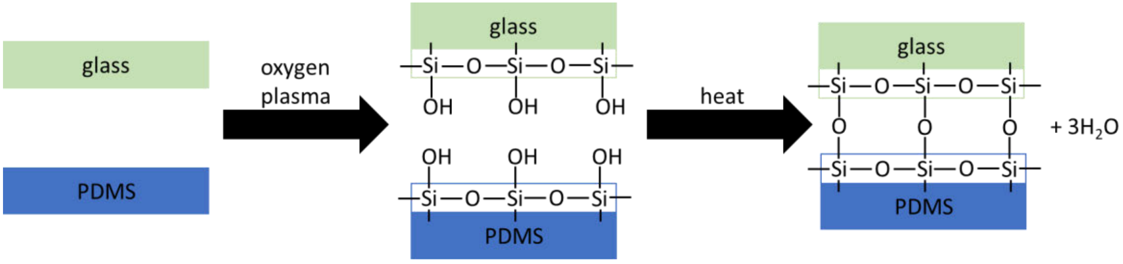

Figure 3.10: PDMS and glass slide covalently bonded after treatment with oxygen plasma.[2]

In order to regain the hydrophobic nature of the PDMS micro-channels and even coat the free glass surface hydrophobic compounds as for example *Sigmacote*® from *Merck* can be used. They contain chlorinated organopolysiloxanes which can react with the free silanol groups.

Using *Sigmacote*® prior to the microfluidic experiments resulted in the droplet creation to remain stable after the irradiation of the droplets commenced. Therefore, a working microfluidic setup with an integrated glass capillary was achieved. Successful microgel synthesis was achieved with flowrates of the dispersed phase of 250 $\frac{\mu L}{h}$ and the continuous phase of 500 $\frac{\mu L}{h}$.

3.3 Conclusion of project I

In summary the aim to increase the yield of an already existing microfluidic experimental setup was achieved by completely remodeling the reaction segment of the microfluidic setup. The reaction segment formerly was composed of the *Black-Ray B-100 AP High Intensity UV lamp* and the polyethylene tubing wrapped around a copper tube for temperature control.

To increase the UV-radiation of the microfluidic droplets the UV lamp was changed to the *OmniCure series 1500*, which not only contains a more powerful radiation source but also allows the intensity to be focused on a much smaller area than the previous UV lamp.

To further increase the intensity of the irradiation of the droplets the polyethylene tubing was changed to a glass capillary. Several different glass capillary types were tested resulting in the final successful integration of a glass capillary with a large inner diameter into the experimental setup. Using shrinking tubing the challenges of sealing the connection points of the glass capillary and the polyethylene tubing and minimizing the shear forces at the exiting point were overcome and challenges with the droplet creation stability were resolved by hydrophobically coating the PDMS device.

The resulting modified microfluidic setup was successfully used to synthesize microparticles at flowrates of 250 $\frac{\mu L}{h}$ for the dispersed phase and 500 $\frac{\mu L}{h}$ for the continuous phase. These flowrates are more than twice as high as the previous flowrates of the old microfluidic setup therefore significantly increasing the overall yield of the microfluidic experimental setup.

3.4 References

[1] © 2024 Excelitas Technologies Corp., *OmniCure S1500 UV Aushärtungssystem* **2024**, https://www.excelitas.com/de/product/omnicure-s1500-uv-curing-system.

[2] L. Xiong, P. Chen, Q. Zhou, *Journal of Adhesion Science and Technology* **2014**, *28*, 1046.

4. Project II: Core-shell interfacial interpenetration control for switchable elasticity

In "*area D – Microgels: Core-shell interfacial interpenetration control for switchable elasticity*" of the GRK 2516 the aim was to create core-shell microgels, with a switchable elasticity. This change in elasticity is achieved by the interconnection of a temperature insensitive shell and a temperature sensitive core made of a polymer with LCST-behavior. The elasticity is quantified in terms of the Young's modulus. Furthermore, the direction of the change of the Young's modulus upon a change in temperature is dependent on the interpenetration of the shell and core polymer. Controlling this interpenetration is therefore a further aim of this project.

There are two possible extreme cases of the interpenetration of the shell and core. In the first case the core and shell are not connected at all. In this case with increasing temperature the core would collapse due to its temperature sensitivity. This collapse would lead to an empty space into which the shell swells thereby decreasing its density and the Young's modulus of the core-shell particle.

In the case of a fully connected core and shell, the cores collapse at increased temperatures and pull on the shell due to the interconnection, increases both the shells density and the Young's modulus (see **figure 4.1**).

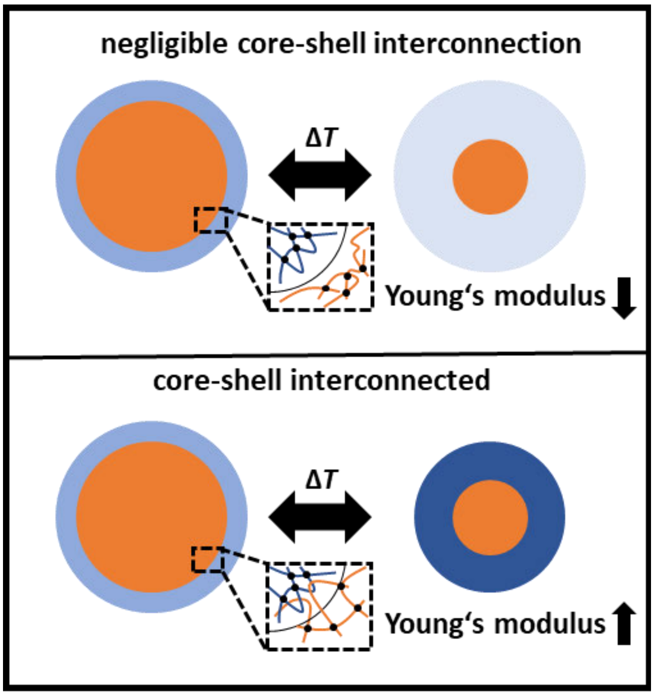

Figure 4.1: Effect of core collapse on core-shell particle with different interconnection of core and shell. On the top the negligible core shell interconnection leads to a swelling of the shell into the empty space decreasing the density of the shell as well as the Young's modulus. In contrast if the core and shell is interconnected, the shell density increases as it is pulled into a smaller space. The Young's module in this case also increases.[1]

To create such core-shell particles droplet-based microfluidics is the synthesis method of choice, as in previous research this method had already been successfully used.[1] In a first step the cores are synthesized, using a microfluidic setup as already depicted in figure **1.1A**. This is followed by the creation of a double emulsion with non-crosslinked shell polymer surrounding the pre-synthesized core in a second microfluidic experiment. After crosslinking the shell polymer via UV exposure any interconnectivity of the shell polymer and the core would be frozen. The interconnectivity is a result of diffusion of the linear shell polymer, from now on named shell-precursor polymer, into the core polymer network. A schematic of the microfluidic device used for the creation of the core-shell particles is shown in **figure 4.2**.

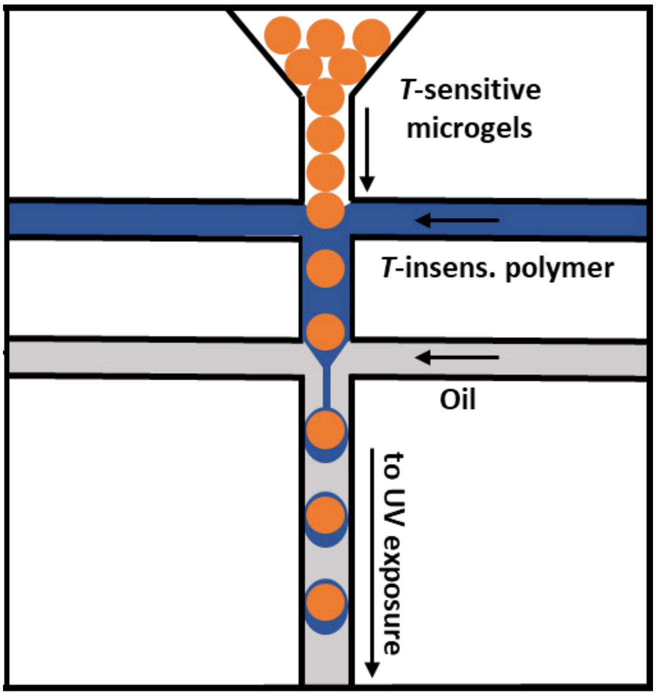

Figure 4.2: Schematic of the microfluidic setup with two cross-sections. At the first cross-section the pre-synthesized core-particle is engulfed by the temperature insensitive shell precursor polymer, which together form the core-shell droplet at the second cross-section. UV radiation crosslinks the shell precursor polymer thereby creating the core-shell microparticles.

In the following each step to create the core-shell particles will be described in more detail with Project II.1 (chapter 5) focusing on the core-particle synthesis. Project II.2 (chapter 6) describes the synthesis of the shell-precursor polymer, as well as, the photosensitizer needed for the later crosslinking thereof. Finally in Project II.3 (chapter 7) the final core-shell synthesis alongside the challenges with the UV exposure is the main topic. Furthermore, the tandem project analyzing diffusion simulations of linear polymers into a polymer network are discussed in Project II.3.

4.1 References

[1] M. Seuss, W. Schmolke, A. Drechsler, A. Fery, S. Seiffert, *ACS applied materials & interfaces* **2016**, *8*, 16317.

5. Project II.1: Core-particle synthesis

5.1 Introduction and aim regarding the core-particle synthesis

Within this first part of this project the aim was to create cores made of poly *N*-isopropylacrylamide (poly-NIPAM) using microfluidics. These cores have to meet two key criteria: Firstly, the cores have to be monodisperse in size to ensure comparability of the effect of the cores' collapse once the core-shell particles had been synthesized. Secondly, the microfluidic setup for the cores has to be able to produce a large quantity of core-particles, since this is a requirement for the core-shell microfluidic experiment later on. The general composition of the cores is determined by the dispersed phase listed in **table 5.1**.

Table 5.1: Composition of the dispersed phase and the continuous phase for the microfluidic experiments to create the core-microgels.

	Monomer (g)	**Crosslinker (mol% of NIPAM)**	**Initiator ($\mathbf{g \cdot L^{-1}}$)**	**Water (g)**
dispersed phase	0.5	1	8	5

The microfluidic setup for the creation of the core-particles was a single cross-section microfluidic device made of PDMS or glass depending on the intended size of the microfluidic channels and the resulting core-particles. In all cases the dispersed phase consists of an aqueous solution of the monomer NIPAM and crosslinker *N,N'*-methylenebisacrylamide (MBAA) with concentration as listed in table 5.1. The continuous phase is composed of low viscosity paraffin oil with PGPR90 (10 wt%) as surfactant. As initiator APS was used in conjunction with TEMED, just as described in **1.1.3.6.** To prolong the possible creation of core droplets as long as possible the TEMED was located within the collection vessel as a highly concentrated TEMED continuous phase mix (4 mL TEMED in 10 mL continuous phase), thus no polymerization could influence the droplet creation over time.

There were several different microfluidic experiments done using microfluidic devices with differing channel sizes, the results of which are described in the following. The devices will be named according to their channel sizes, for example a 100 µm device is a microfluidic device with channel sizes of 100 µm in height and width at the cross-section.

5.2 Preliminary core creation microfluidic experiments

Keeping the two desired criteria of monodisperse size distribution and adequate quantity of the yield in mind the core-particle production was optimized using microfluidic devices with channel heights and widths of 25, 50 and 200 µm. In the case of the 25 and 50 µm channel sized devices PDMS was used. For the microfluidic device with 200 µm channels a glass microfluidic device with a grinded tapered round glass capillary was created. All devices were self-made using the methods as described in chapter **1.1.3.4**. Though in all experiments dispersed and continuous phases of the same composition were used, the flowrates had to be optimized for each channel size. The optimized flowrates, at which a stable production of monodisperse droplets took place, are summarized in **table 5.2**.

Table 5.2: Optimized flowrates of the dispersed and continuous phase for the microfluidic devices with channel sizes of 25, 50 and 200 µm.

channel size (µm)	**flowrate of dispersed phase (µL· h^{-1})**	**flowrate of continuous phase (µL· h^{-1})**
25	40	150
50	35	160
200	1500	4000

Though using the optimized flowrates core-particle syntheses in all cases were successful, none of the yields fulfilled both of the beforementioned criteria’s resulting in the cores not being applicable for the overall aim to create core-shell microparticles with varying degrees of interconnectivity of the two. The reasons for the exclusion of the core-particles are described in the following in more detail.

5.2.1 Reasons for exclusion of the core-particles from the 25 and 50 µm devices

As the initial targeted size of the core-particles was 50 µm the microfluidic channels were tried to be kept as small as possible to create cores in the targeted range. Both the 25 and 50 µm devices are made of PDMS and in the case of the 25 µm device the small channel size resulted in challenges arising during the creation of the devices themselves. As the PDMS-slab needs to be slightly pressed against the glass during the final bonding step this resulted in some 25 µm devices’ channels partially collapsing resulting in the shredding of the core-droplets as shown in **figure 5.1**. During the creation of 50 µm devices this problem however not arose.

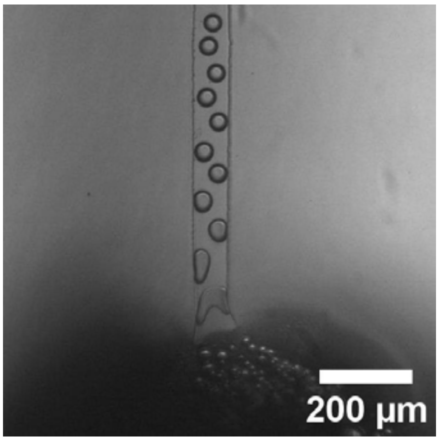

Figure 5.1: Droplets (around $35-40$ *µm) from the 25 µm device being destroyed whilst exiting the microfluidic device.*

One challenge which however did arise in both the 25 µm as well as the 50 µm devices were the extremely low flowrates as summarized in table 5.2. As the minimum targeted yield amount was around 1 mL of the dispersed phase, microfluidic experiments would have to run non-stop and without problem for days on end. This is difficult to control as there was no possibility to constantly observe the droplet creation. Alternatively multiple yields from different experiments would have to be combined.

Core-creation microfluidic experiments using 25 µm devices quickly proved not capable to fulfill the experimental time requirement as over the course of five hours the stable droplet creation would first start to jet and ultimately cease as shown in **figure 5.2**.

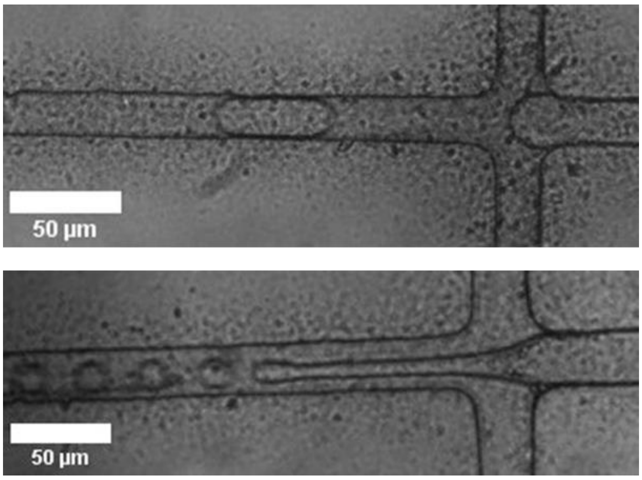

Figure 5.2: Regular droplet creation on the top. On the bottom the beginning of jetting of the dispersed phase.

Therefore, in case of the 25 µm devices the yields would have to be combined to reach the minimal core amount.

In the case of the 50 µm devices the droplet creation seemed to be stable over the duration of several days, making it therefore not necessary to combine multiple experimental yields.

The final cause of exclusion for core-particles from both 25 and 50 µm devices revealed itself during the inspection of the core-particles using light microscopy. Though in the continuous phase appearing to be monodisperse in size as shown in **figure 5.3A** this monodispersity disappeared upon swelling of the microgels in water. Figure **5.3B** shows an analysis of the polydispersity in size of the 25 µm devices yield of two experiments on the left and particle size distribution observed under the microscope of one of the yields from a 50 µm device on the right.

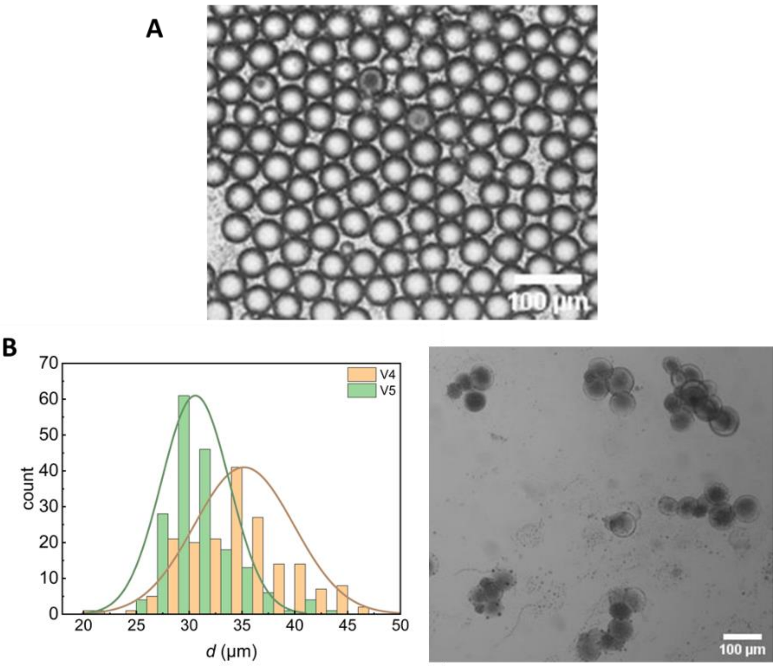

Figure 5.3:(A) Example of apparent good monodispersity of the core-particle sizes in the continuous phase from a 50 µm device. (B) size distribution of two yields from a 25 µm device in water (left) and microscopy image of the core-particles from a 50 µm device, transferred into water revealing a large size distribution (right).

The large size distribution as depicted in figure 5.3 could be an indirect result from the low flowrates necessary for stable droplet production during microfluidic experiments using 25 µm and 50 µm devices. The syringe pumps used during the microfluidic experiments were *PHD ULTRA* syringe pumps from *Harvard Apparatus*. These are mechanical pumps and at low flowrates beneath 100 $\frac{\mu\mathrm{L}}{\mathrm{h}}$ difficulties maintaining constant pressures and fluid flow seemed to occur. This fluctuation of the fluid flow could explain the high polydispersity of the particle size observed.

5.2.2 Reasons of exclusion of the core-particles from the 200 µm devices

As summarized in table 5.2 the optimal flowrates for the 200 µm devices were drastically increased in comparison to those of the 25 µm and 50 µm devices. Therefore, the previous problems with maintaining the flowrates did also not occur. In all microfluidic experiments using the 200 µm glass microfluidic devices the droplet creation was extremely uniform as depicted in **figure 5.4**. The yield amount was also more than desired, in some cases using up the entirety of the dispersed phase of 5 mL. The reason for exclusion would in this case however again be revealed upon the removal of the continuous phase and swelling of the core-particles in Milli-Q water.

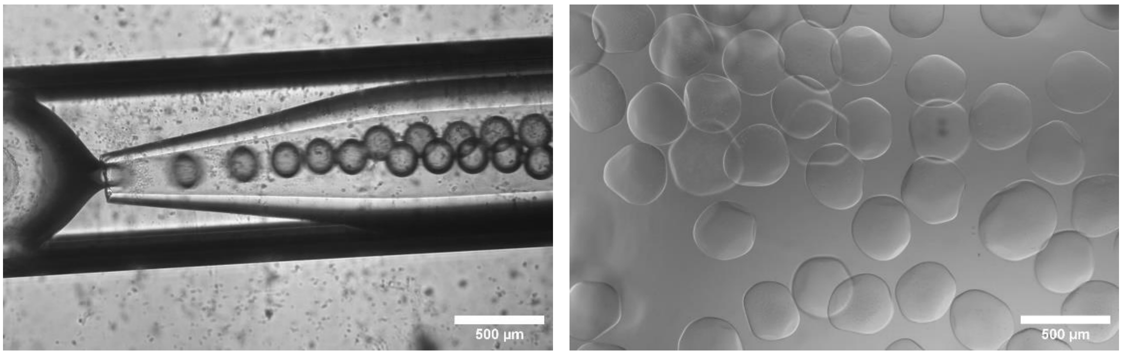

Figure 5.4: On the left, glass microfluidic experiment producing uniform droplets. On the right core particles swollen in Milli-Q water having lost their spherical shape.

As shown in figure 5.4 on the right the core-particles lose their spherical shape after swelling in Milli-Q water. This loss of shape is detrimental to the overall aim of creating core-shell particles with an evenly distributed interpenetration of the shell into the core. If the core is not spherical in shape the interpenetration depths as well as the effect of the cores collapse as described at the start of the project (see chapter 4) would not necessarily be uniform.

5.3 Final core-synthesis using 100 µm devices

After the resulting core-particles made using 25 µm, 50 µm and 200 µm devices had all not been able to fulfill the two criteria necessary to be used as cores in the desired core-shell particles with varying interpenetration depths, 100 µm devices were experimented with. The 100 µm devices were self-made PDMS devices and using the dispersed phase and continuous phase with the compositions as described in chapter 5.1 were able to create microgels with the optimized flowrates of $120\,\frac{\mu\mathrm{L}}{\mathrm{h}}$ for the dispersed phase and $700\,\frac{\mu\mathrm{L}}{\mathrm{h}}$ for the continuous phase.

The desired yield of at least 1 mL of droplets from the dispersed phase could be achieved as droplet production of a single microfluidic experiment using a 100 µm device was stable for over 24 hours. The average yield was between $2.9 - 3.3$ mL of the dispersed phase. Therefore, the combination of core-particle batches was not necessary. The final core-particles swollen in distilled water were of monodisperse size with an average diameter of $\bar{d} = 122 \pm 8$ µm and are depicted in **figure 5.5**.

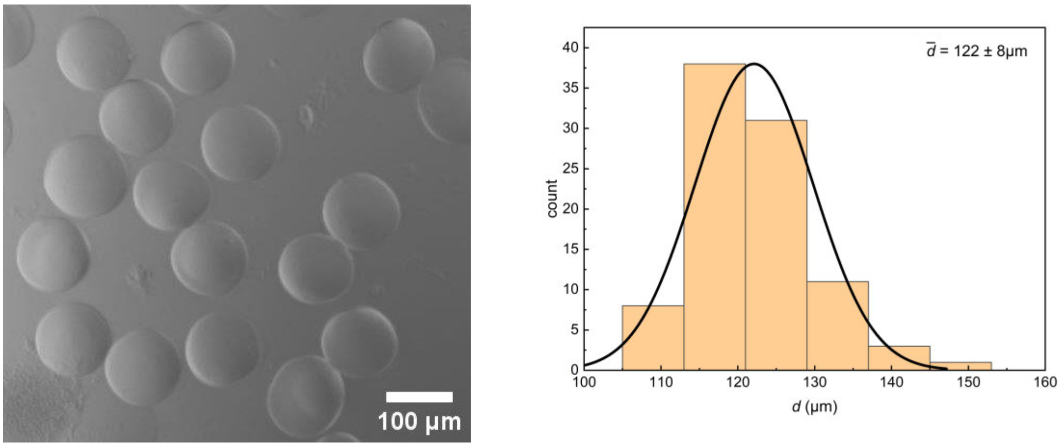

Figure 5.5: Core-particles synthesized using a 100 µm device swollen in Milli-Q water on the left. Size distribution of the core-particles with an average of 122 µm to the right.

As the microgels meet the two desired criteria of monodisperse size distribution and yield amount, these particles were chosen to be the final core-particles to be used to create the core-shell particles with varying interconnectivity of the shell and core.

The only noticeable downside to the core-particle production using the self-made 100 µm PDMS-devices came in the form of a slight size variation (~9 %) of the average core-particle from batch to batch. This size variation from batch to batch is a result from imperfections of the self-made master devices used to create the PDMS-devices themselves and will play a further role in the later chapter on the synthesis of the core-shell particles.

5.3.1 LCST investigation of the core particles

As the temperature sensitivity of the cores is curial in the regard of the switchable elasticity as described in chapter 4, the core particles LCST behavior was analyzed.

To do this a small core-particle sample of around 30 particles in Milli-Q water was placed in a small confined space made of an adhesive silicone isolator with a depth of 1 mm and two small microscopy slides. The sample was then placed into a thermal controller and placed under an inverse microscope (*Zeiss Axio*). Using a computer-controlled thermostat, the temperature of the sample was slowly increased from 20 °C to 50 °C in 1 °C steps from 20 – 27 °C, and thereafter by 0.5 °C steps until the end. After each temperature step, the sample was left to equilibrate for 10 minutes and then an image taken. Using the program *ImageJ* the diameters of the core-particles were measured in relation to the temperature and averaged. **Figure 5.6** depicts the change of the average diameter of the core-particles d_{T} at a certain temperature T with d_0 the average diameter of the core particles at 20 °C.

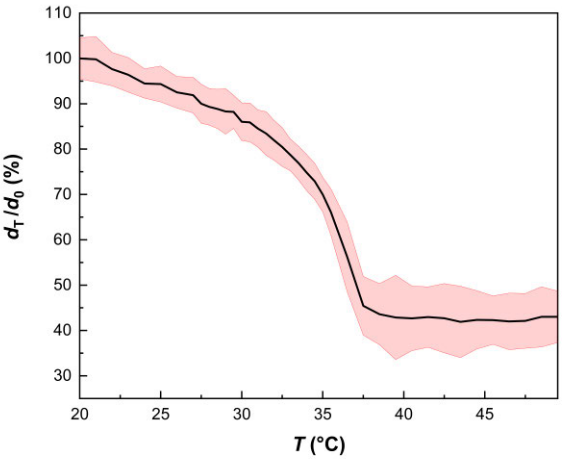

Figure 5.6: Change of the core-particles diameter with the temperature. Beginning at 32°C a sharp decline of the particle sizes is noticeable in accordance with the lower critical solution temperature (LCST) of poly-NIPAM. In red the error range of the particle diameter change.

As shown in figure 5.6 the core-particles made of poly-NIPAM show LCST behavior, with the diameter at first slowly decreasing from 20 – 32 °C after which the poly-NIPAM particles rapidly shrink to around 40 % of their original size. This significant change in size should be adequate for the desired effects to take place in the core-shell particles resulting in the switchability of the elasticity of the later core-shell particles.

6. Project II.2: Shell-precursor preparation

6.1 Introduction and aim of the project

The focus of this chapter is on the synthesis of the shell-precursor polymer with the criteria of being temperature insensitive and crosslink-able via UV-radiation as depicted in figures 4.1 and 4.2.

The chosen shell-precursor polymer fulfilling these two criteria is a copolymer of acrylamide (AAm) and *N*-(2-(3,4-dimethyl-2,5-dioxo-2,5-dihydro-1H-pyrrol-1-yl)ethyl)acrylamide (DMMIAAm). AAm as the main monomer is temperature insensitive and DMMIAAm as comonomer has a cross-linkable side group, allowing the crosslinking of the linear copolymer in the presence of the triplet-photosensitizer thioxanthone-2,7-disulfonate (TXS) using UV-radiation as shown in **figure 6.1**.

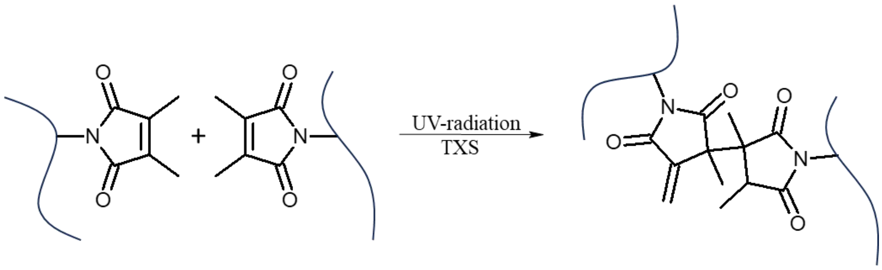

Figure 6.1: Dimerization reaction of DMMIAAm side group in presence of the photosensitizer TXS, crosslinking the previously linear shell-precursor polymer to create the shell polymer-network of the core-shell particles.

Photo-crosslinking is the method of choice in this case as it allows good control over the diffusion-time of the linear shell-precursor polymer into the core-particle by control over the time of irradiation. Once the droplet is irradiated the diffusion should cease and various interconnection extents can be realized based on the penetration depths.

In the following the three separate syntheses, of the crosslinker DMMIAAm, the triplet photosensitizer TXS and the shell-precursor polymer, are described in more detail.

6.2 Synthesis of the photo-crosslinker *N*-(2-(3,4-dimethyl-2,5-dioxo-2,5-dihydro-1H-pyrrol-1-yl)ethyl)acrylamide (DMMIAAm)

The synthesis of *N*-(2-(3,4-dimethyl-2,5-dioxo-2,5-dihydro-1H-pyrrol-1 yl)ethyl)acrylamide from now to be referred to as DMMIAAm is based on a synthesis route published by Seuss et al..[1] The four step synthesis starting with ethylenediamine is depicted in **figure 6.2**. All products (**1**, **2**, **3** and **4**) were characterized using ^{1}H-NMR spectroscopy, the corresponding spectra can be found in the Appendix **A1**.

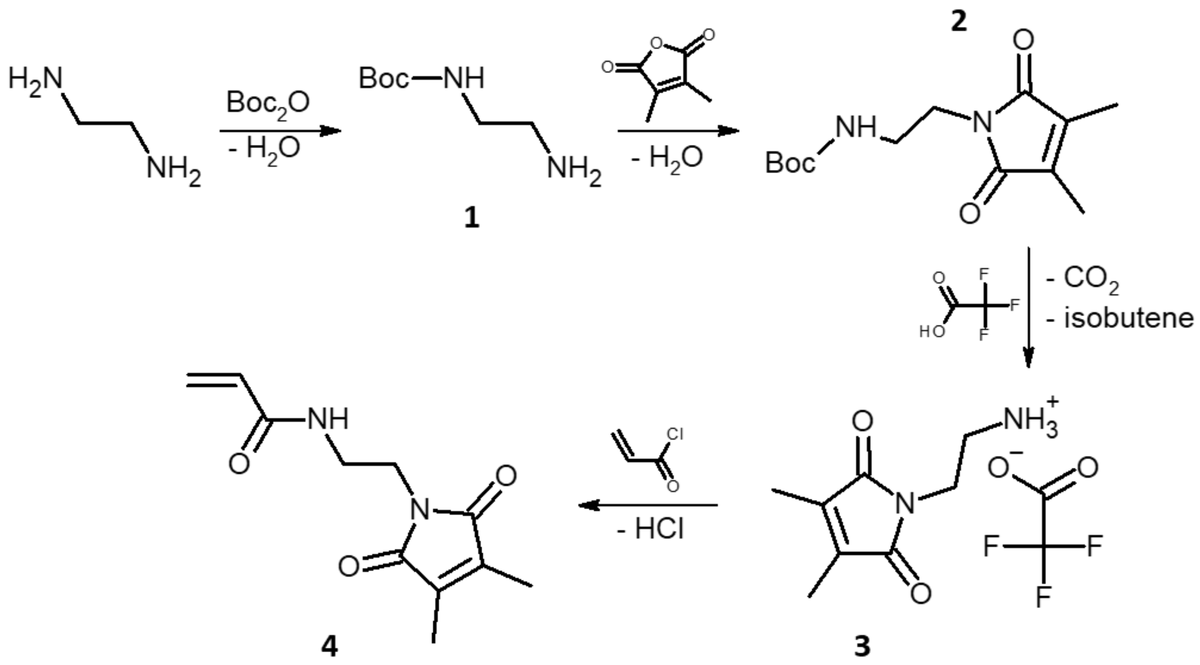

Figure 6.2: Synthesis route of the photo-crosslinker DMMIAAm starting with ethylenediamine.[1]

As shown in figure 6.2 during the first step of the synthesis of the crosslinker, tert-butyl (2-aminoethyl) carbamate (see figure 6.2 (**1**)) is synthesized using ethylenediamine and ditert-butyl-dicarbonate. Both chemicals were dissolved in 1,4-Dioxane and the ditert-butyl-carbonate was added dropwise. The mixture was stirred rapidly for about 2 days. The formed precipitate was removed and the solvent alongside the excess ethylenediamine was removed in vacuo. Ditert-butyletane-1,2-diyldicarbamate was filtered off after its precipitation following the addition of water. The aqueous phase was saturated with sodium chloride and extracted using dichloromethane. The combined organic phase was then dried and the solvent removed to obtain the crude product as a yellow oil, purified using vacuum distillation. The pure product was a colorless oil. ^{1}H-NMR (400 MHz, $CDCl_3$): δ 1.29 (s, 9H, CH_3, BOC), 2.62 (m, 2H, $\mathbf{CH_2} - NH_2$), 2.99 (m, 2H, $\mathbf{CH_2} - NH$), 5.36 (br. s, 1H, NH) ppm.

In the second step of the synthesis tert-butyl (2-aminoethyl) carbamate was dissolved in toluene along with dimethyl maleic anhydride. The solution was refluxed for 3 hours using a water separator. The product tert-butyl (2-(3,4-dimethyl-2,5-dioxo-2,5-dihydro-1H-pyroll-1-yl)ethyl)carbamate (**2**) was obtained after removing the solvent and drying the precipitate in vacuum. ^{1}H-NMR (400 MHz, $CDCl_3$): δ 1.40 (s, 9H, tert-butyl-O), 1.96 (s, 6H, $2CH_3$, maleic), 3.31 (m, 2H, $\mathbf{CH_2} - NH$), 3.61 (m, 2H, $\mathbf{CH_2} - N$), 4.78 (br. s, 1H, NH) ppm.

Next tert-butyl (2-(3,4-dimethyl-2,5-dioxo-2,5-dihydro-1H-pyroll-1-yl)ethyl)carbamate was dissolved in dichloromethane and trifluoroacetic acid was added. After an hour of stirring the crude product was obtained after removing the solvent in vacuum. To the crude product water was added and the pH raised to pH = 8 using diethyl amine. The product was extracted from the aqueous solution using ethyl acetate, which was in the following removed via vacuum. Excess diethyl amine within the product was removed after suspension of the crude product in dichloromethane and filtering. The product 2-(3,4-dimethyl-2,5-dioxo-2,5-dihydro-1H-pyrrol-1-yl)ethan-1-aminium 2,2,2-triffluoroacetate (**3**) was dried overnight in vacuum and appears as a colorless solid. ^{1}H-NMR (400 MHz, DMSO-*d*$_6$): δ 1.90 (s, 6H, 2CH_3), 2.93 (m, 2H, $\mathbf{CH_2} - NH_3^+$), 3.62 (t, *J* = 6.05 Hz, 2H, $\mathbf{CH_2} - N$), 7.78 (s, 3H, NH_3^+) ppm.

As the last step in the synthesis the previous product is dissolved in dichloromethane alongside sodium carbonate and acryloyl chloride is added slowly at 0 °C. After complete addition the colorless suspension is stirred for a further two days at room temperature. The product *N*-(2-(3,4-dimethyl-2,5-dioxo-2,5-dihydro-1H-pyrrol-1 yl)ethyl)acrylamide (**4**) or DMMIAAm is obtained after filtration of the suspension and removing of the solvent in vacuo. ^{1}H-NMR (400 MHz, $CDCl_3$): δ 1.98 (s, 6H, 2CH_3), 3.51 (m, $\mathbf{CH_2} - NH$), 3.73 (m, $\mathbf{CH_2} - N$), 5.62 (dd, *J* = 10.3, 1.4 Hz, $\mathbf{CH_2}$), 6.06 (dd, *J* = 17.0, 10.3 Hz, $\mathbf{CH_2}$), 6.23 (dd, J = 17.0, 1.4 Hz, $\mathbf{CH_2}$ und br. s, NH) ppm.

6.3 Synthesis of shell-precursor polymer

After synthesis of the crosslinker DMMIAAm, as described in 6.2, the shell-precursor polymer was synthesized. The polymerization method used to create the poly AAm-co-DMMIAAm was free radical polymerization. The mechanism of the free radical polymerization has already been introduced in chapter **1.1.3.6** and for the synthesis of the shell-precursor polymer the initiator pair TEMED and APS were used.

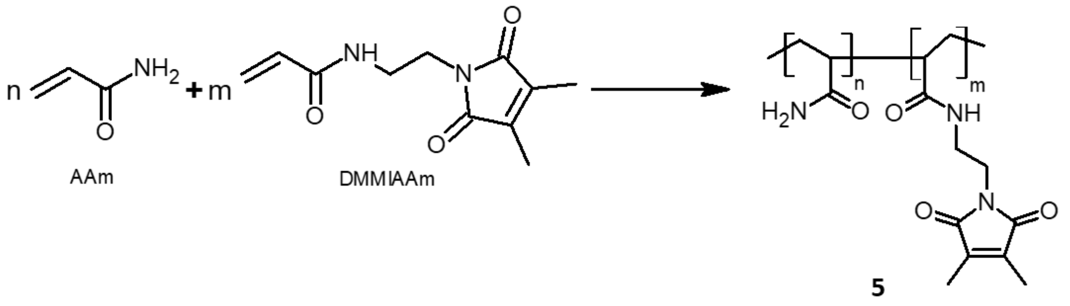

Figure 6.3: Polymerization reaction of AAm and DMMIAAm to form the statistical shell-precursor poly acrylamide-co-DMMIAAm.[1]

For the polymerization both acrylamide (3.97 g, 55 mmol) and DMMIAAm (**4**) (0.39 g, 2 mmol) are dissolved in water (125 mL) along sodium formate (0.18 g, 2.6 mmol) for control of the molecular weight. The solution is purged using argon for two hours at room temperature and initiated using 100 mg of APS dissolved in 2.3 mL of water and 0,2 mL of TEMED. The polymerization is monitored by taking samples every 30 minutes and adding them to excess methanol to check for precipitation. After about two hours noticeable precipitation was observed and the reaction was terminated by addition of 750 mL of methanol. The precipitate was filtered and dialyzed against Milli-Q water for one week. The shell-precursor polymer (**5**) is a white solid. ^{1}H-NMR (400 MHz, D_2O): $\delta\ 1.4 - 2.4$ (b, m, polymer backbone and DMMIAAm methyl group protons), $3.2 - 3.7$ (4H, CONH–**$(CH_2)_2$**–DMMI) ppm.

The percentage of the DMMIAAm within the copolymer was determined via ^{1}H-NMR of the copolymer using the approach by Seuss et al..[1] According to the approach, the NMR signal at $\delta = 3.20 - 3.75$ ppm was set to 4 representing the methylene chain between the amide and DMMI group, and the ratio determined using the signal at $\delta = 2.4$ ppm to determine the ratio, by reducing the integrals value by nine (3 backbone protons and 6 methyl protons of each DMMIAm) and then dividing it by three cause of each acrylamide residue. The determined ratio of DMMIAAm in the shell-precursor polymer is 27 %. The determined ratio is a bit higher than anticipated (10 %), however this increased ratio should not be problematic.

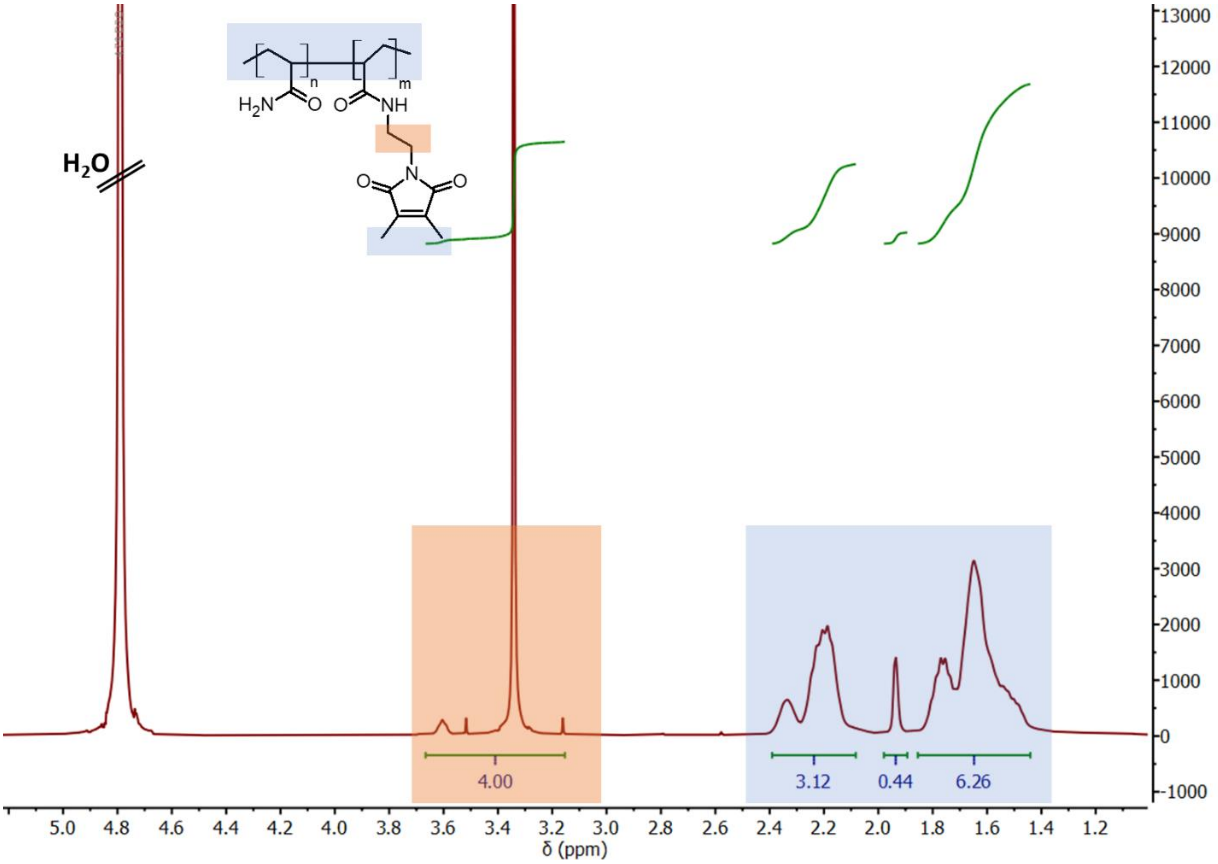

Figure 6.4: ^{1}H-NMR of the copolymer used to determine the percentage of DMMIAAm in the shell-precursor polymer.

6.4 Synthesis of thioxanthone-2,7-disulfonate (TXS)

Lastly after successful synthesis of the shell-precursor polymer, the photo-sensitizer thioxanthone-2,7-disulfonate or from now to be abbreviated as TXS had to be synthesized. TXS is needed for the dimerization reaction of the DMMIAAm within the shell-precursor polymer, effectively crosslinking the linear polymer chains to create a 3D-polymer network. The synthesis of TXS was published by Kronfeld and Timpe[2] and is depicted in **figure 6.5**.

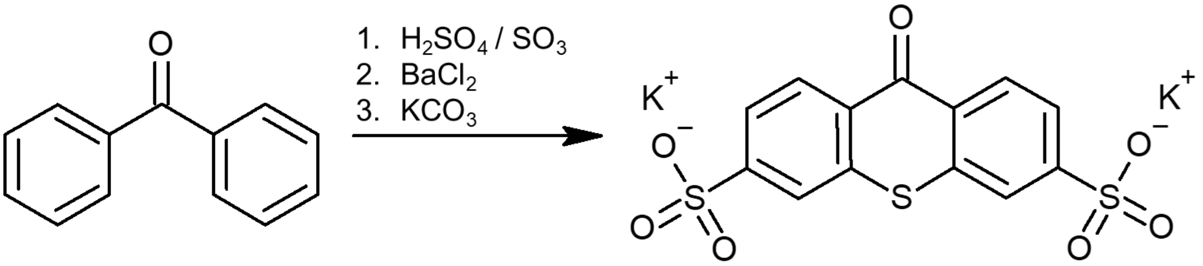

Figure 6.5: Synthesis of TXS according to the synthesis protocol of Kronfeld and Timpe.[2]

Benzophenone (5 g, 27 mmol) was dissolved in fuming sulfuric acid (100 mL) and heated for 2.5 hours. Then it was cooled to room temperature and added to 300 g of ice. Excess sulfuric acid was neutralized using calcium carbonate and the gibs filtered off, followed by addition of barium chloride (5 g) to the clear filtrate and the barium salt filtered off. After purification of the barium salt via recrystallization it was dissolved in water and potassium carbonate added. After removal of the barium carbonate diluted sulfuric acid was added to the solution and the solvent removed in vacuo. The crude product was washed several times and finally dried. For the use of the TXS in the microfluidic experiments a solution of TXS in water with the concentration of $1\,\frac{\mathrm{g}}{\mathrm{L}}$ was prepared and successfully used to crosslink the prepared shell-precursor polymer using UV-radiation.

6.5 References

[1] M. Seuss, W. Schmolke, A. Drechsler, A. Fery, S. Seiffert, *ACS applied materials & interfaces* **2016**, *8*, 16317.

[2] K.-P. Kronfeld, H.-J. Timpe, *J. Prakt. Chem.* **1988**, *330*, 571.

7. Project II.3: Core-Shell synthesis

7.1 Introduction into the topic

In this final part of "*Project II Core-shell interfacial interpenetration control for switchable elasticity*" the focus is on the creation of the actual core-shell particles. As core-particles the microgels synthesized in chapter 5 are used and for the shell the precursor polymer synthesized in chapter 6. Besides the synthesis of the core-shell particles a secondary focus is on the control of the interpenetration depths of the shell for the desired control of the switchable elasticity (see chapter 4, figure 4.1).

To better understand the challenges faced with the creation of the core-shell particles using a double emulsion microfluidic setup, preliminary experiments using the abundant core-particles from the synthesis with the 200 µm devices were performed and the microfluidic setup adjusted to allow control over the interpenetration depths.

Furthermore, to better comprehend the diffusion of linear polymer chains into a polymer network, simulations were analyzed during a tandem project with the theoretical partner [redacted] [redacted].

7.2 Preliminary experiments to create core-shell microparticles using microfluidics

As microfluidic device for the preliminary experiments a PDMS-device depicted in **figure 7.1** was used. The double emulsion setup has channel widths of 1000 µm at the second cross-section with a slightly smaller first cross-section (~ 700 µm).

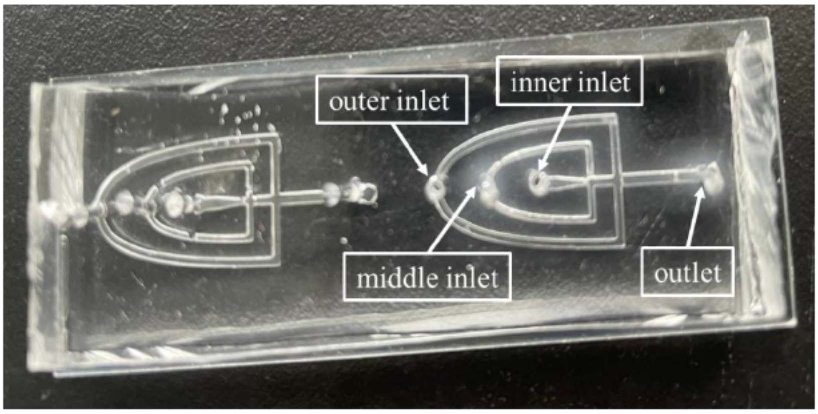

Figure 7.1: PDMS-device used in the preliminary core-shell experiments. The device has three inlets (to the left of the cross-sections) and one outlet to the right of the cross-sections.

Into the three inlets the following three phases as summarized in **table 7.1** were injected using syringe pumps *PHD ULTRA* from *Harvard Apparatus*.

Table 7.1: Composition of the three phases used during the core-shell microfluidic preliminary experiments.

inlet	phase	phase composition
outer inlet	continuous phase	Low viscous paraffin oil with 10 wt% ABIL EM 90
middle inlet	shell-polymer phase	Aqueous solution containing: • 100 $\frac{\mathrm{g}}{\mathrm{L}}$ of the shell-precursor polymer • 1 $\frac{\mathrm{g}}{\mathrm{L}}$ of the photosensitizer TXS
inner inlet	core-particle phase	Aqueous dispersion containing: • core-particles

7.2.1 Challenges during the preliminary experiments

One key aspect of microfluidic experiments is the stable flow of the individual phases for consistent droplet creation. During the preliminary experiments the stable flow of the core-dispersion proved to be challenging. The dispersion had been prepared by removing as much excess water via decantation with pipetttes and using paper wipes to further remove excess water. These core-dispersions however needed extreme pressures or flowrates $\left(> 3\,\frac{\mathrm{mL}}{\mathrm{h}}\right)$ to beginn the core-flow. As the core-dispersion moved twoards the microfluidic device it further seperated into core- and water-rich segments. This segmentation of the dispersion lead to instability in the core-flow within the device switching from rapid core-flow slowly to no core-flow. In the case of rapid core-flow the first cross-section of the microfluidic device was often flooded with core-particles as depicted in **figure 7.2**.

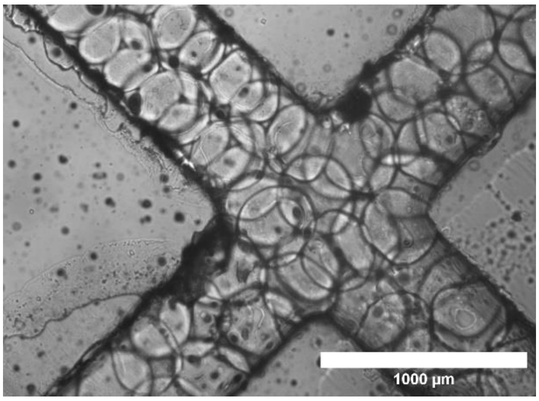

Figure 7.2: Core-particles having flooded the first cross-section of the PDMS microfluidic device, with the intended flow of the core-particles from the top left to the bottom right.

The flooding of the first cross-section, at which the core-particle is to be engulfed by the shell-phase would be detrimental in the case of the synthesis of the core-shell particles with controlled interpenetration depths. As the rapid core-flow slowly decreased core-shell particles formed from both fresh cores as well as cores, which had flooded the cross-section. This would remove the control of the interpenetration depths of the shell, which is one central aim of this project.

As the core-flow decreased the creation of core-shell particles as depicted in **figure 7.3** did succeed. With the channel size of the microfluidic device fitting multiple cores side by side (see figure 7.2) the core-shell particles mostly though contained multiple cores instead of a single one.

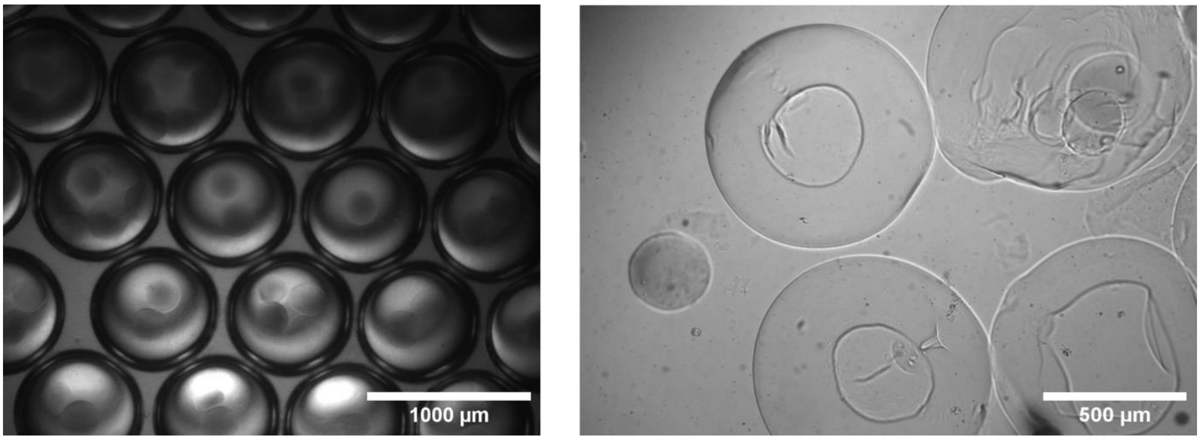

Figure 7.3: Core-shell particles synthesized during the preliminary experiments. On the left still within the continuous phase and on the right after the removal of the continuous phase and transfer of the core-shell particles into distilled water.

On the left of figure 7.3 the core-shell particles are shown still within the continous phase. As intended the core-shell particles contain core-particles, however unlike planned in most cases there are multiple cores in one core-shell particle. Futhermore the core-particles seem to have shrunken in size, which became problematic once the core-shell particles were transferred into Milli-Q water, as the cores seem to have burst from the core-shell particles.

The peliminary tests identified two challenges leading to these results. One beeing the PDMS-devices channel sizes, which were to big resulting in multiple cores being pushed into the cross-section at the same time and secondly the instability of the flow-rate of the core-particle dispersion which lead to inconsistent core-feeding into the cross-section also resulting in core-shell particles with multiple to no cores.

7.2.2 Solutions regarding the found challenges

To overcome the core-flow instabilities the water content of the core-paste was decreased. This was done by slowly centrifugating the core-particle suspension within the syringe at 1000 rpm using a syringe stopper to keep the cores from spilling. The condensed core-paste as shown in **figure 7.4** no longer caused segmentation during the core-shell preliminary experiments.

Further the necessary pressures to achieve core-flow could be reduced by cooling the core-paste syringe using ice.

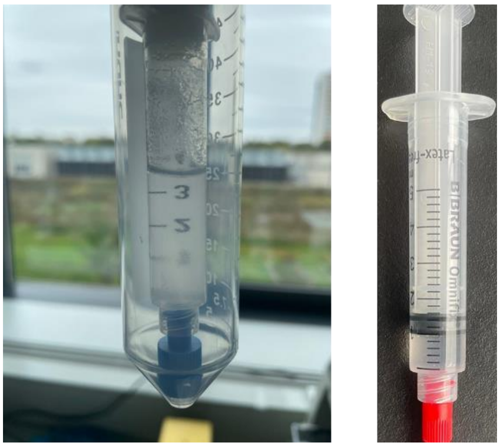

Figure 7.4: Syringe stopper in bule on the left allowing centrifugation of the core-particle dispersion within the syringe. After centrifugation the excess water is removed and the syringe piston carefully inserted resulting in the core-particle paste ready for use in core-shell microfluidics as shown on the right.

The challenge regarding the too large channel-size of the PDMS-devices used during the preliminary experiments resulted from the microfluidic master, used to create the PDMS-devices. As to create such masters the corresponding photomask has to be used (see figure 1.6), new photomasks were designed with channel-sizes matching the average diameter of the final core-particles from chapter 5 ($d \sim 120$ µm).

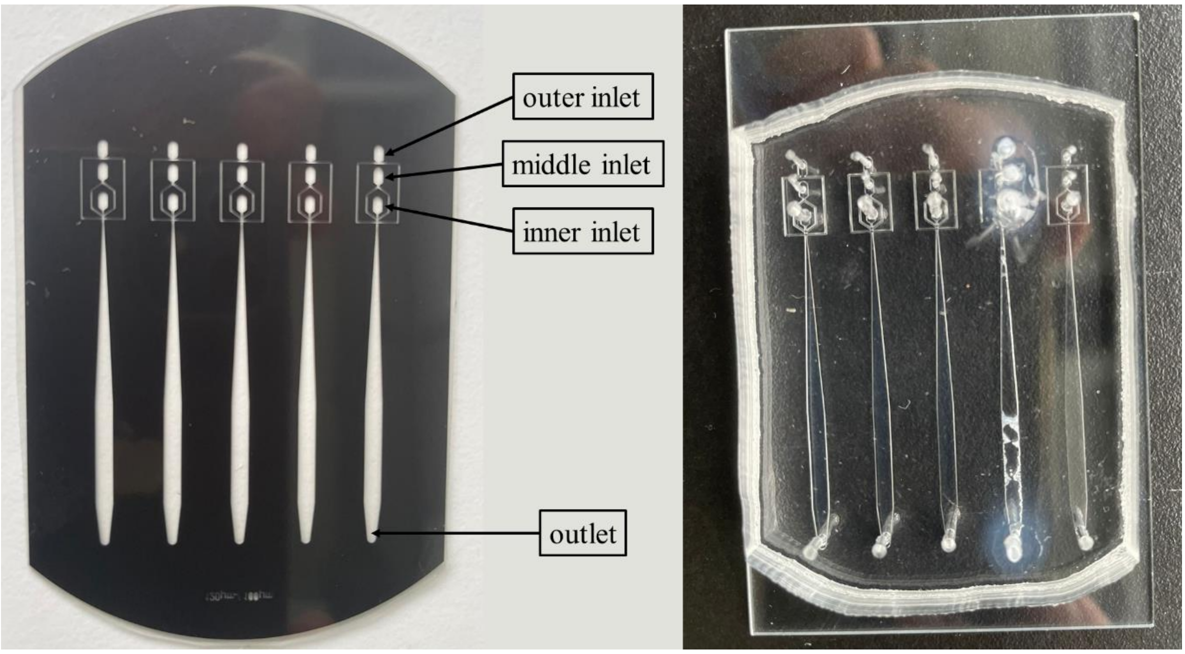

Figure 7.5: On the left designed photomask with a channel width matching the core sizes at the first cross-section and on the right the corresponding PDMS-device ready for the core-shell microfluidic experiments.

As the creation of new photomasks is both time consuming and costly a further method to adjust the channel sizes was also tested to accommodate for the slight variation of the core-particle sizes from batch to batch. Using for example *Sigmacote*® from *Merck* it is possible to slightly swell the PDMS-devices due to its organic solvent heptane. This usually unwanted effect in PDMS-devices was successfully tested on the larger PDMS-devices as depicted in figure 7.1, leading to a narrowing of the core-feeding channel by over 10 % as shown in **figure 7.6**.

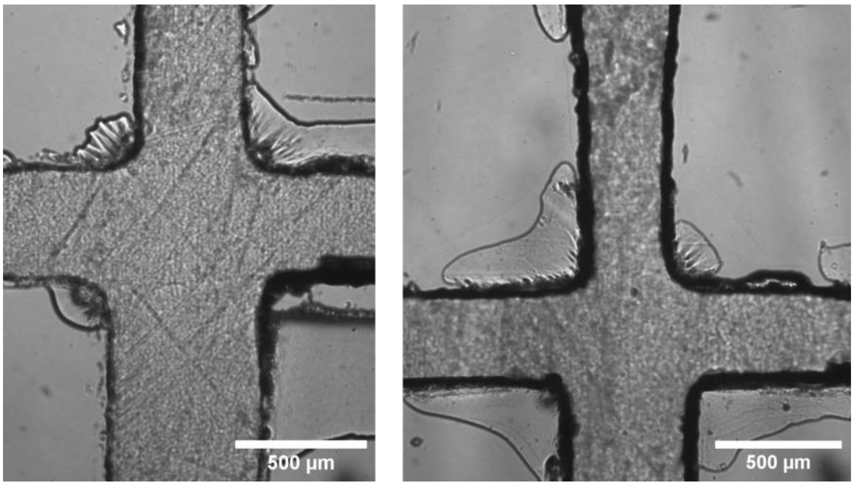

Figure 7.6: PDMS-device before swelling with Sigmacote® on the left. Same PDMS-device after leaving the Sigmacote® solution in the device for 4 minutes. The channel diameters are visibly shrunken as the PDMS has swollen.

Using the newly created photomasks in combination with the swelling effect makes it possible to create PDMS-devices with optimized channel-sizes for core-particles with a range of sizes, thereby saving the effort of having to create new optimized photomasks for every corresponding core-particle batch.

7.3 Controlling the interpenetration depths of the shell into the core

The overall aim of project II was not only the core-shell particle synthesis itself but also to control the interpenetration depths of the shell into the core, due to it determining the connectivity of the two and with it the change in the elasticity as described in figure 4.1. As the interpenetration depth is dependent on the diffusion-time of the shell-precursor polymer prior to its crosslinking via UV-radiation, the microfluidic setup has to be adapted accordingly.

In the case of well interconnected core-shell particles the diffusion time is sufficiently long to first collect the core-shell droplets and then irradiate them within the collection vial, which had also been done during the preliminary tests.

However, to synthesize core-shell particles with negligible interconnection, UV-irradiation of the droplets has to be initiated as soon as possible. In an ideal case the exposure would take place directly after the formation of the core-shell droplet. This however is not possible as the droplet formation would be hindered if the shell crosslinking reaction already started prior to the droplet formation. Instead, the UV-irradiation was located at the widest part of the exiting channel (wide downward channel in figure 7.5). Since the PDMS-device during the microfluidic experiment is placed under a microscope for droplet creation control, irradiating the droplets with high intensity UV-light poses a safety issue that had to be resolved. As a solution an irradiation-chamber with UV impermeable glass was constructed in cooperation with [redacted] as shown in **figure 7.7**.

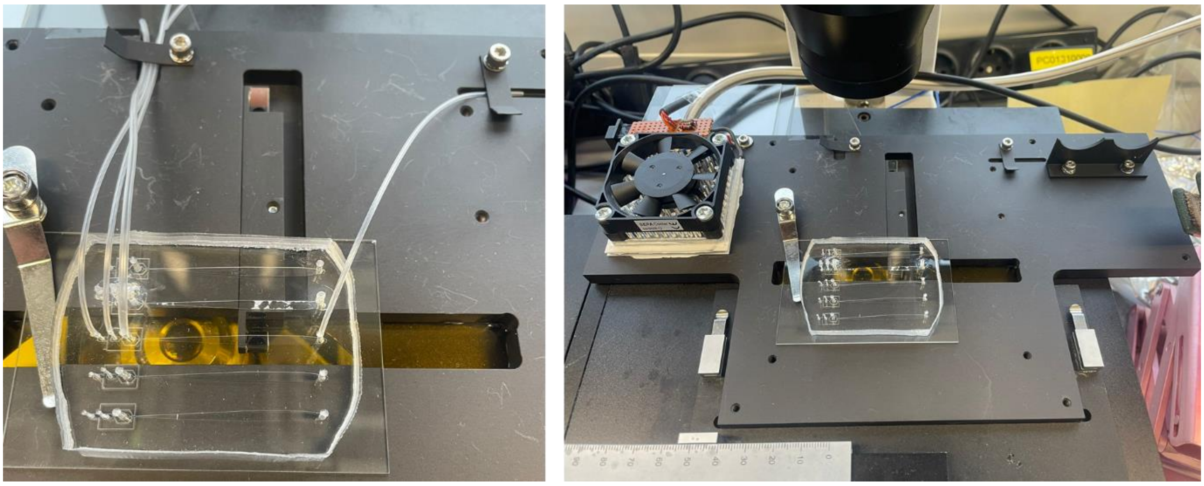

Figure 7.7: Opened irradiation chamber with PDMS-device clamped down. The connecting polyethylene tubing enter via entrance channels on the top and the exit tubing leaves to the right as can be seen on the left. For temperature control a small piezo element is connected to the chamber on the left and on the right two collection vials can be placed as shown on the right.

The irradiation chamber is designed to allow the UV exposure of the core-shell droplets through the glass from underneath using two mirrors aligned with the glass fiber connector of the *OmniCure series 1500* UV lamp. The irradiation channel is located in the center of the irradiation chamber (see figure 7.8). A depiction of the closed irradiation chamber can be seen in **figure 7.8**. As once the irradiation chamber is closed it can no longer be opened during the experiment it is paramount to carefully place of the device using the metal clamps to ensure the successful irradiation of the droplets and therefore obtain the wanted core-shell particles with negligible interconnections of the two.

Figure 7.8: Closed irradiation chamber underneath the microscope allowing the creation of core-shell particles with negligible connection between the two.

7.4 Diffusion simulations of linear polymer chains into a defective polymer gel

In prior research the diffusion of linear polymers (102 beads in length) into diamond lattice gel with equal strand lengths had already been analyzed.[1] Since diamond lattice polymer networks represent ideal networks and do not truly describe the polymer networks of the core-particles of this project new diffusion simulations of linear polymer strands (80 beads in length) into defective polymer gels were to be analyzed. This was done in a tandem project with the workload split according to **table 7.2**.

Table 7.2: Task distribution during the tandem project "Diffusion simulations of linear polymer chains into a defective polymer gel".

[redacted]	• programming: ➢ free radical polymerization simulation of the polymer network ➢ diffusion simulation script of the linear polymer strands into the polymer network • programming expertise • evaluation of analysis results
Torsten Gereon Linder	• programming: ➢ python scripts for analysis of diffusion simulation • chemical expertise • evaluation of analysis results

To help better understand the following analysis of the diffusion simulations a brief description of the simulations themselves is provided.

7.4.1 Simulating the diffusion of a linear polymer into a polymer network

In preparation of the diffusion simulations the polymer gel was first created in a separate simulation. In this simulation a free radical polymerization using a monomer, represented by single beads, as well as, crosslinkers, represented by four connected beads in the shape of a tetrahedron, was mimicked. Once the creation of the polymer network was finished in the simulation any non-reacted monomer- and crosslinker-beads were deleted and the polymer network was given time to equilibrate. During the diffusion simulations the simulation box, in which the polymer network had been created, was expanded to both sides to a length of 135 length units. The empty space to both sides was then filled with polymer bead strands, until the desired “concentration” of these linear polymers was reached. After this the simulated linear polymers were equilibrated with a repulsive barrier between the polymer network and the linear polymers preventing any diffusion into the gel at this point.

With all this done to start the diffusion simulation the barrier was removed and $16 \cdot 10^7$ simulation steps taken. During each one of these simulated time steps every bead within the simulation could move a certain distance following Newtons laws of motion. In **figure 7.9** the simulated polymer gel as well as the linear polymers can be seen within the simulation box with τ in this case denoting the time steps of the simulation that have already occurred. τ can be calculated using the following equation, with dt denoting the time laps, according to $\tau = simulation\ step\ \cdot dt$, in this case $dt = 0.001$.

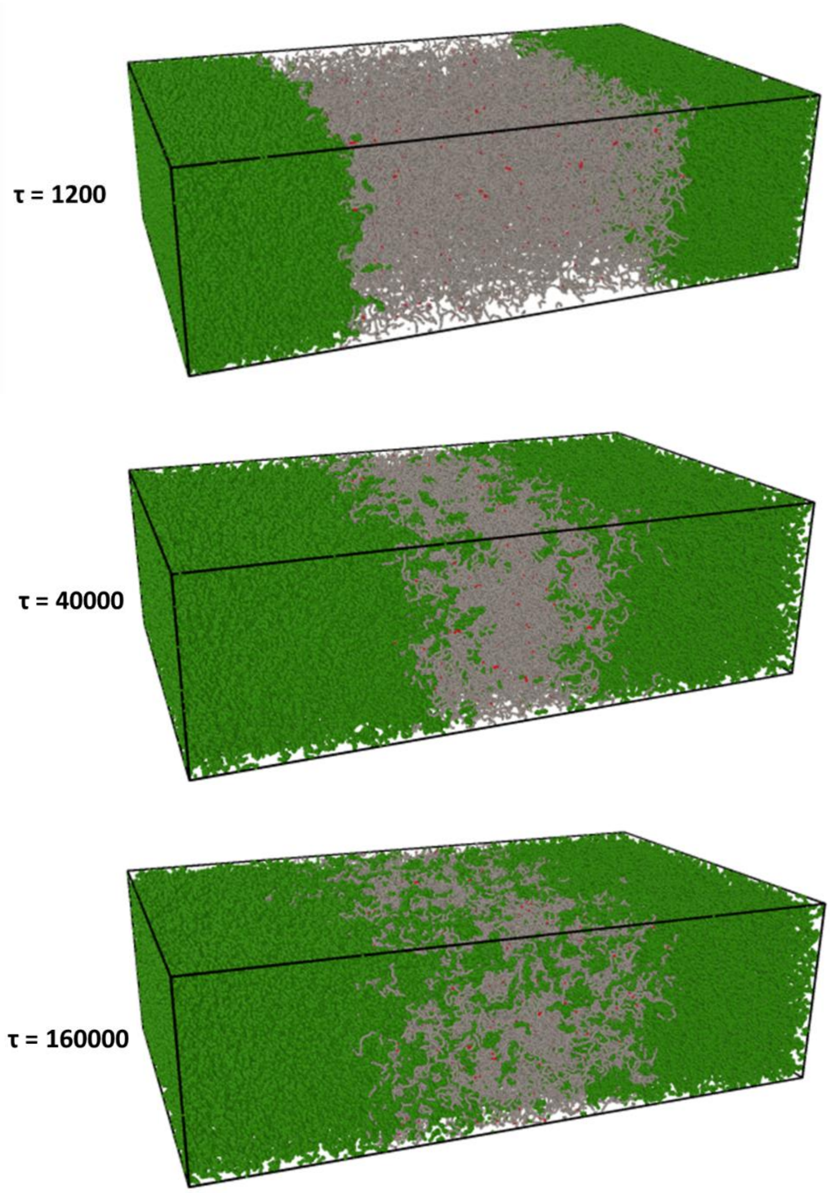

Figure 7.9: Simulation box after 1200, 40000 and 160000 τ, showing the diffusion of the linear polymer strands (green) into the polymer gel (monomer units in grey, crosslinker units in red)

For future analysis the position and properties of each bead, as to whether it was part of the polymer network or part of the diffusing linear polymers within the simulation box, was recorded with every $2 \cdot 10^5$ simulation steps.

7.4.2 Analysis of the diffusion simulations

The diffusion simulations were analyzed using self-written python scrips. After a short crash course in programming with python, several different scripts were written (a selection can be found in the **appendix A2**) among which, there were scripts to analyze the density profiles of the linear polymer strands and the polymer gel-network within the simulation box (see **figure 7.10**); the degree of interfacial integration (DII) versus the simulation steps that had occurred, i.e. how many linear polymers were diffusing into the gel-network at the time; the radius of gyration squared of the polymer stands and the overall orientation of the polymer stands within the simulation box among a few to be named. The results of the analysis were then saved in “.txt”, as well as, “.npy” files, from which the results could then be plotted.

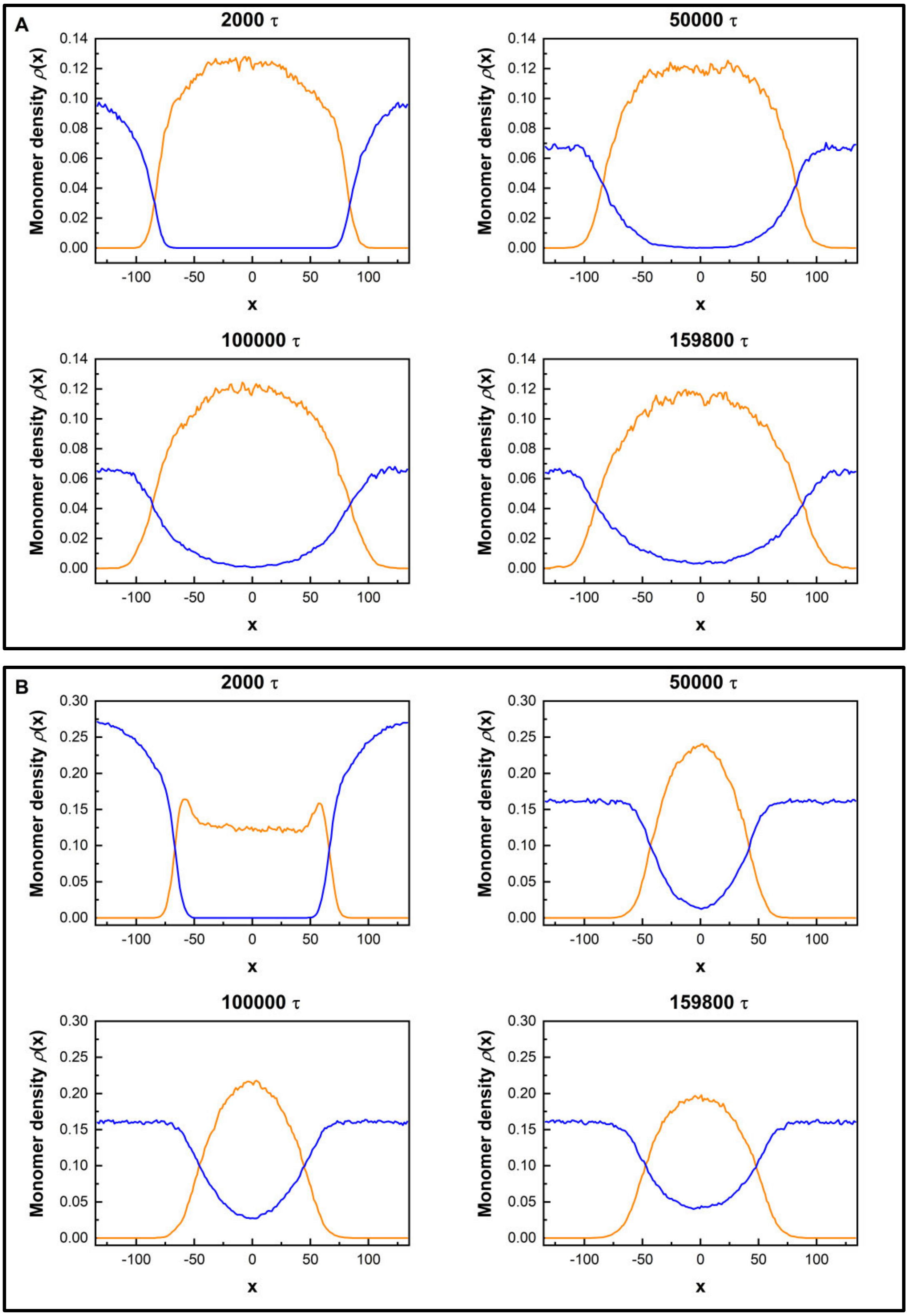

*Figure 7.10: Density profile of the simulation boxes of both the polymer network (orange) and the diffusing linear polymer strands (blue) at different times in the simulations. The volume fraction of the diffusing linear polymer is in **(A)** 0.09 and in **(B)** 0.39.*

In general figure 7.10 depicts the slow diffusion of the linear polymer strands into the polymer network. It can further be noted that the volume fraction of the linear polymer strands has a significant impact on the diffusion speed, as well as, on the penetration depths. If the concentration of the chains is low (figure **7.10A**, volume fraction = 0.09) the linear polymer strands even at the end of the simulation have not reached a significant density at the center of the polymer gel. Furthermore, the density profile of the linear polymers after 50000 τ no longer significantly changes. In contrast at higher concentrations (volume fraction = 0.39), as shown in figure **7.10B**, the polymer gel at first is condensed by the surrounding linear polymers. As the simulation progresses the gel partially relaxes, as the shell polymer completely diffuses throughout the gel, having a noticeable density in the center of the polymer gel at the end of the simulation. In total the density profiles of the analysis showed similarities to the density profiles, that had been retrieved from the diffusion simulations using ideal polymer networks.[1] Due to this similarity, it was decided to next check the chain orientation of the polymer strands, as during the analysis of the diamond lattice polymer network the overall chain orientation of the free polymer chains at the interface had shown a small preference to orientate perpendicular to the interface. The overall orientation, perpendicular $R^2_{g,\perp}$ or parallel $R^2_{g,||}$, of the linear polymer strands to the interface, was calculated as components of the radius of gyration R_g^2 using the following two equations.

$$R^2_{g,\perp} = \frac{3\langle R^2_{g,x}\rangle - \langle R^2_g\rangle}{2\langle R^2_g\rangle} \tag{7.1}$$

$$R^2_{g,||} = \frac{3\left(\langle R^2_{g,z}\rangle + \langle R^2_{g,y}\rangle\right)/2 - \langle R_g\rangle^2}{2\langle R^2_g\rangle} \tag{7.2}$$

The results for the simulated free radical polymer network at the volume fractions of 0.09 and 0.39 are depicted in **figure 7.11**.

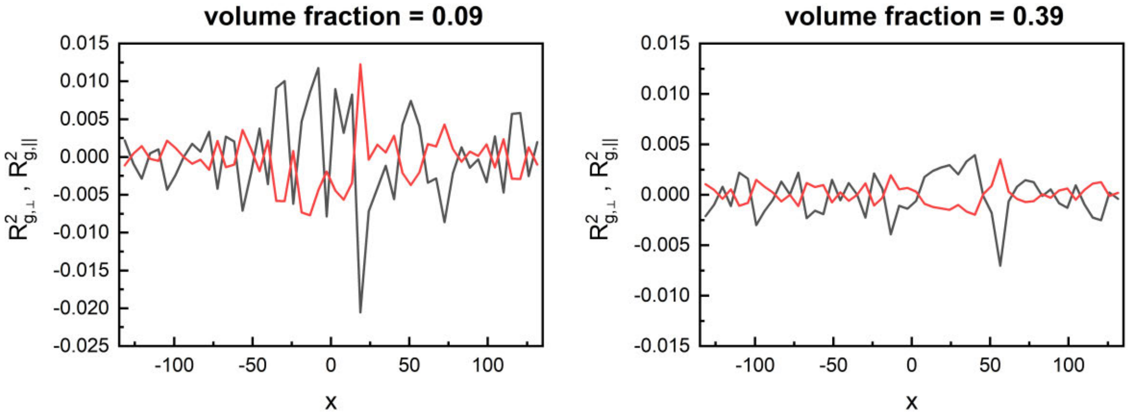

Figure 7.11: Overall chain orientation profile of the polymer strands throughout the simulation box, with $R^2_{g,\perp}$ in black and $R^2_{g,||}$ depicted in red averaged over the last 20000 τ.

As the plots in figure 7.11 show, there is no clear preference visible at any point of the chain orientation of the free polymer chains. This is very different in comparison to the previous results gained from the diamond lattice polymer networks simulations in which a preference for $R_{g,\perp}^2$ at the interface had been visible.[1] Furthermore, it had been expected to at least see some mirroring of the overall chain orientation at both sides of the polymer gel. This though is not noticeable.

To better understand what was happening at the interfaces, the diffusion distance M_a of the linear polymer chains within one simulation time step τ was analyzed next. The results can be seen in **figure 7.12**.

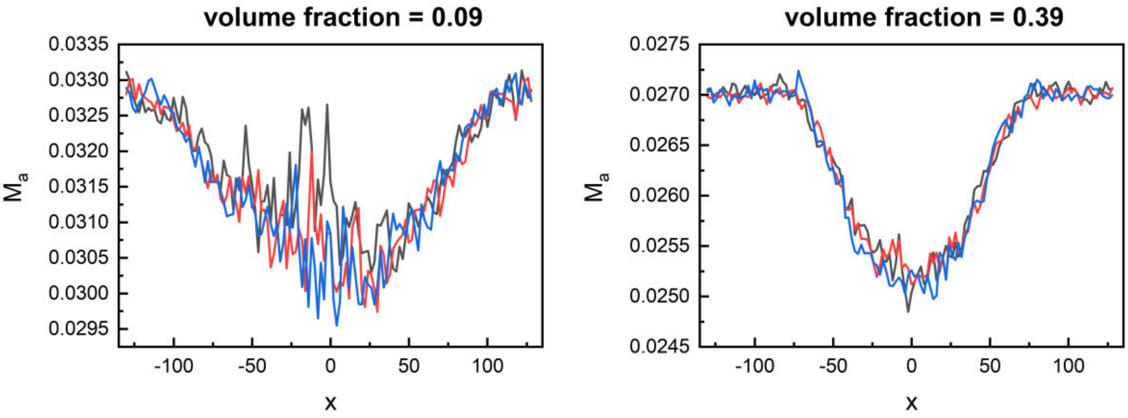

Figure 7.12: Diffusion distance M_a of the polymer strands in the simulation box, with $a = x$ in black, $a = y$ in red and $a = z$ in blue.

The diffusion distances, depicted in figure 7.12 above, show all a clear trend. Once the polymers enter the polymer gel the diffusion distance decreases due to the obstructions of the polymer network. Furthermore, at higher volume fractions the overall diffusion distance is decreased as the density within the simulation box increases. Even though in summary the results proved to be as expected, the pronounced decrease in the diffusion distance at the interfaces seen in the case of the ideal polymer networks again were not noticeable.[1] Instead, the diffusion distance decreases gradually as the gel is interpenetrated. This oddity led to further analysis of the polymer gel-network to better understand the obtained results.

Closer analysis of the polymer network revealed, that the crosslinking density was extremely heterogenous leading to large cavities within the polymer network through which rapid diffusion was possible. Furthermore, the lengths between crosslinks in the gel varied extremely, as can be seen in **figure 7.13**.

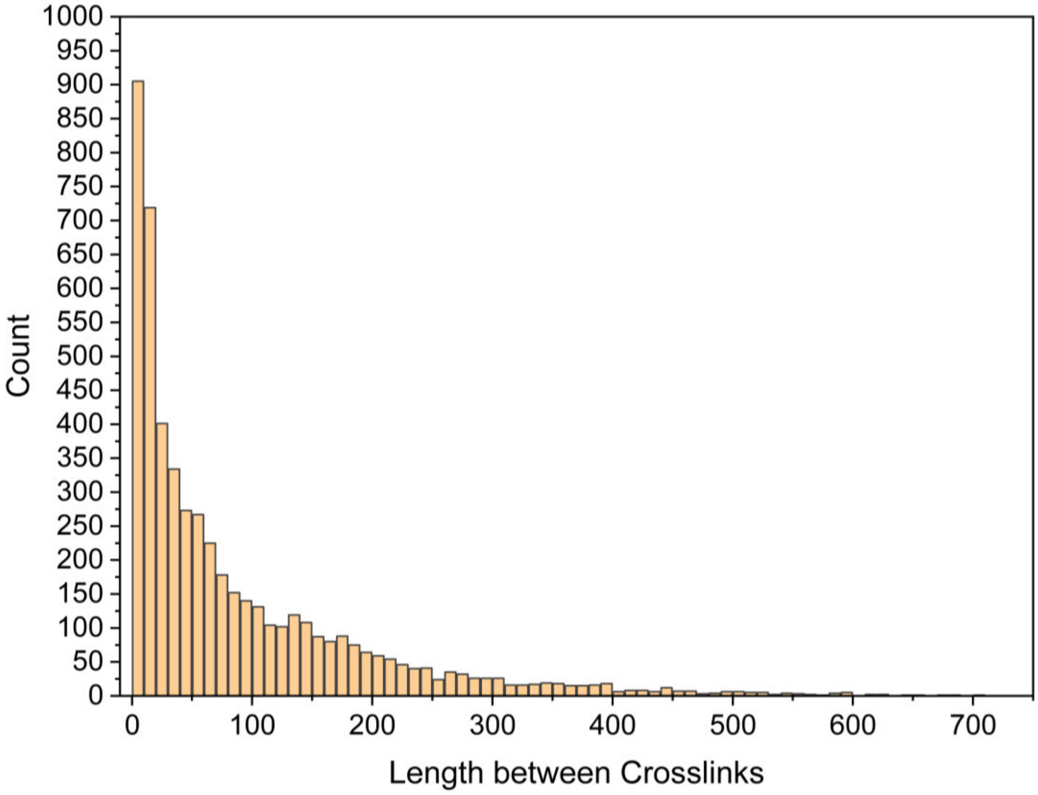

Figure 7.13: Chain lengths in number of monomers between two crosslinks in the simulated gels. The number of monomers hereby ranges from one to over 600. The majority however are in the range of $1\text{–}10$.

Though in general the chain lengths between crosslinks were intended to vary, as this would more resemble polymer networks made by free radical polymerizations, figure 7.13 shows that most of the polymer chains between crosslinks are in the range of $1\text{–}10$ monomers. This high degree of inhomogeneity however was not intended and as it did not represent the core-particle polymer networks. It was concluded that the polymer network creation simulation had therefore to be revised.

7.5 Conclusion of the project

After the successful synthesis of both the core-particles and the shell-precursor polymer in chapters 5 and 6 preliminary test were made to identify and solve the challenges of creating the core-shell particles. There were two main challenges met; the core-flow throughout the experiment and the devices channel size having to be adjusted to the core-particle size. To overcome the core-flow challenge the core-paste had excess water removed via slow centrifugation and cooling of the core-paste during the experiment. The channel-size was adjusted by using new photomasks with additional smaller scaled adjustments possible by controllably swelling the PDMS-devices.

As the overall aim of the project was to create core-shell particles with switchable elasticity possible through varied interconnectivity of the two, the microfluidic setup was improved to allow for control of the diffusion time of the shell-precursor polymer.

Sadly, due to time restraints the synthesis of core-shell particles with switchable elasticity could not be achieved, however in summary a good groundwork could be set to fulfill this goal in future research.

Lastly in a tandem simulation project with [redacted], diffusion simulations of linear polymer chains into polymer networks with defects were analyzed. The results showed a dependence of the maximum diffusion depths on the volume fractions of the linear polymers. This result was similar to previous simulations using ideal polymer networks. Due to the analysis of the overall chain orientation profile of the linear polymers not showing any symmetry and the diffusion distance gradually decreasing, the polymer network was more closely investigated. This showed a large variation of the chain lengths, which to this degree had not been intended. Thus, it was concluded that the free radical polymerization simulation to create the polymer networks had to be revised.

7.6 References

[1] J. A. Vishnu, T. G. Linder, S. Seiffert, F. Schmid, *Macromolecules* **2024**, *57*, 5545.

8. Project III: Influence of the crosslinker hydrophobicity on the swelling kinetics of poly(acrylic acid) hydrogels

8.1 Introduction to the project

With project I and project II focusing on the modification of a microfluidic experimental setup and the creation of core-shell particles this project focuses on the effect of the crosslinkers hydrophobicity on the swelling kinetics of hydrogels. As monomer 50 % neutralized acrylic acid is used. The main synthesis method is droplet-based microfluidics, with the microfluidic design being a T-junction device as shown figure **1.1A**. The results of the research were first published in Macromolecular Chemistry and Physics on the 20th of June 2024.

Influence of the Crosslinker Hydrophobicity on the Swelling Kinetics of Poly(Acrylic Acid) Microgels

Torsten Gereon Linder, [redacted]

Macromol. Chem. Phys. 2024, 225, 2400138; doi: 10.1002/macp.202400138

Corresponding *Supporting Information* included in **Appendix A.3**

First published June 20, 2024 adapted with permission of Macromol. Chem. Phys. 2024, 225, 2400138

8.2 Specific Summary

As mentioned in the theoretical background (**1.2.3**) the swelling of hydrogels is influenced by numerous different factors, among which the influence of the hydrophobicity of the crosslinker used in the hydrogel has not yet been investigated systematically. To achieve this goal, 50 % neutralized poly(acrylic acid) microgels were synthesized using four differently hydrophobic crosslinkers: *N,N'*-methylenebisacrylamide, *N,N'*-ethylenebisacrylamide, *N,N'*-propylenebisacrylamide, and *N,N'*-butylenebisacrylamide. To keep all other influences on the swelling kinetics of the microgels as constant as possible, both the polymer composition as well as the synthesis was kept uniform for all microgels. To ensure a similar integration of the crosslinkers into the microgels the reactivity ratios of four *N*-alkylacrylamides: *N*-methylacrylamide, *N*-ethylacrylamide, *N*-propylacrylamide, and *N*-butylacrylamide are first determined. They show a similar integration of all comonomers into linear poly(acrylic acid)-chains at low concentrations of the comonomer in the monomer solution. Furthermore, the reactivity ratio r_2 increases with increasing hydrophobicity of the comonomers. During the swelling kinetic experiments of the microgels it was determined that the limiting effect on the swelling rate is the gel diffusion. With this effect becoming more dominant with increasing crosslinker hydrophobicity. Determination of the activation energy of the swelling of the microgels revealed that with increasing hydrophobicity from *N,N'*-methylenebisacrylamide to *N,N'*-propylenebisacrylamide the activation energy decreased but with further increasing hydrophobicity of the crosslinker in the case of *N,N'*-butylenebisacrylamide the activation energy increased surpassing even the determined activation energy of *N,N'*-methylenebisacrylamide. This narrow window of a decrease of the activation energy of the swelling of the microgel stems from the two counteracting effects from the hydrophobicity of the crosslinker within the polymer gel. A higher degree of hydrophobicity of the gel leads to a more porous structure, which facilitates swelling. Yet the hydrophobic crosslinkers also lead to the emergence of hydrophobic domains within the gel, which increase the activation energy of the swelling of the microgels. However, the narrow window of decreasing activation energy of the swelling of the microgels could be used within industrial applications especially those, in which the swelling of the polymer is crucial.

8.3 Author Contributions

Torsten Gereon Linder:	Concept development, microgel synthesis, swelling kinetics studies, evaluation of kinetics data, linear copolymer synthesis, NMR measurements, evaluation of NMR data and paper writing.
[redacted]	Microgel synthesis, swelling kinetics studies, evaluation of kinetics data.
[redacted]	Scientific supervision of Torsten Linder and manuscript correction.
[redacted]	Concept development and manuscript correction.

8.4 Acknowledgement

The Authors would like to thank the Research Training Group GRK 2516 for funding the research work.

8.5 Abstract

Superabsorbent polymer gels are widely used in commercial areas, such as in hygiene products. A key aspect in these and other applications is the gel swelling kinetics, and a key factor of influence on that is the hydrophobicity of the gel. This paper reports on the synthesis of superabsorbent polymer microgel particles with four differently hydrophobic crosslinkers: *N,N'*-methylenebisacrylamide (MBAA), *N,N'*-ethylenebisacrylamide (EBAA), *N,N'*-propylenebisacrylamide (PBAA), and *N,N'*-butylenebisacrylamide (BBAA). This work uses droplet-based microfluidics to produce uniform and well-defined microgel specimen and study the influence of the crosslinker hydrophobicity on the swelling kinetics. In particular, this work determines swelling constants and their dependencies on the temperature of the swelling medium as well as the activation energies of swelling in relation to the crosslinker hydrophobicity. This work finds two competing effects, leading to a narrow window in which the activation energy of the swelling of the microgels decreases with increasing crosslinker hydrophobicity.

8.6 Introduction

Superabsorbent polymers (SAPs) are integral parts in many areas of use, such as in the field of medicine and pharmaceutics and as in disposable hygienic products.[1–3] In these and other applications, the swelling kinetics of the SAPs is of crucial importance.[1–3] As a result, research on different influences on the swelling kinetics of diverse types of SAPs has been intense, such as the influences of the SAP size, shape, and chemical composition as well as influences from the swelling medium. Already in 1979, Tanaka and Fillmore derived a power-law relation between the swelling time and the SAP size for spherical gels; later on, Li and Tanaka further expanded their theories in 1990 to cylindrical and disk gels.[4,5] In 2009, Atta et al. compared two crosslinkers, *N,N'*-methylenebisacrylamide and melaminetriacylamide, in poly(acrylic acid) and found that the latter had faster swelling ratios.[6] Furthermore, Jovanovic et al. investigated the swelling kinetics of poly(acrylic acid) hydrogels at different pH, finding that the activation energy of swelling decreased upon increase of the pH.[7] Using sodium methacrylate, methacrylic acid, and acrylonitrile copolymers, Sunitha et al. investigated the influence of the acrylonitrile on the swelling ratio, as well as the influence of the crosslinker concentration (butylene dimethacrylate) on the swelling kinetics of the hydrogels. The authors found that with increased crosslinking density, the swelling rate did increase as well. Furthermore, with increasing acrylonitrile content, the swelling ratios first decreased and then again increased (< 8.9 mol%).[8] Also, Sharma and Madras studied the swelling of cationic

SAPs made of [2-(methacryloyloxy) ethyl] trimethylammonium chloride and different crosslinkers with different amounts of functionalities, among which were MBAA (tetrafunctional), trimethylpropane trimethacrylate (hexafuntional), and pentaerythritol tetraacrylate (octafunctional). They found that an increase of the functionality from 4 to 6 resulted in an increase of the swelling capacity, but a further increase from 6 to 8 lead to a decrease.[9]

In general, SAPs are lightly crosslinked 3D polymer networks in which acrylic acid is the most commonly used monomer. Other common monomers are *N*-isopropylacrylamide, methacrylic acid, and ethylene oxide is sometimes also used as co-monomers with acrylic acid. As crosslinker, MBAA is the most typical choice.[6,7,10–17] The selection of the monomer as well as the crosslinker comes along with several underlying influences on the swelling kinetics, such as the possible neutralization degree of the monomer or the concentration of the crosslinker, leading to different crosslinking densities, which does not only affect the swelling kinetics, but also the mechanical properties of the SAPs. As these properties are usually predetermined in applications, influences on the swelling kinetics with no major impact on the mechanical properties are of special interest. The gel hydrophilicity and hydrophobicity can be considered as one such influence. It can be varied in several ways. One way is the integration of a co-monomer into the polymer chain backbone, as found in the form of acrylamide-*co*-acrylic acid polymer gels or Pluronic ethers used by Bomberg et al., even though in this case no swelling kinetics were investigated.[16] Okala et al. did the same using acrylic acid, *N,N*-dimethylacrylamide, and tert-butylacrylamide among other monomers to vary the gel hydrophobicity. They found that an increase of the co-monomer in the gel lowered the rate of swelling, due to increasing hydrophobicity in the gels.[18] Another possibility to influence the SAPs hydrophilicity/hydrophobicity is the crosslinker, which often results in a direct comparison between two different crosslinkers, as it was done by Atta et al., who found that the crosslinker melamine triacrylamide showed faster swelling rates in poly(acrylic acid-*co*-*N*-isopropylacrylamide) gels than the crosslinker MBAA, which these researchers attributed to the increased hydrophobicity of the copolymers and the formation of a less elastic network.[6]

In most kinetic studies, SAP sample specimen are synthesized via a bulk method, for example in cylindrical molds, via free-radical polymerization.[6,7,18–20] Such SAPs commonly show pronounced nanoscopic network defects and structural inhomogeneities.[21,22] Also, the observed swelling times of such SAP specimen are often in the range of several hours, as commonly determined via a gravimetric approach known as the “tea bag method”.[6,7,18–20,23] In this method, a dry SAP is placed in an excess of swelling solution and left to swell for a determined time. Then, it is removed from the swelling solution, and after excess medium is removed from the outside of the gel, the SAP is weighted, and the weight increase noted. This process, however, is prone to inaccuracies. One such inaccuracy is the removal of excess medium after the SAP is taken from the swelling solution, which is commonly performed with a tissue and may both be done too gently or too harshly. In addition, the typically long swelling times in the tea bag method can come along with ageing of the structure of a gel, such as hydrolysis of parts of the network. Long swelling times as well as gel hydrolysis also generally render such SAPs inapplicable for most commercial products.

On top of these practical flaws, the current level of research generally lacks a systematic isolation of the influence of the crosslinker hydrophobicity on the swelling kinetics of SAPs that leaves other influences as the concentration of the crosslinker as well as the SAPs monomer constant. Furthermore, a faster approach to determine the swelling speed is needed to quantify the influence of factors such as the network hydrophobicity.

In this paper, we aim to systematically isolate the influence of the crosslinker hydrophobicity on the swelling kinetics of SAP microgels. We keep the composition of the polymer gels consistent in both the fraction of the monomer, which is 50% neutralized acrylic acid, as well as the molar concentration of both the monomer and the crosslinker. As crosslinker, four different *N,N'*-alkylbisacrylamides are employed: MBAA, *N,N'*-ethylenebisacrylamide (EBAA), *N,N'*-propylenebisacrylamide (PBAA), and *N,N'*-butylenebisacrylamide (BBAA), as displayed in **Figure 8.1**. The hydrophobicity of these crosslinkers increases as the alkylene chain lengths increase. With these components, we use droplet-based microfluidics to template uniform, sub-millimeter-sized microgel specimen.[24–27] Due to efficient transfer of the heat of polymerization from the gelling droplets to a surrounding continuous phase, hot spots inside the gelling specimen are avoided, thereby reducing large-scale structural heterogeneities in the gel samples.[24,28] As the swelling time scales with the square of the size of the microgel, [4] the swelling kinetics of these small microgels can be easily observed via optical microscopy in real-time, whereby the datapoint density is only limited by the millisecond-range camera framerate.

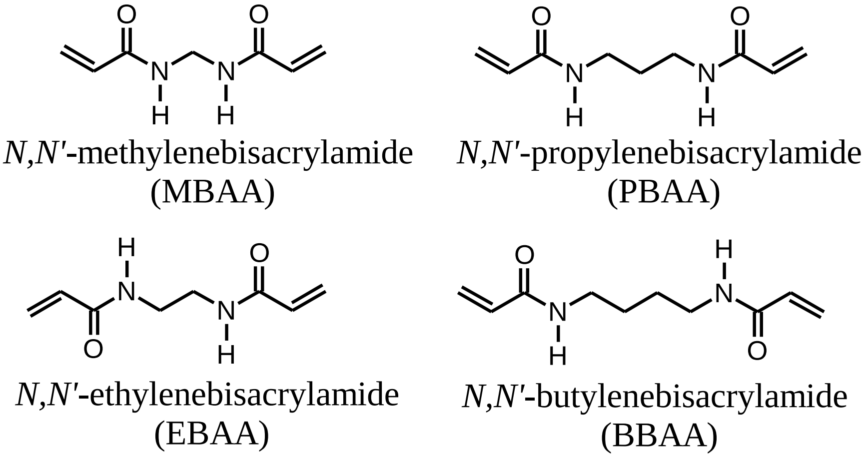

Figure 8.1: Crosslinkers used in droplet-based microfluidic experiments to create superabsorbent polymer microgels.

8.7 Experimental Part

Materials Used: Acrylic acid and *N,N,N’,N’*-tetramethyl-ethylenediamine (TEMED) were purchased from Sigma-Aldrich, ammoniumperoxodisulfate (APS) from Acros Organics, sodium hydroxide solution 50% from Merck, MBAA, EBAA, PBAA, BBAA as well as *N*-methylacrylamide, *N*-ethylacrylamide, *N*-propylacrylamide and *N*-butylacrylamide from BLDpharm. For the continuous phase in the microfluidic experiments low viscosity paraffin oil from Roth was used with ABIL EM 90 as surfactant from Evonik Industries. All chemicals were used as received.

SAP Microparticle Synthesis via Droplet-Based Microfluidics: For the droplet-based microfluidic experiments an aqueous solution (dispersed phase) of 50% neutralized acrylic acid was prepared by adding 0.56 g of a sodium hydroxide solution (50%) (7 mmol) dropwise to 1.00 g of acrylic acid (14 mmol) diluted with 3.43 mL of milli-Q water. To the solution 0.3 mol% crosslinker (versus acrylic acid) was added, and the mixture was shaken (250 rpm) over night for the crosslinker to dissolve. Once a clear solution was obtained 5 mg of APS initiator was added (dispersed phase). For the continuous phase low viscosity paraffin oil was mixed with 10 wt% of ABIL EM90 as surfactant. 2 g of TEMED were added to 5 mL of the continuous phase (as APS initiation activator), and 0.5 mL of the continuous phase solution were filled into the collection vial used during the microfluidic experiment. After about 8 mL had been collected, the collection vial was changed with a fresh vial containing fresh 0.5 mL of TEMED mixed continuous phase.

Both the dispersed phase as well as the continuous phase were filled in syringes and pumped into a self-made polydimethylsiloxane (PDMS) microfluidic chip using two PHD ULTRA syringe pumps from Harvard Apparatus. The flowrates were adjusted for optimal droplet creation with the dispersed phase having flowrates between 75 and 125 µL h^{-1} and the continuous phase 700 and 725 µL h^{-1}, and the experiment was left running for up to 24 hours. The droplets were left for a further 24 hours at room temperature to ensure complete polymerization. Afterwards, the continuous phase was removed, isopropanol was added, and the microgels were washed five times with 5 mL of isopropanol each, followed by further five times washing with acetone. Afterwards the microgels were dried using a hotplate at 90 °C for 2.5 h to conduct for the swelling kinetic studies. The dried microgels had a size between 50 and 60 µm.

Copolymer Synthesis for Determination of the Reactivity Ratios of the Co-Monomers: Acrylic acid was first diluted with 20 mL milli-Q water and then neutralized with sodium hydroxide solution. The corresponding amount of *N*-alkylacrylamides was added and the mixture was bubbled for 3 h with argon. An amount of 0.11 g of APS was dissolved in 0.5 mL of milli-Q water, and 75 µL TEMED was added to initiate the polymerization. The progress of the polymerization was checked every 10 min by trying to precipitate aliquot samples in excess oxolane. Once a noticeable precipitation was observed the reaction was terminated in oxolane, whereby the polymer precipitated. The product was isolated by filtration, re-dissolved in water, dialyzed for 1 week against deionized water, and finally gained in solid form by freeze drying. For analysis of the copolymer composition, 3 mg were dissolved in D_2O and subjected to the ^{1}H-NMR-experiments conducted on an NMR spectrometer of type Bucker AC 400 (400 MHz). The resulting spectra were evaluated using the software MestReNova V5 by MESTRELAB RESEARCH S.L..

Swelling Experiments of the SAP Microparticles: A small amount of the microgel particles was filled into a single well of a µ-Slide 8 Well ibiTreat made by Ibidi and separated until single free lying microgels could be seen under an inverted microscope (Axio Vert.A1 from Zeiss). Using a camera UI-3060CP from IDS and the program uEye Cockpit*,* a video of the microgel swelling was recorded. As swelling medium, a physiological salt solution (9 gL^{-1} of sodium chloride in deionized water with a pH of 5) was prepared and heated to the corresponding temperature using a thermostat CF31Kryo-Kompakt-Thermostat from Julabo. Once the temperature was reached, the swelling solution was left for 1 hour at the temperature being lightly shaken. After that, 1 mL of the swelling solution was then added to the microparticles as the video recording was already running, and the swelling of the spheres was captured for 5 min. The resulting video was then cut into single frames using a self-written python routine, which is available in the Supporting Information (see Appendix **A3**) and the single frames analyzed using the free software image-J. The particles area was determined, and from the area the corresponding diameter of the particles was calculated at various times during the swelling.

8.8 Results and Discussion

8.8.1 Reactivity ratios within co-polymerization

The material basis of our work are SAP microgels of partially neutralized acrylic acid and four differently hydrophobic crosslinkers, templated by droplet-based microfluidics. The goal of our investigation is to independently assess the crosslinker hydrophobicity on the microgel swelling kinetics. This ambition requires that all four crosslinkers are chemically incorporated into the microgels with similar extent and spatial distribution. Both can be assumed to be given if their reactivity ratios are similar in the microgel co-polymerization. However, as the crosslinkers carry two reactive groups and will lead to a crosslinked product, it is difficult to determine their extent and pattern of incorporation in the final microgel by common polymer-analytical methods. To circumvent this challenge, we take a detour and determine the reactivity ratios of monofunctional analogs to the crosslinkers, as depicted in **Figure 8.2**. We copolymerize these with the main monomer (50% neutralized acrylic acid) at different compositions and interrupt the reaction at low conversion. Isolation and analysis of the resulting linear co-polymers allows us to determine the reactivity ratios and to check whether they are similar.

N-methylacrylamide (MBAA*)

N-propylacrylamide (PBAA*)

N-ethylacrylamide (EBAA*)

N-butylacrylamide (BBAA*)

Figure 8.2: Monofunctional N-alkylacrylamides used in the determination of the reactivity ratios upon co-polymerization with acrylic acid (sodium acrylate).

If the crosslinker in a co-polymerization has a higher reactivity ratio with itself than with the co-monomer, it is prone to assemble in local domains within the microgels. To check for this, we determine the reactivity ratios of the co-polymerization of 50% neutralized acrylic acid with *N*-methylacrylamide (MBAA*), *N*-ethylacrylamide (EBAA*), *N*-propylacrylamide (PBAA*), and *N*-butylacrylamide (BBAA*) from copolymers made from reaction batches with ratios of 20, 40, 60, and 80 mol% of the corresponding *N*-alkylacrylamide. We analyze the mole fraction of the *N*-alkylacrylamide in the copolymer, F_2, via ^{1}H-NMR-spectroscopy. For this purpose, the NMR-peak of the terminal methyl group of the co-monomer is put in relation to the polymer-backbone, as depicted in **Figure 8.3** on the left. The mole fraction of the co-monomer within the polymer is then put in relation with the mole fraction of the co-monomer within the monomer solution, f_2. The reactivity ratios of the copolymerization r_1 and r_2 are then determined through linearization of the data in accordance with the method of Kélen and Tüdös,[29] as shown on the right of Figure 8.3 and listed in **Table 8.1**.

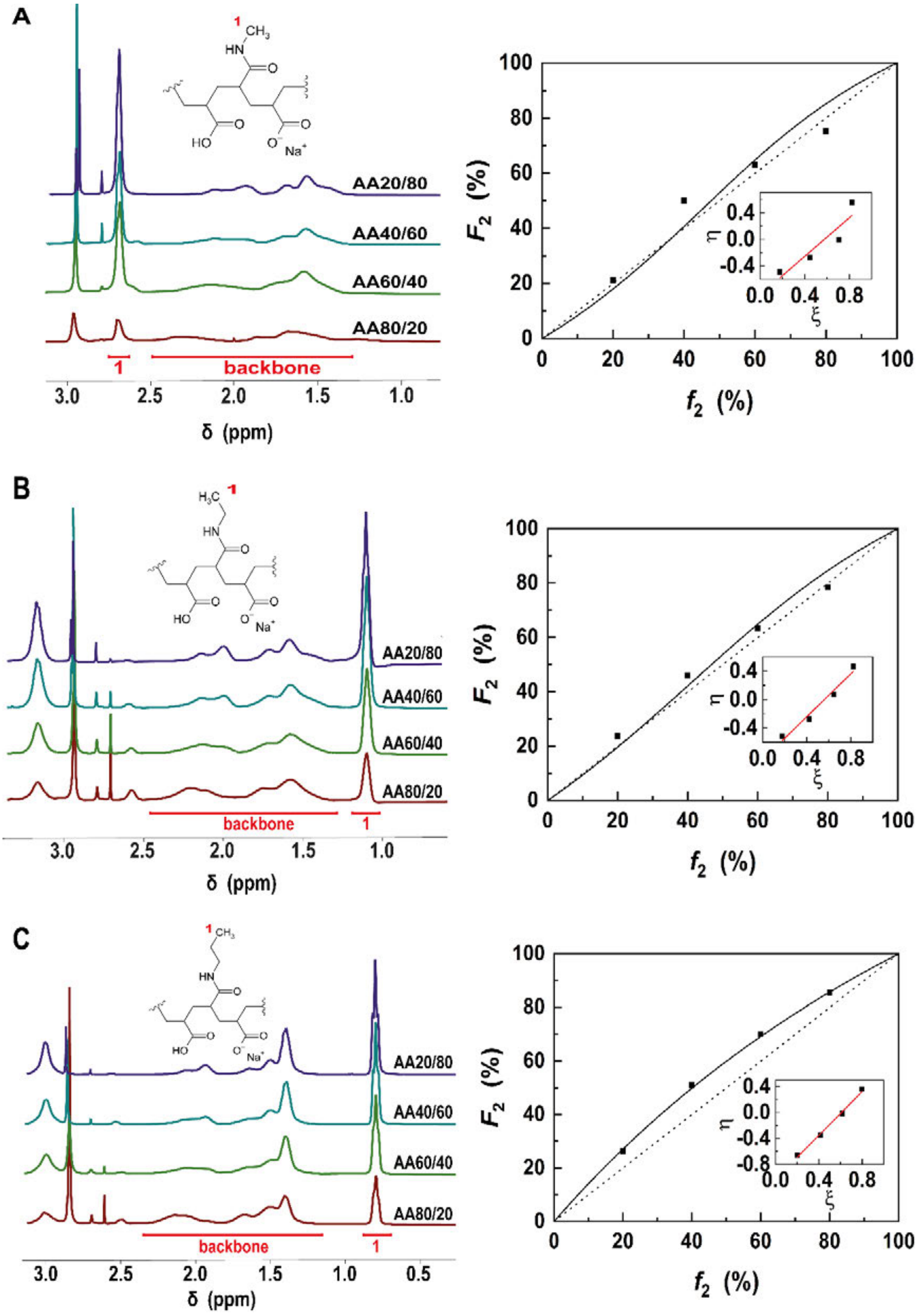

Figure 8.3: Left: NMR-spectra of copolymers of 50% neutralized acrylic acid with N-methylacrylamide (A), N-ethylacrylamide (B), and N-propylacrylamide (C). Right: Plot of the mole fraction of the corresponding N-alkylacrylamide in the polymer (F_2) vs the mole fraction in the monomer solution (f_2). The full line is calculated from the copolymerization equation using the corresponding reactivity ratios determined in this work. The inset on the right shows a linearization of the data according to the method of Kélen and Tüdös.[29]

Table 8.1: Reactivity ratios of a co-polymerization of 50% neutralized acrylic acid with N methylacrylamide (MBAA), N ethylacrylamide (EBAA*), or N propylacrylamide (PBAA*).*

Co-monomer	r_1	r_2
MBAA*	0.615	0.778
EBAA*	0.663	0.894
PBAA*	0.663	1.482

All copolymerization reactions are performed in 20 mL milli-Q water and terminated at low conversion. During the polymerization with the co-monomer *N*-butylacrylamide, the monomer solution turned opaque instantly after initiation if the concentration of the co-monomer content was at least 40 mol%. This observation impaired the determination of the reactivity ratios for this co-monomer.

We find that the reactivity ratio r_1 is similar for all, MBAA*, EBAA*, and PBAA*, whereas the reactivity ratio r_2 increases as the hydrophobicity of the *N*-alkylacrylamide increases. Thus, the statistical distribution of the co-monomers in the polymer decreases as well. Nevertheless, based on extrapolation of the data, their incorporation into the copolymers is expected to be similar for all the three in the lower range of composition (< 5 mol%). Hence, we conclude that the analog bifunctional crosslinkers are incorporated and distributed similarly in all our microgel samples at low mol-percentages.

8.8.2 Swelling kinetic studies

We continue our investigation with crosslinked and gelled SAP microspheres created by droplet-based microfluidics. Once dried, theses microgels with diameters between 50 and 60 µm are swollen in physiological saline solution, thereby obtaining larger diameters of around 100–200 µm. The swelling process is videotaped using a UI-3060CP from IDS camera mounted to an inverted optical microscope, and the frames are extracted via a python routine from the video and then analyzed. Some frames are displayed in **Figure 8.4**.

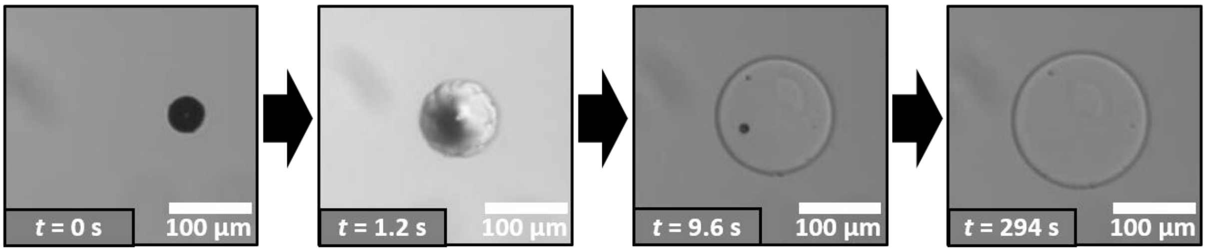

Figure 8.4: Extracted frames from the video of the swelling process of one of the microgels with length and typical timescales for reference.

The swelling degree (*SD*) of the SAPs is defined from the normalized diameter of the particles:

$$SD = \frac{d_t}{d_0} - 1 \tag{8.1}$$

In this equation, *SD* is the swelling degree, d_t is the diameter of the particles at the time *t,* and d_0 is the diameter of the particles in the dried state. Plotting the *SD* against the time that the SAP microparticles spent in excess physiological saline solution results in the corresponding swelling curve. We determine these curves on an individual particle level, as shown in **Figure 8.5**.

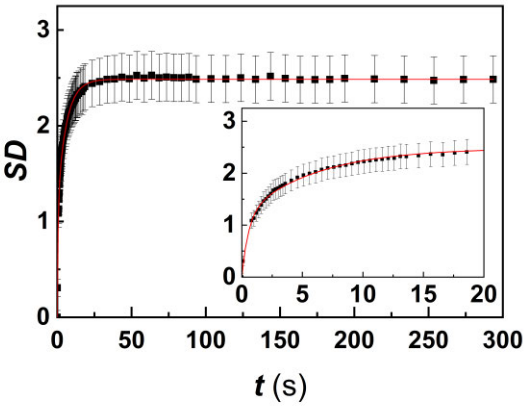

Figure 8.5: Swelling curve of a single SAP microgel containing the crosslinker MBAA in physiological saline solution at 45 °C. The error bars denote the possible error of the swelling degree calculated from the errors from the determination of the diameters of the particle at the start of the swelling and at time t. The red line is a fit to Equation 2. The inset shows a zoom onto the data between 0 and 20 seconds.

Fitting of the datapoints for the swelling of the SAP microspheres is best achieved with a bi-exponential function:

$$SD = A \cdot \left(1 - exp\left(\frac{-t}{\tau_1}\right)\right) + B \cdot \left(1 - exp\left(\frac{-t}{\tau_2}\right)\right) \tag{8.2}$$

With A and B being weighting factors of the two exponential functions, t the time that the microgel was surrounded by swelling medium, and τ_1 and τ_2 the specific swelling times. A compilation of all fitting-parameter values is available in the S.I. (Appendix **A3**) After each of the particles swelling curves are fitted, the average of the swelling curve fits of all particles containing one crosslinker and swelling at 10 °C, 25 °C, 45 °C, 65 °C, and 85 °C are taken. The averaged datapoints are again fitted to Equation 8.2, as shown in **Figure 8.6**.

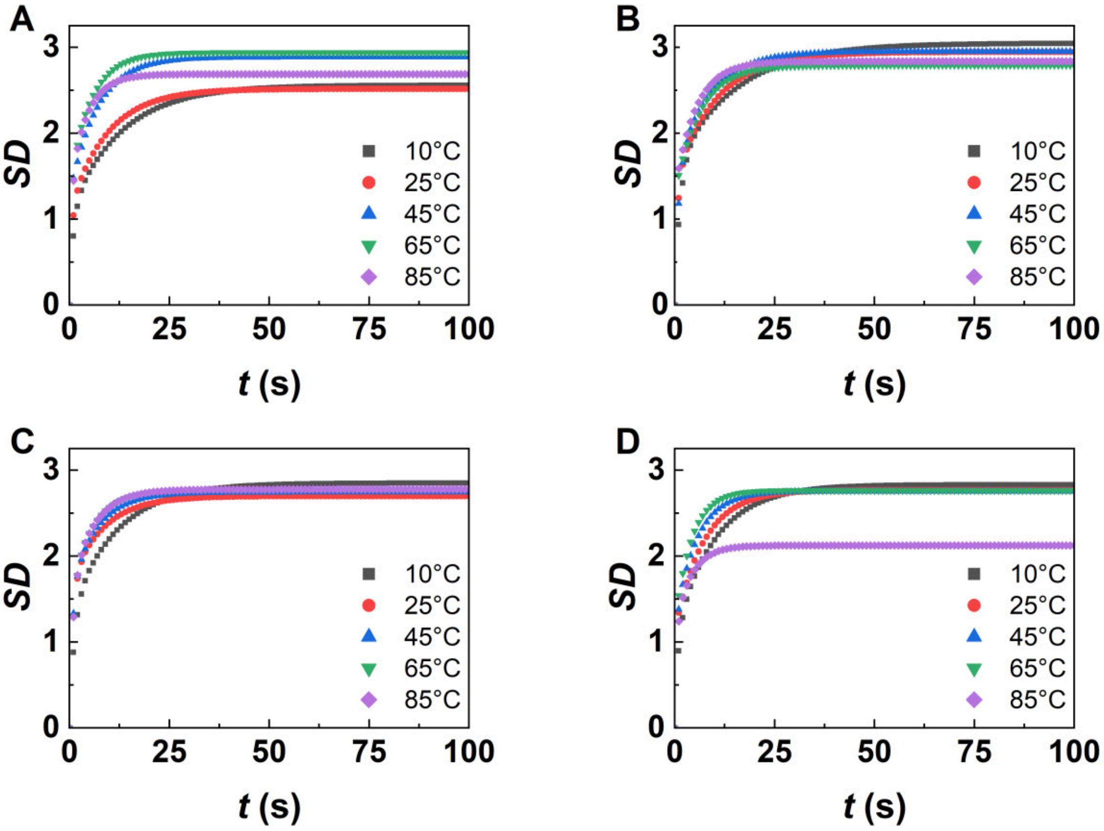

Figure 8.6: Fits of the swelling degree of the swelling data averaged over the particles of the SAP microgel particles containing the different crosslinkers MBAA (A), EBAA (B), PBAA (C) and BBAA (D) in physiological saline solution vs the time t spent in the swelling solution at temperatures of 10, 25, 45, 65 and 85 °C.

The averaged swelling curves of the SAP microparticles containing the different crosslinkers MBAA, EBAA, PBAA, and BBAA show no clear trend as the temperature of the swelling medium increases. In general, all SAP microparticles reach the swelling equilibrium within 100 s, with extremely fast changes in the *SD* within the first few seconds after the microparticle is immersed in the swelling solution.

A possible model to describe the swelling kinetics is the diffusion of the gel-network as a primary driving swelling kinetic force, as expressed by Equation 8.3: [20]

$$\ln\left(\frac{SD_{\mathrm{eq}}}{SD_{\mathrm{eq}}-SD_{\mathrm{t}}}\right) = k \cdot t \tag{8.3}$$

In this equation, k is the swelling constant of the gel, SD_{eq} the SD at equilibrium, and SD_{t} the SD at time t. **Figure 8.7** shows this function applied to the swelling kinetics of the SAP microspheres with the four different crosslinkers.

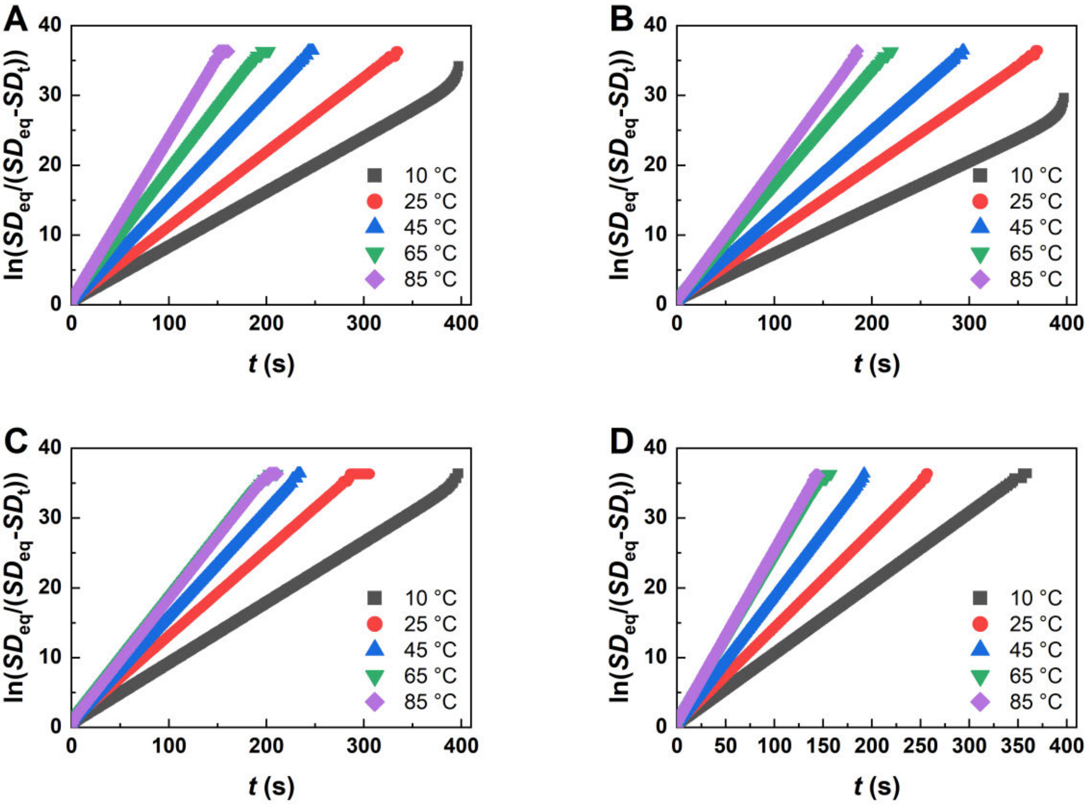

Figure 8.7: Plots of the natural logarithm of the swelling degree at equilibrium divided by the difference between the swelling degree at equilibrium and the swelling degree at time t versus the time t spent within physiological saline solution at different temperatures for the SAP microgels containing the crosslinkers MBAA (A), EBAA (B), PBAA (C), and BBAA(D).

Figure 8.7 shows a linear relationship up to at least 90% of the swelling for all SAP microspheres once the temperature of the swelling medium is at least 25 °C. Furthermore, the influence of the crosslinker hydrophobicity also leads to an increase in the linearity at 10 °C. Therefore, it can be concluded that the rate-limiting factor of the SAP microspheres' swelling kinetics is the gel diffusion. In addition, as the hydrophobicity of the gel slightly increases for the more hydrophobic crosslinkers, this influence becomes even more prominent, especially for swelling beyond 90% of the equilibrium capacity of the microgels. Regarding the plots shown for 65 °C and 85 °C, it can further be seen that the difference of the two plots becomes less as the hydrophobicity of the crosslinker increases. As each swelling kinetic curve has its own swelling constant k, specific to the type of microgel as well as the temperature of the swelling medium, we calculate all swelling constants, as listed in **Table 8.2** and plotted against the temperature of the swelling medium T in **Figure 8.8**.

Table 8.2: Calculated swelling constants k of the microparticles with the crosslinkers MBAA, EBAA, PBAA, and BBAA at the corresponding temperature of the swelling medium T.

T [°C]	$k_{\mathrm{MBAA}}\,[s^{-1}]$	$k_{\mathrm{EBAA}}\,[s^{-1}]$	$k_{\mathrm{PBAA}}\,[s^{-1}]$	$k_{\mathrm{BBAA}}\,[s^{-1}]$
10	0.079	0.067	0.087	0.101
25	0.107	0.096	0.121	0.138
45	0.146	0.121	0.152	0.184
65	0.183	0.164	0.175	0.235
85	0.231	0.191	0.175	0.247

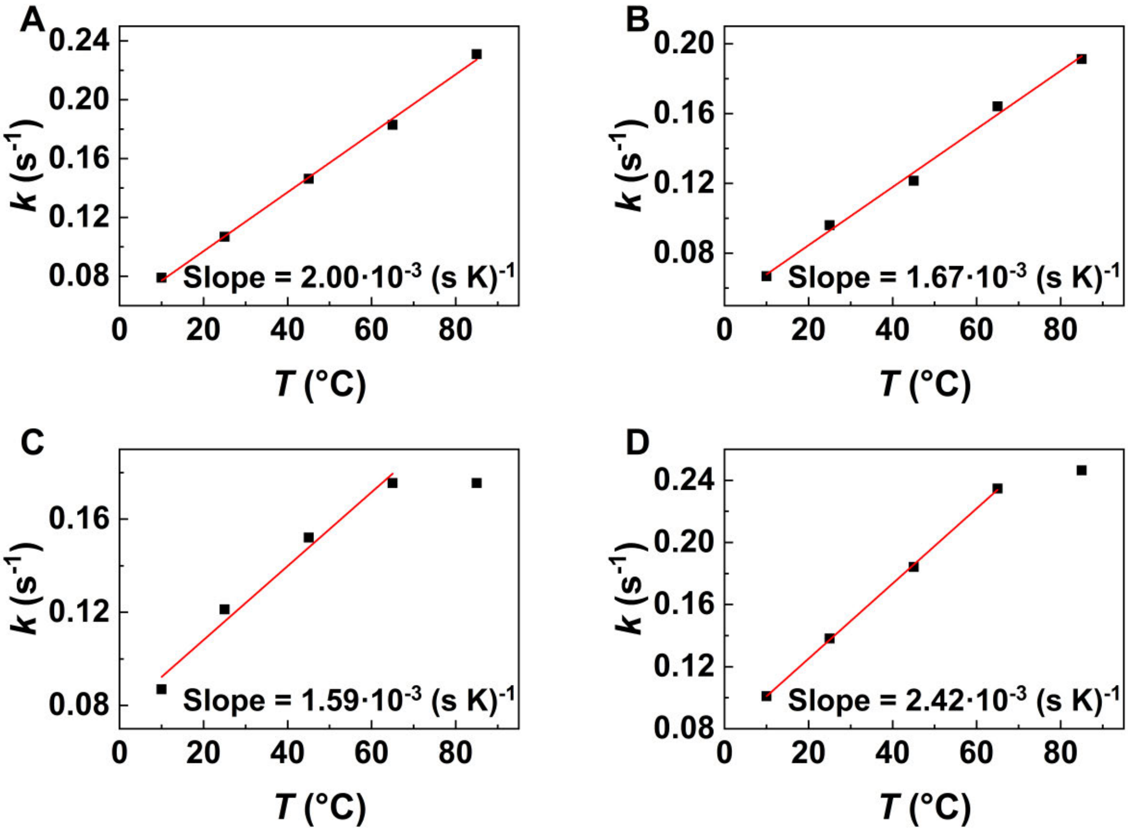

Figure 8.8: Swelling constant k of the SAP microgels containing the crosslinkers MBAA (A), EBAA (B), PBAA (C), and BBAA (D) versus temperature. The red lines are linear fits through the low temperature branch of the dataset.

Figure 8.8 shows a linear relation of the swelling kinetic constant k and the temperature of the swelling medium T, which seems to start to break down and reach a plateau between 65 °C and 85 °C at higher crosslinker hydrophobicity. This finding corresponds to the previous observation in Figure 8.7, where the plots at 65 °C and 85 °C become more identical as the hydrophobicity of the crosslinker increases.

If only the linear relation of the swelling constant versus temperature of the swelling medium is fitted, the change rate, Δk, can be determined, as listed in **Table 8.3**. We notice that with increasing hydrophobicity of the crosslinker, starting from MBAA to PBAA, the change rate decreases. As the hydrophobicity of the crosslinker further increases (BBAA), however, this trend inverses, leading to an increase of the change rate even exceeding the calculated values of the most hydrophilic crosslinker MBAA.

Table 8.3: Calculated change rates of the swelling constant with temperature of the swelling medium versus the crosslinker used in the SAP microgels.

Crosslinker	$\boldsymbol{\Delta k}$ $[(\mathbf{s\ K})^{-1}]$
MBAA	$2.00 \cdot 10^{-3}$
EBAA	$1.67 \cdot 10^{-3}$
PBAA	$1.59 \cdot 10^{-3}$
BBAA	$2.42 \cdot 10^{-3}$

Based on the calculated swelling constants k of the four different SAP microgels (Table 8.2), the activation energies E_a of the swelling process can be calculated based on an Arrhenius approach, as compiled in **Table 8.4** and **Figure 8.9**. In the case of the more hydrophobic crosslinkers PBAA and BBAA, the plateau region at higher temperature is ignored for the calculation of the activation energies.

Table 8.4: Activation energies of the microgel swelling, E_a, in relation to the corresponding crosslinker.

Crosslinker	$\boldsymbol{E_a}$ $[\mathbf{kJ \cdot mol^{-1}}]$
MBAA	11.9
EBAA	11.7
PBAA	10.0
BBAA	12.2

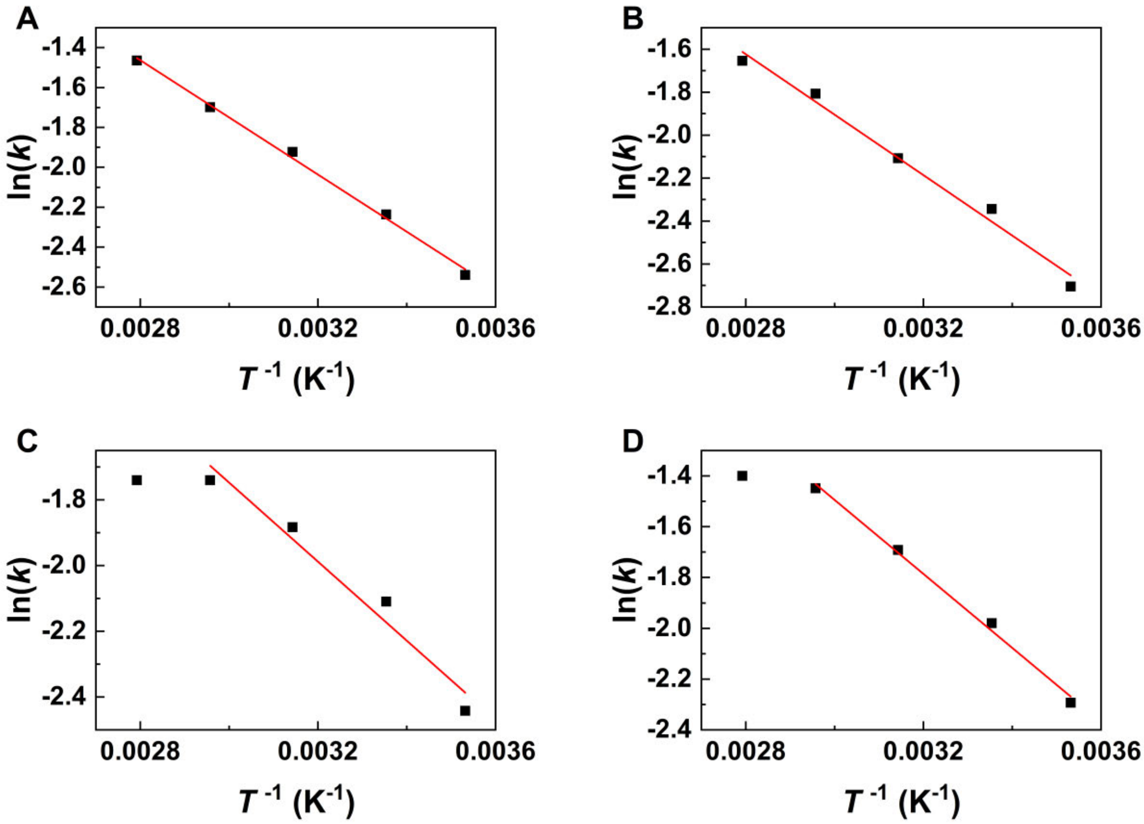

Figure 8.9: Arrhenius plots for the SAP microparticles containing the crosslinkers MBAA (A), EBAA (B), PBAA (C) and BBAA (D). The red line in each panel represents a linear fit, ignoring the plateau reached at high temperatures in the cases of (C) and (D).

The calculated activation energies of the swelling of the SAP microgels express a similar trend as the change rate of the swelling constants. At first, the activation energy E_a decreases as the hydrophobicity of the crosslinker increases. This trend again reverses for the crosslinker BBAA, as its activation energy increases in comparison to the less hydrophobic crosslinker PBAA. Furthermore, the calculated activation energy of the most hydrophobic crosslinker BBAA surpasses the activation energy of the most hydrophilic crosslinker used (MBAA).

In summary, the swelling kinetic studies of the SAP microgels synthesized in this study show that even though only a small part of the microgels' hydrophobicity is changed, there is a measurable effect on the swelling kinetics. Specifically, an increase in the hydrophobicity of the crosslinker within the SAP shows an increase of the influence of the gel-network diffusion during the swelling at 10 °C. Once the temperature of the swelling medium is at least 25 °C, the plots in all cases show almost perfect linearity. Using the linear relation of Equation 8.3, swelling constants can be calculated from which the change rate of the constants with temperature of the swelling medium as well as the activation energy of the swelling of the SAP can be determined. The data shows that at first, an increase in the hydrophobicity leads to a decrease of both the change rate of the swelling constant, as well as the activation energy to swell the microgels. This trend in both cases is broken as the hydrophobicity increases further for the crosslinker BBAA. Both results are visualized together in **Figure 8.10**.

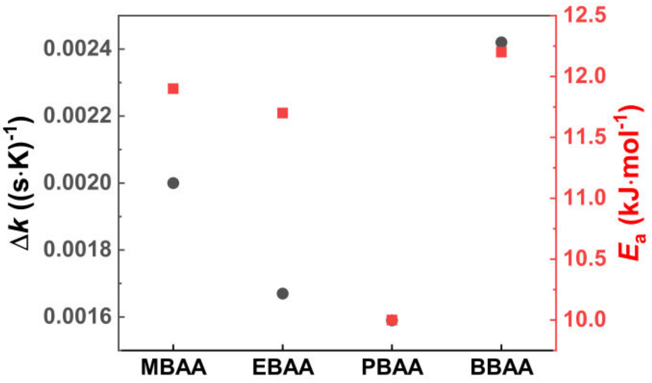

Figure 8.10: Calculated change rates of the swelling constants and activation energies of the microgel swelling for microgels containing the four different crosslinkers.

As a result, we conclude that there are at least two separate influences of the crosslinkers hydrophobicity on the SAP microgel, which seem to have opposite effects on the swelling kinetics of the microgel and partially compete with one another. One influence of the crosslinker hydrophobicity was previously described by Bromberg et al. The authors described that a higher hydrophobicity of co-monomers during the gel creation will lead to an increased degree of porosity of the gels.[11] Such an increased porosity of the microgel in our case would come from increasing *apparent* crosslink to crosslink distance, which may also be conceived as the distance between *effective* crosslinking nodes that actually consist of several locally close-by crosslinks. This kind of spatial inhomogeneity of the microgel crosslinking density can be expected to lead to a decrease in the activation energy needed for the swelling of the gel, as it facilitates solvent transport to and from the gel and is indeed observed for the crosslinkers MBAA to PBAA.

A competing effect of the hydrophobicity of the crosslinker might be the emergence of hydrophobic domains within the microgel, as detected in small-angle neutron scattering (SANS) experiments on poly (acrylic acid) microgels by Bromberg et al.[16] These hydrophobic domains might increase the activation energy of the swelling, as they need to be broken upon swelling. This effect should compete with the before-mentioned effect of increased porosity. Since the trends observed in both the change rates of the swelling constants as well as the activation energy reverse as the hydrophobicity of the crosslinker increases from PBAA to BBAA, we conclude that the effect of the hydrophobic domains in BBAA dominates over the increased porosity effect. Further support for this conclusion is given by the calculated reactivity ratios r_2 of the corresponding *N*-alkylacrylamides, for which we found that with an increase of the hydrophobicity of the *N*-alkylacrylamides r_2 increases. Furthermore, in the case of *N*-butylacrylamide, the hydrophobicity of the co-polymer lead to a phase separation immediately after initiation. This finding is a strong indication that in the case of the crosslinker BBAA, a microphase separation happened during the gelation-process of the droplets, which can be associated to the formation of hydrophobic domains within the microgel.

8.9 Conclusion

In this article, we systematically isolated the influence of the crosslinker hydrophobicity on the swelling kinetics of SAP microgels. We found two counteracting effects on the swelling kinetics resulting from an increase of the hydrophobicity of the crosslinker. The increase of the spatial crosslinking inhomogeneity of the microgels leads to a decrease of the activation energy of the swelling, which reverses at a further increase of the hydrophobicity of the crosslinker due to dominance of a second effect: the emergence of hydrophobic domains in the microgel. However, our research shows a narrow window in which an increase of the crosslinker hydrophobicity can have a positive effect especially for applications, in which fast swelling of dried hydrogel particles is desired.

8.10 References

[1] L. Yahia, *J Biomed Sci* **2015**, *04*.

[2] S. Behera, P. A. Mahanwar, *Polymer-Plastics Technology and Materials* **2020**, *59*, 341.

[3] P. Gupta, K. Vermani, S. Garg, *Drug Discovery Today* **2002**, *7*, 569.

[4] T. Tanaka, D. J. Fillmore, *The Journal of Chemical Physics* **1979**, *70*, 1214.

[5] Y. Li, T. Tanaka, *The Journal of Chemical Physics* **1990**, *92*, 1365.

[6] A. M. Atta, E. M. Abdel-Bary, K. Rezk, A. Abdel-Azim, *J of Applied Polymer Sci* **2009**, *112*, 114.

[7] J. Jovanovic, B. Adnadjevic, A. Kostic, *J of Applied Polymer Sci* **2010**, *116*, 1036.

[8] K. Sunitha, R. Sadhana, D. Mathew, C. P. Reghunadhan Nair, *Designed Monomers and Polymers* **2015**, *18*, 512.

[9] T. SHARMA, G. MADRAS, *Bull Mater Sci* **2016**, *39*, 613.

[10] J. Xie, X. Liu, J. Liang, Y. Luo, *J of Applied Polymer Sci* **2009**, *112*, 602.

[11] L. Bromberg, M. Temchenko, V. Alakhov, T. A. Hatton, *Langmuir* **2005**, *21*, 1590.

[12] K. M. Huh, N. Baek, K. Park, *Journal of Bioactive and Compatible Polymers* **2005**, *20*, 231.

[13] B. Adnadjevic, J. Jovanovic, *J of Applied Polymer Sci* **2008**, *107*, 3579.

[14] A. S. Kipcak, O. Ismail, I. Doymaz, S. Piskin, *Journal of Chemistry* **2014**, *2014*, 1.

[15] J. Tanasić, T. Erceg, L. Tanasić, S. Baloš, O. Klisurić, I. Ristić, *Reactive and Functional Polymers* **2021**, *169*, 105085.

[16] L. Bromberg, M. Temchenko, G. D. Moeser, T. A. Hatton, *Langmuir* **2004**, *20*, 5683.

[17] T. K. Mudiyanselage, D. C. Neckers, *J. Polym. Sci. A Polym. Chem.* **2008**, *46*, 1357.

[18] E. O. Akala, P. Kopecková, J. Kopecek, *Biomaterials* **1998**, *19*, 1037.

[19] Ö. B. Üzüm, S. Kundakci, H. B. Durukan, E. Karadağ, *J of Applied Polymer Sci* **2007**, *105*, 2646.

[20] A. Kostic, B. Adnadjevic, A. Popovic, J. Jovanovic, *J Serb Chem Soc* **2007**, *72*, 1139.

[21] S. Seiffert, W. Oppermann, *Macro Chemistry & Physics* **2007**, *208*, 1744.

[22] S. Seiffert, *Polym. Chem.* **2017**, *8*, 4472.

[23] A. R. Khare, N. A. Peppas, *Biomaterials* **1995**, *16*, 559.

[24] R. Seemann, M. Brinkmann, T. Pfohl, S. Herminghaus, *Reports on Progress in Physics. Physical Society (Great Britain)* **2012**, *75*, 16601.

[25] H. M. Shewan, J. R. Stokes, *Journal of Food Engineering* **2013**, *119*, 781.

[26] E. Tumarkin, E. Kumacheva, *Chemical Society Reviews* **2009**, *38*, 2161.

[27] B. Lu, M. D. Tarn, N. Pamme, T. K. Georgiou, *Journal of Materials Chemistry. B* **2015**, *3*, 4524.

[28] F. Di Lorenzo, S. Seiffert, *Macromol. React. Eng.* **2016**, *10*, 201.

[29] F. Tüdöds, T. Kelen, T. F. Berezhnikh, *J. Polym. Sci., C Polym. Symp.* **1975**, *50*, 109.

9. Further projects

In this chapter two further projects are described. Project 9.1 was an addition to project III (chapter 8). The aim of the project was to do light scattering experiments on polymer gels researched in project III and to gain more information on the polymer networks and their structures.

Project 9.2 was in co-operation with [redacted] an exchange student from Italy. In this project the aim was to together develop a microfluidic experimental setup with the unique requirement of having to heat all components prior to the creation of the droplets, which included the microfluidic device, to 75– 80 °C, to keep the dispersed phase in the sol state.

9.1 Light scattering experiments on Gels

Investigating the gel-structures of microgels within a dispersion is not possible as the scattering of the moving microparticles themselves makes it impossible to ascertain information of their polymer network. For this reason, macro gels instead of microgels were used during the light scattering experiments.

To keep at least some correlation between the macro gels and the microgels of project III the composition of the macro gels was kept identical to those of the microgels. As there however was no dispersed and continuous phase needed, the 1.00 g of acrylic acid was only diluted by 3.00 mL of milli-Q water prior to the addition of 0.56 g of sodium hydroxide solution (50 %). After addition of 0.3 mol% of the crosslinker versus the acrylic acid, the solution was shaken (250 rpm) over night to dissolve the crosslinker. As crosslinkers *N,N'*-methylenebisacrylamide (MBAA), *N,N'*-ethylenebisacrylamide (EBAA), *N,N'*-propylenebisacrylamide (PBAA), and *N,N'*-butylenebisacrylamide (BBAA) were used again as in the previous project. After addition of 40 µL of TEMED the solution was filtered into the light scattering cuvette. 5 mg of APS were dissolved in 0.43 mL of milli-Q water and filtered into the light scattering cuvette as well. After thorough mixing a Teflon plug was inserted just above the solution and the light scattering cuvette closed and sealed using Teflon tape. The cuvette was then placed into an oven at 40 °C for two hours for the polymerization to take place.

Thereafter the polymer within the cuvette could be placed into the light scattering setup. The experimental setup, already mentioned in the theoretical background in chapter **1.3.3**, contained a laser with a wavelength of 632.8 nm. The light scattering of the polymer samples was investigated at 30°, 50°, 70°, 90°, 110° and 130°. At each angle 300 measurements (speckles) were measured each for 60 seconds. The data was investigated using a self-written python script and the program LSApp4 written in MATLAB by [redacted]. The resulting speckle patterns at 30° of the four different polymer gels can be seen in the following figure.

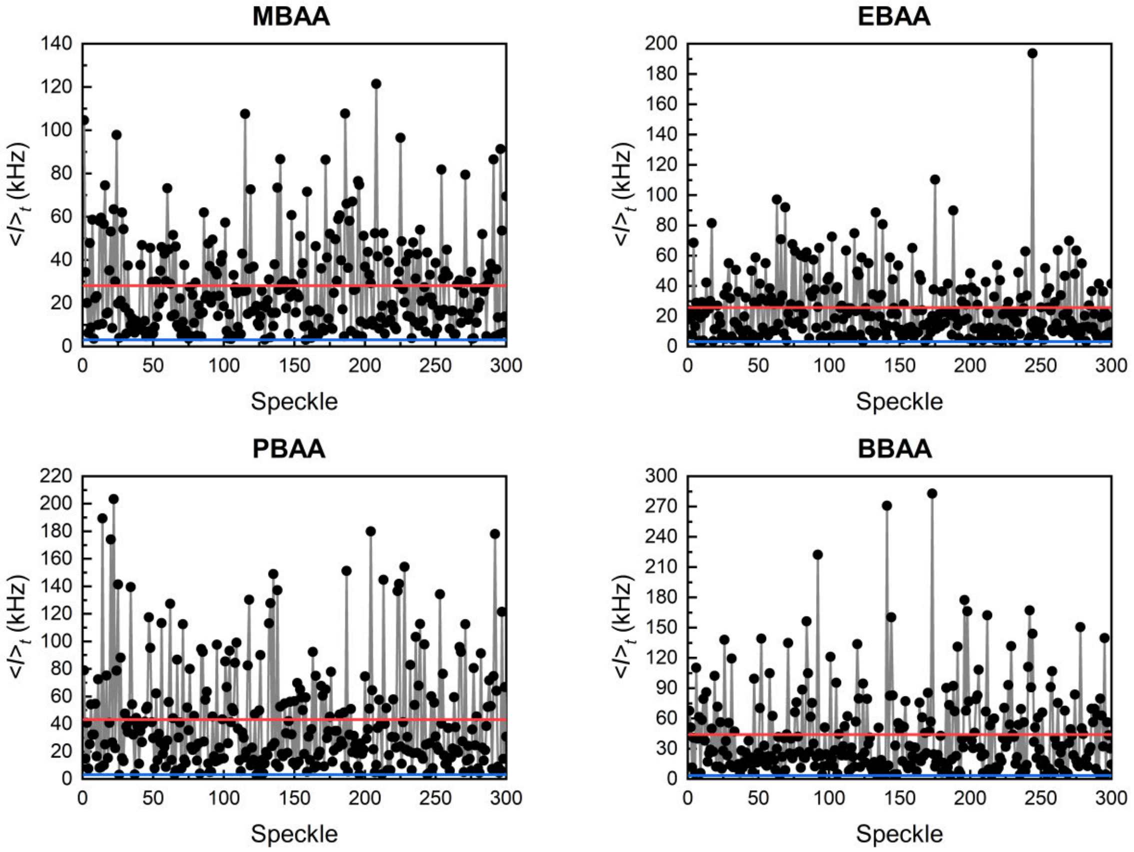

Figure 9.1: Speckle patterns of the four polymer gels containing the crosslinkers MBAA, EBAA, PBAA and BBAA. The red line indicates the I_{excess} and the blue line indicates I_{fluid} of the measurements at the corresponding angle.

Using the I_{excess} of each angle the static correlation lengths Ξ of each polymer can be calculated using the methods of Debye-Bueche, Guinier and Ornstein-Zernike, using the y-intercept and slope of the corresponding linear regressions from the plots of the excess scattering intensity against q^2 (see table 1.1). The plots and corresponding results are shown in **figure 9.2** and **table 9.1** below.

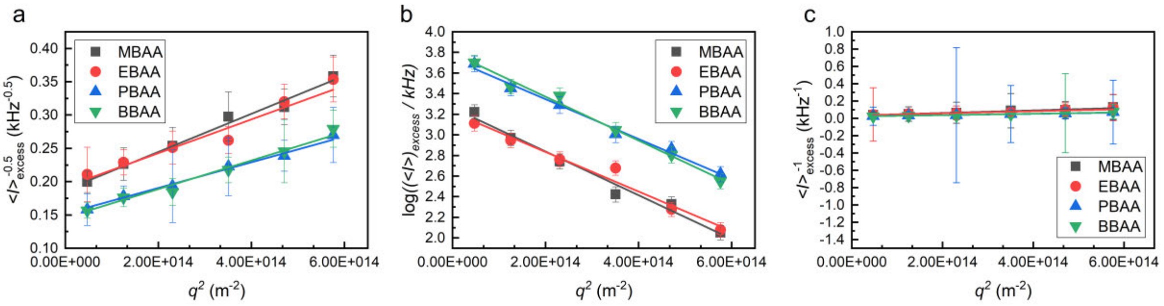

Figure 9.2: Plots of the excess scattering intensity I_{excess} vs q^2 and the linear regressions of the four polymer gels using the methods of Debye-Bueche (a), Guinier (b) and Ornstein-Zernike (c). The static correlation lengths can then be calculated using the slopes and y-intercept of the corresponding fits.

Table 9.1: Static correlation length of the different polymer gels containing the crosslinkers MBAA, EBAA, PBAA and BBAA.

Crosslinker	$\Xi_{\mathrm{Debye-Bueche}}$ **(nm)**	Ξ_{Guinier} **(nm)**	$\Xi_{\mathrm{Ornstein-Zernike}}$ **(nm)**
MBAA	39.1±1.0	46.1±1.6	67.5±2.5
EBAA	36.3±2.9	43.8±1.9	59.0±9.9
PBAA	35.6±0.8	44.0±1.1	57.9±1.0
BBAA	38.4±1.6	46.1±1.2	63.7±4.2

The calculated static correlation lengths of the four different polymers summarized in table 9.1 generally seem to increase as the method changes from Debye-Bueche to Guinier and finally to Ornstein-Zernike. Regarding the static correlation lengths calculated by each method any trend is broken by the uncertainties, with the uncertainty of the static correlation lengths calculated for EBAA in each method being the largest. Keeping the uncertainties in mind the static correlation lengths calculated for the different crosslinkers are all very close together, to almost constant.

In literature the static correlation lengths are used as indications of the spatial homogeneity or inhomogeneity of the polymer gels. For a free radical polymerization, it is expected to have values between $10 - 100$ nm.[1] Therefore, all calculated values are within the expected range, with the differences between the methods likely a result of the different bases for their calculation. In conclusion there could be no measurable effect found of the crosslinkers hydrophobicity on the static correlation lengths of the macro gels. There are two possible reasons this could be the case. Firstly, the crosslinkers hydrophobicity increase results from the single addition of a further methylene group. This could simply be too little to measure a noticeable effect in macro gels. Secondly in the case of the macro gels, the free radical polymerizations own effects on the polymer network structure may also obscure the effect of the crosslinkers hydrophobicity, which was the reason microfluidics and microgels had been used during project III.

Following the evaluation of the static light scattering data, the dynamic light scattering data was analyzed to calculate the dynamic correlation lengths ξ_{dyn} using the partial heterodyne method by Joosten et al. (see equation 9.1).[2] In the following, the correlation data was then fitted using a simple exponential function, with example fits of each polymer gel shown in **figure 9.3**.

Partial heterodyne method to obtain $g_F^{(1)}(q,\tau)$:

$$g_{\mathrm{T,p}}^{(2)}(q,\tau) = \frac{\langle I(t)I(t+\tau)\rangle_{\mathrm{T,p}}}{\langle I(t)\rangle_{\mathrm{T,p}}^2} = X_{\mathrm{p}}^2 \cdot g_{\mathrm{F}}^{(1)}(q,\tau)^2 + 2X_{\mathrm{p}} \cdot (1 - X_{\mathrm{p}}) \cdot g_{\mathrm{F}}^{(1)}(q,\tau) + 1 \tag{9.1}$$

$$X_{\mathrm{p}} = \frac{\langle I_{\mathrm{F}}\rangle_{\mathrm{T}}}{\langle I\rangle_{\mathrm{T,p}}} \tag{9.2}$$

Mono-exponential fitting function:

$$g_{\mathrm{F}}^{(1)}(q,\tau) = \exp(-D_{\mathrm{HT}} \cdot q^2 \cdot \tau) \tag{9.3}$$

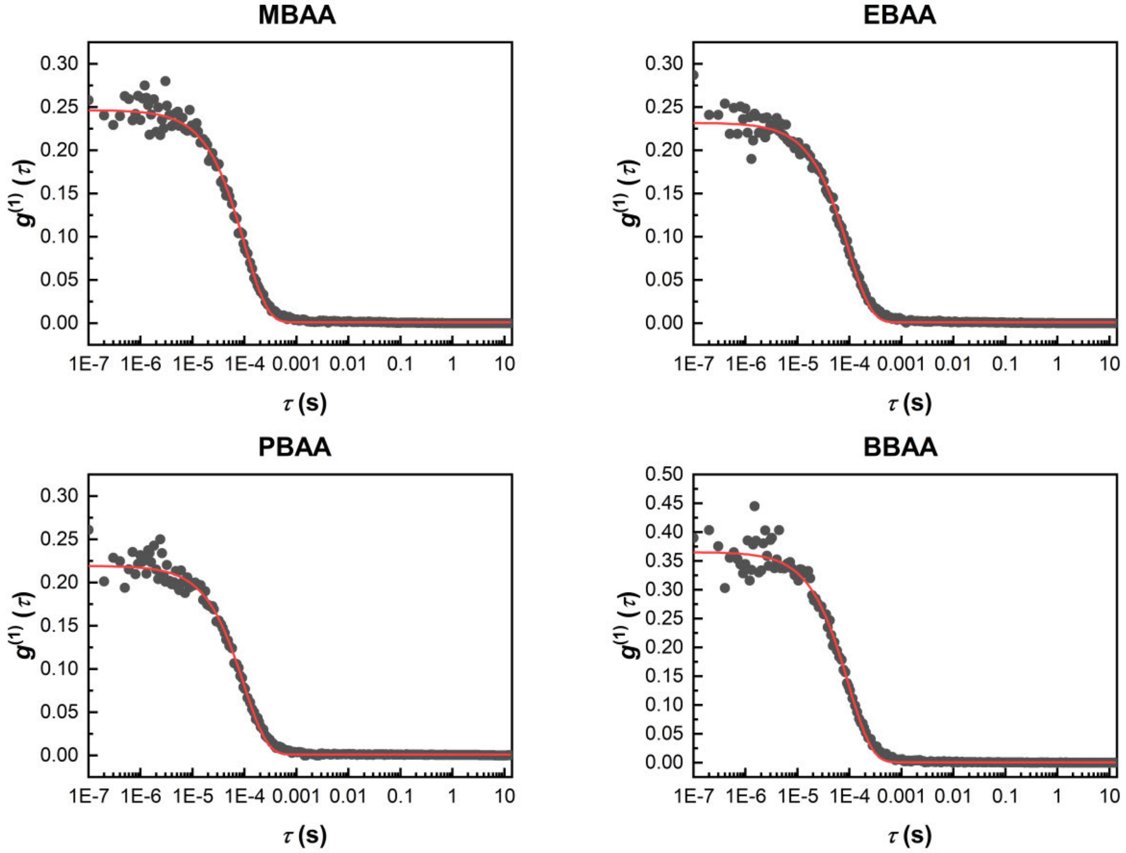

Figure 9.3: Examples of the correlation data and the mono-exponential fits of a single speckle of each of the different polymer gels.

Using the partial heterodyne method by Joosten et al., the inverse of the averaged characteristic relaxation time τ from the fitted data is plotted against q^2 as shown in **figure 9.4** and from the linear regression fits the dynamic correlation lengths calculated (shown in **table 9.2**).

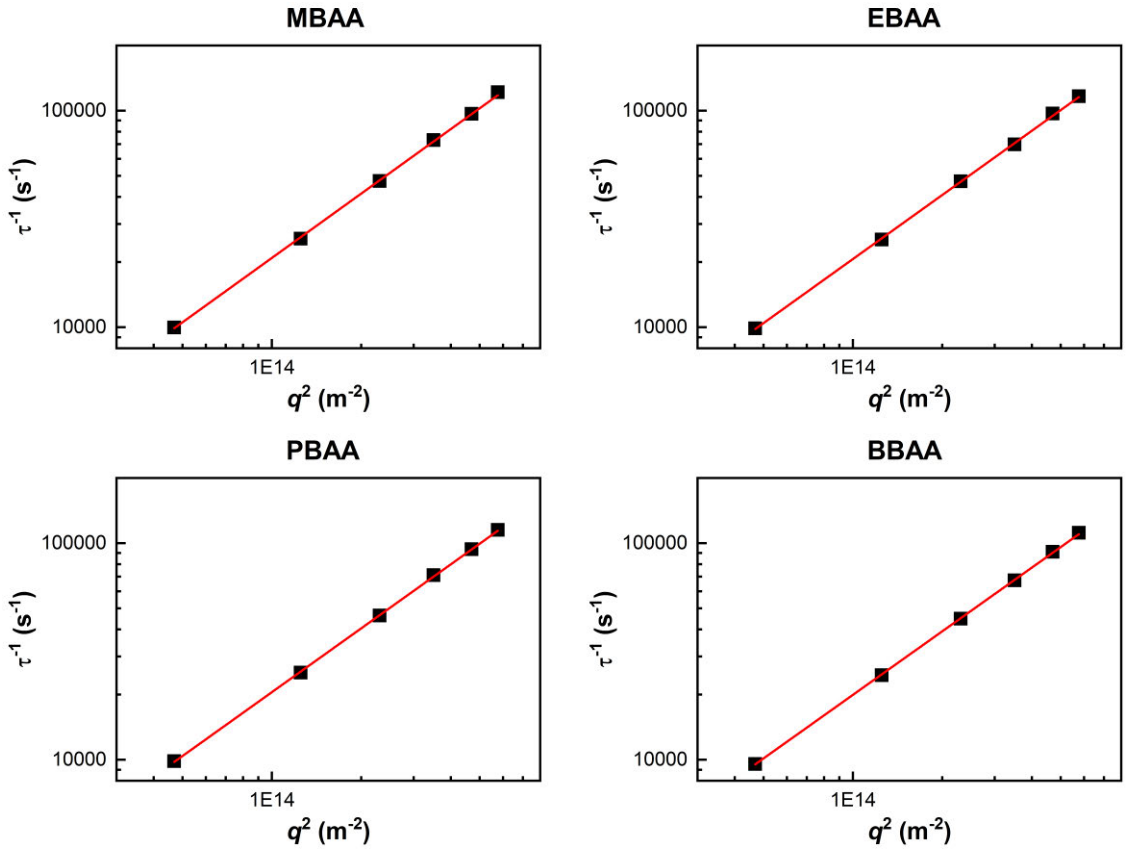

Figure 9.4: Linear regression through the averaged characteristic relaxation times plotted against q^2.

Table 9.2: Dynamic correlation lengths calculated using the Joosten approach for the four crosslinkers MBAA, EBAA, PBAA and BBAA.

Crosslinker	**ξ_{dyn} (nm)**
MBAA	1.18±0.02
EBAA	1.21±0.02
PBAA	1.22±0.02
BBAA	1.26±0.02

The dynamic correlation length in literature is associated with the network-strand fluctuations during the dynamic light scattering experiments and sometimes used as a reference of the mesh size of the gel.[1] With the expected values for the dynamic correlation lengths in the range of $1 - 10$ nm the calculated values of the four different polymer gels are on the lower end of the spectrum. Just as in the case of the static correlation lengths a possible trend is obscured by the uncertainties. However, in general it seems as if the dynamic correlation length does increase with the crosslinkers hydrophobicity. As this increase in the hydrophobicity stems from the increase of the methylene chain length connecting the two acrylamides, it could though be reasoned that the possible trend seen in table 9.2 could be a result thereof. Therefore, further research using crosslinkers with even longer methylene chains separating the acrylamides might be necessary, or alternatively using different crosslinkers, in which the hydrophobicity is changed using a different method than increasing the methylene chain lengths connecting the acrylamides.

9.2 Microfluidic synthesis of carbomer 974p-agarose hydrogels crosslinked via hyaluronic acid

The main goal of this project was the synthesis of carbomer974p-agarose hydrogel microgels (AC-HA hydrogels) crosslinked with hyaluronic acid (see **figure 9.5**) using droplet-based microfluidics. AC-HA macro gels had already previously been researched on as possible drug delivery systems, with its crosslinking giving an additional possibility of degradation.[3] The hope was that a successful synthesis of microgels would be a next step towards this application.

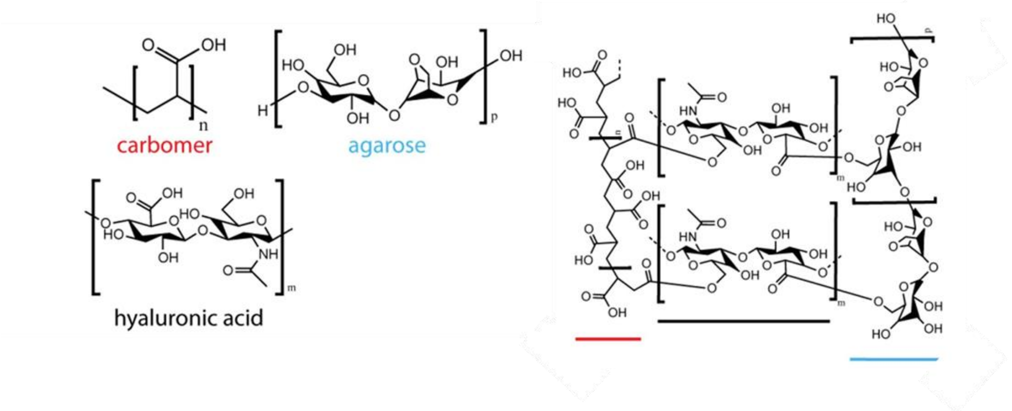

Figure 9.5: On the left the thee monomers composing the polymer network as shown on the right.[3]

Therefore, one requisite of the project was to keep both the synthesis method and the composition of the hydrogel microgels unchanged, as much as possible compared to the macro gels of the previous research.[3] Here a solution of the three monomers seen in figure 9.5 was heated to 80 °C. This initiated the condensation reaction with the polymer network remaining in the sol state until it cooled to around 37 °C, at which point the sol/gel transition took place, resulting in the macro gels.

In this project this same monomer solution would make up the dispersed phase, with the condensation reaction initiated prior to the start of the microfluidic experiment. As continuous phase low viscosity paraffin oil with SPAN 80 (3 wt%) as surfactant would be used.

Since in droplet-based microfluidics both the dispersed phase and the continuous phase is needed as fluids for droplet creation to function, the dispersed phase had to be kept in the sol state and thus heated to 75 – 80 °C. Furthermore, the continuous phase would also need to be kept at this temperature to prevent rapid sol/gel transition at the cross-section of the microfluidic device.

As microfluidic device a glass microfluidic device was used with a tip of around 200 µm. Since previous research (see chapter 5.2) had shown that with such devices increased flow rates are possible. This eased the challenge to maintain the temperatures using the *HD ULTRA* syringe pumps from *Harvard* as the flow time until the droplets were created was minimized. However, to maintain the microgel production for as long as possible the transport and the mixing section (syringes and the microfluidic device) as well as the polyethylene tubing in between had also to be heated to 75– 80 °C as shown schematically in **figure 9.6.**

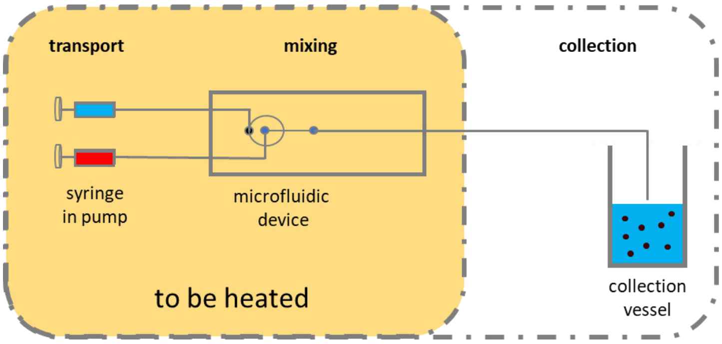

Figure 9.6: Schematic of microfluidic setup with heated sections in the yellow box. This includes the two syringes within the syringe pumps, the microfluidic device and the connecting polyethylene tubing.

With the extreme time constraint of only three months for the project, solutions had to be at times improvised. Hence, as depicted in **figure 9.7** both the syringes in the transport section are temperature controlled using heating mantels made of glass tailored for both a 5 mL and 10 mL syringe by the local glass workshop. The plastic syringes were glued into the glass heating mantel using epoxy glue to seal the gap between syringe and the heating mantel. The reason no premade syringes with heating mantels were used was, besides the time limit, that it was feared that the gelation of the dispersed phase within the syringe may make a reuse of the syringe impossible.

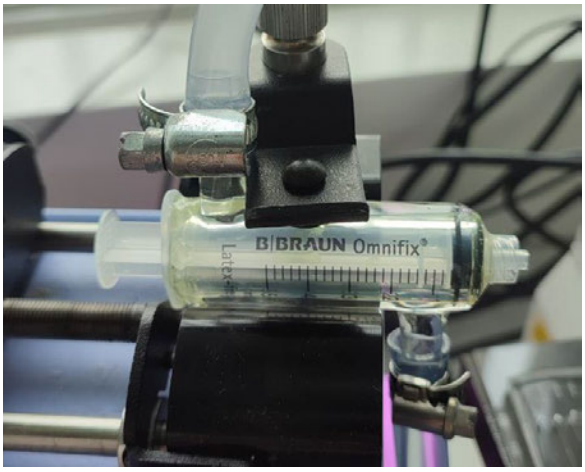

Figure 9.7: Heating mantel for the 5 mL syringe with syringe glued into. The heating mantel ensures the microfluidic phase has a constant temperature of 75–80 °C. [4]

With temperature control of the syringes achieved, the microfluidic device and connecting polyethylene tubing had to be temperature controlled. First experiments using the microfluidic temperature device already used in project I proved, that it was not capable of maintaining the high temperature needed rendering the production of microgels with it impossible.

However, the heating device was capable to be used as a heating source for a water bath in which the entire microfluidic device was submerged. The water bath would also contain most of the connecting polyethylene tubing, thereby keeping both at 75– 80 °C. As the tubing would need to be held underneath the water surface small weights in the form of pebbles were used to hold them down. Once the microgels had been formed the exit tubing would exit the water bath, as it is no longer necessary to keep the droplets temperature above the sol/gel transition temperature. An image of the microfluidic setup within the water bath can be seen in **figure 9.8**.

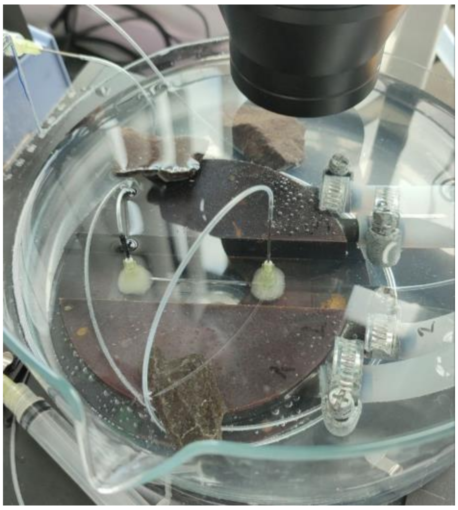

Figure 9.8: Microfluidic experimental setup modified to keep the temperature of both dispersed and continuous phase at 75 –80 °C until the microgels are formed. [4]

Using the above shown microfluidic experimental setup [redacted] successfully synthesized microgels at flowrates of 1.5 $\frac{\mathrm{mL}}{\mathrm{h}}$ for the dispersed phase and 4.5 $\frac{\mathrm{mL}}{\mathrm{h}}$ for the continuous phase. The microgels with diameters around 200 µm showed sponge-like structures allowing for the possible use of them as drug delivery systems in the future. Her results were published in her dissertation “DIFFUSION MOTION IN CONFINED SYSTEMS: NMR EXPERIMENTAL APPROACHES” publicly accessible after the 08.04.2025.

9.3 References

[1] S. Seiffert, *Progress in Polymer Science* **2017**, *66*, 1.

[2] M. Shibayama, *Bulletin of the Chemical Society of Japan* **2006**, *79*, 1799.

[3] F. Pizzetti, A. Maspes, A. Rossetti, F. Rossi, *European Polymer Journal* **2021**, *161*, 110843.

[4] V. Vanoli, *Diffusion motion in confined systems: NMR experimental approaches* **2024**.

10. Conclusions and Outlook

This thesis is comprised of several projects around the topic of droplet-based microfluidics and the microgels synthesized via this method. The focus hereby was on both the yields of the microfluidic experiments and to use the method to create microgels, with both structural control and regulated attributes such as for example LCST behavior and swelling characteristics.

In project I (chapter 3) modifying a microfluidic experimental setup to increase the yield of the microgels was the main focus. The reaction segment was completely redesigned. The original UV lamp was changed to the more powerful *OmniCure series 1500* UV lamp and the polyethylene tubing was replaced by an integrated glass capillary. After hydrophobically coating the microfluidic device using *Sigmacote*® droplet production remained stable at flowrates of 250 $\frac{\mu L}{h}$ for the dispersed phase and 500 $\frac{\mu L}{h}$ for the continuous phase. With these doubled flowrates compared to the unmodified setup the aim of increasing the microgel-yield was fulfilled. Furthermore, the used method of integrating a glass capillary into a microfluidic experimental setup could be used in future setups in which irradiation of the droplets is required.

Project II (chapters $4-7$) "*Core-shell interfacial interpenetration control for switchable elasticity*" focused on the creation of core-shell microgels made of temperature sensitive cores and a non-temperature sensitive shell. Through varying core-shell interconnection the Young's modulus would either increase as the core collapsed at higher temperatures (high degree of interconnection) or it would decrease (low degree of interconnection). With droplet-based microfluidics the synthesis method of choice in a first step the core-particles, made up of poly-NIPAM were synthesized. Several different preliminary microfluidic experiments using microfluidic devices with different channel sizes were conducted, with the optimal core-particles synthesized using 100 µm devices and an average core size of $\bar{d} = 122 \pm 8$ µm. Furthermore, the LCST-behavior of the core-particles was analyzed. It could be determined that the average diameter would shrink to about 40 % of its original size if the temperature was above 37.5 °C.

Following the successful core-particle synthesis the non-temperature sensitive shell-precursor polymer was synthesized along with a photosensitizer. As shell-precursor polymer a copolymer of acrylamide (AAm) and *N*-(2-(3,4-dimethyl-2,5-dioxo-2,5-dihydro-1H-pyrrol-1-yl)ethyl)acrylamide (DMMIAAm) was prepared via a free radical polymerization. This linear copolymer can be photo-crosslinked by UV-radiation in the presence of the photosensitizer thioxanthone-2,7-disulfonate.

With all components necessary to create the core-shell particles, preliminary tests were conducted. In these the importance of the core-paste became evident, as if there was too much water within it, the core-flow would not remain consistent. Additionally, to ease the core-flow it was found that cooling the core-particles was beneficial. Besides the importance of the core-paste it also became evident, that the channel-sizes of the microfluidic setups needed to match those of the core-particles. In that regard new photomasks were designed and PDMS-devices created. A further minor adjustment (around 10 %) of the channel size was found to be possible by utilizing the swelling effect of organic solvents on PDMS.

To gain better control of the interpenetration depths of the shell-precursor polymer into the core-particles a UV-irradiation chamber was designed and constructed allowing the creation of core-shell particles with negligible interconnection of the two. For the creation of interconnected core-shell particles the core-shell droplets were first collected and then irradiated within the collection vial. Due to time restraints however the creation of core-shell particles with switchable elasticity could not be fulfilled. However, a good foundation for future research on this topic could be created, allowing the creation of core-shell microgels with controlled switchable elasticity for future uses as for example in the stem-cell differentiation.

Lastly in this project diffusion simulations of linear polymers into a defective polymer network were studied. With the results showing a dependence of the maximum penetration depths on the volume fraction of the diffusing polymer strands. As however no clear overall chain orientation of the diffusing linear polymer throughout the simulation box nor the rapid decrease of the diffusion speed at the interface was determinable, the polymer network itself was more closely analyzed. It could be determined that the strand lengths of the polymer chains of the polymer network varied extremely, with the majority being in the range of $1-10$ monomer units. As this high degree of inhomogeneity of the polymer network was however not intended nor representative of the core-particles created during the microfluidic experiments the creation of the defective polymer networks will have to be revised.

In project III (chapter 8) the focus was on the influence of the crosslinker hydrophobicity within the polymer microgel on the swelling kinetics. The microgel particles were synthesized using droplet-based microfluidics. In microfluidics the reaction heat can be dissipated effectively to the continuous phase, thus limiting other factors on the heterogeneities of the polymer network stemming from the polymerization method, the free radical polymerization.

The four crosslinkers investigated were *N,N'*-methylenebisacrylamide (MBAA), *N,N'*-ethylenebisacrylamide (EBAA), *N,N'*-propylenebisacrylamide (PBAA) and

N,N'-butylenebisacrylamide (BBAA), with the hydrophobicity of the crosslinkers increasing with the alkyl-chain length. However, prior to the investigation of the swelling kinetics the equal incorporation of the different crosslinkers into the polymer networks was analyzed. This was done by copolymerizing acrylic acid and the corresponding *N*-alkylacrylamides creating linear copolymers from which the reactivity ratios were calculated. The reactivity ratios showed that with increasing hydrophobicity the *N*-alkylacrylamides would increasingly tend to homopolymerize. In the case of the most hydrophobic comonomer *N*-butylacrylamide this led to the copolymer no longer being soluble in water making the determination of the reactivity ratios in this case impossible. However, at low *N*-alkylacrylamide concentration the incorporation of the comonomers was similar, it was concluded that this would also be the case for the crosslinkers in the polymer gels.

The swelling experiments of the microgels containing the four crosslinkers showed that in case of the first three crosslinkers MBAA, EBAA and PBAA the activation energy of the swelling of the microgels decreased with increasing hydrophobicity of the crosslinker. In the case of BBAA however the trend reversed with the activation energy of the swelling of the microgels increasing again even surpassing that of the most hydrophilic crosslinker investigated. It was concluded that the crosslinkers hydrophobicity had two competing effects on the polymer networks: firstly, increasing porosity of the polymer gels with increased hydrophobicity decreasing the activation energy of the swelling of the microgels. And secondly the emergence of hydrophobic domains with increasing hydrophobicity of the crosslinker leading to increasing activation energies of the swelling of the microgels. With the first effect dominating the second in the case of the crosslinkers *N,N'*-methylenebisacrylamide, *N,N'*-ethylenebisacrylamide and *N,N'*-propylenebisacrylamide and the second effect dominating the first in the case of *N,N'*-butylenebisacrylamide. Understanding the effect of the hydrophobicity of the crosslinker on the swelling kinetics of microgels could further research into new products in which the swelling of microgels plays an important role.

In chapter 9 two smaller projects were described. In the first project polymer macro gels, similar in composition to the microgels of project III (chapter 8), were investigated using light scattering to better understand the structure of the polymer gels. The data allowed the determination of the static correlation length Ξ and the dynamic correlation length ξ. With the static correlation length often used as an indication of the homogeneity of the polymer gels, the determined lengths using the methods of Debye-Bueche, Guinier and Ornstein-Zernike however showed no clear trend and instead remained almost constant. This was mainly due to the uncertainties of the determined values. The calculated values however do fall into the expected range of the static correlation lengths of polymer gels created by free radical polymerization. In the case of the dynamic correlation lengths ξ calculated using the partial heterodyne method a trend also is unclear due to the uncertainties. The general increase of the dynamic correlation lengths could simply be a result of the increasing methylene chain lengths of the crosslinkers, which also lead to their increasing hydrophobicity. It therefore might be necessary to investigate further crosslinkers to determine if the seen increase is truly the result of the crosslinkers hydrophobicity or just a biproduct of their increased methylene chain.

In the second project, a microfluidic experimental setup was designed with the ability to heat both the transport and mixing segments to $75 - 80$ °C, to create carbomer974p-agarose hydrogel microgels crosslinked via hyaluronic acid. With the polymerization reaction being initiated prior to the start of the microfluidic experiment it was paramount to keep the temperature of the microfluidic experimental setup above the sol/gel transition temperature until the droplets had been created at the microfluidic cross-section. Furthermore, there was a time limit of three months until the project had to be concluded. As solutions to the heating challenge, heating mantels made of glass for the syringes and a water bath heated by a microfluidic chip heating device were created and successfully employed, thereby possibly taking the next step to successfully create carbomer974p-agarose microgels for drug admission.

Publications

1. *Structure and Dynamic Evolution of Interfaces between Polymer Solutions and Gels and Polymer Interdiffusion: A Molecular Dynamics Study*

   [redacted], Torsten Gereon Linder, [redacted]

   Macromolecules, **2024**, 57, 5545-5559.

   ABSTRACT: Letting free polymers diffuse from solution into a cross-linked polymer gel is often a crucial processing step in the synthesis of multiphase polymer-based gels, e.g., core−shell microgels. Here, we use coarse-grained molecular dynamics simulations to obtain molecular insights into this process. We consider idealized situations where the gel is modeled as a regular polymer network with the topology of a diamond lattice, and all free polymers and strands have the same length and consist of the same type of monomers. After the gel and the polymer solution were brought into contact, two time regimes are observed: an initial compression of the gel caused by the osmotic pressure of the solution was followed by an expansion due to swelling. We characterize the time evolution of density profiles, the penetration of free polymers into the gel, and the connection between the gel and solution phase. The interfacial structure locally equilibrates after roughly100 chain relaxation times. At late times, the free chains inside the gel undergo a percolation transition if the polymer concentration in the gel exceeds a critical value, which is on the same order as the overlap concentration. The fluctuations of the interface can be described by a capillary wave model that accounts for the elasticity of the gel. Based on this, we extracted the interfacial tension of the gel−solution interface. Interestingly, both the interfacial tension and the local interfacial width increase with increasing free polymer concentration, in contrast to liquid−liquid interfaces, where these two quantities are typically anticorrelated.

2. *Influence of the Crosslinker Hydrophobicity on the SwellingKinetics of Poly(Acrylic Acid) Microgels*

   Torsten Gereon Linder, [redacted]

   Macromol. Chem. Phys. **2024**, 225, 2400138

   ABSTRACT: Superabsorbent polymer gels are widely used in commercial areas, such as in hygiene products. A key aspect in these and other applications is the gel swelling kinetics, and a key factor of influence on that is the hydrophobicity of the gel. This paper reports on the synthesis of superabsorbent polymer microgel particles with four differently hydrophobic crosslinkers: *N,N'*-methylenebisacrylamide (MBAA), *N,N'*-ethylenebisacrylamide (EBAA), *N,N'*-propylenebisacrylamide (PBAA), and *N,N'*-butylenebisacrylamide(BBAA). This work uses droplet-based microfluidics to produce uniform and well-defined microgel specimen and study the influence of the crosslinker hydrophobicity on the swelling kinetics. In particular, this work determines swelling constants and their dependencies on the temperature of the swelling medium as well as the activation energies of swelling in relation to the crosslinker hydrophobicity. This work finds two competing effects, leading to a narrow window in which the activation energy of the swelling of the microgels decreases with increasing crosslinker hydrophobicity.

Conference Contributions

1. *Core-shell interfacial interpenetration control forms microgels with switchable elasticity*

   Torsten Gereon Linder, [redacted]

   Poster presentation – ECIS 2022 in Chania, Crete, 4 – 9 September 2022

   ABSTRACT: Thermo-sensitive gels exhibit controllable swelling-deswelling transitions upon change of temperature, thereby switching their elastic and Young's moduli. On top of that, the transition leads to a change in their adhesiveness. To decouple these two effects, we form core-shell particles with a thermo-sensitive core and a thermo-insensitive shell. These microgels take advantage of the swelling-deswelling transition, while the outer adhesiveness remains constant. To achieve this goal, droplet-based microfluidics serves us to form microgel core-shell particles of about 400 µm diameter, containing a thermo-sensitive hydrogel core made of poly(N-isopropylacrylamide) (poly-NIPAM) about 300 µm in diameter and a non-thermo-sensitive shell made of an about 100 µm thick shell of polyacrylamide. Through variation of the time of gelation of the shell via UV irradiation, the extent of interpenetration of the core and shell is varied, resulting in core-shell particles with interconnected cores and shells and particles with negligible core-shell interconnection. Due to the thermo-sensitive core of the core-shell particles, the core deswells upon an increase of the temperature, changing the particle surficial Young's modulus in a way that decisively depends on the interconnection of the shell and core.

List of Abbreviations

3D	three dimensional
AAm	acrylamide
APS	ammonium persulfate
BBAA	*N,N′*-butylenebisacrylamide
BBAA*	*N*-butylacrylamide
Ca	Capillary number
CMC	critical micelle concentration
DII	degree of interfacial integration
DLS	dynamic light scattering
DMMIAAm	*N*-(2-(3,4-dimethyl-2,5-dioxo-2,5-dihydro-1H-pyrrol-1-yl)ethyl)acrylamide
EBAA	*N,N′*-ethylenebisacrylamide
EBAA*	*N*-ethylacrylamide
FID	Free Induction Decay
fps	frames per second
FT	Fourier transformation
i.e.	that is
IUPAC	International Union of Pure and Applied Chemistry
LCST	lower critical solution temperature
MBAA	*N,N′*-methylenebisacrylamide
MBAA*	*N*-methylacrylamide
NA	numerical aperture
NMR	nuclear magnetic resonance
PBAA	*N,N′*-propylenebisacrylamide
PBAA*	*N*-propylacrylamide
PDMS	poly(dimethylsiloxane)
poly NIPAM	poly(*N*-isopropylacrylamide)
polyHEMA	poly(2-hydoxyethyl methacrylate)
Re	Reynolds number
RTG	research training group
SANS	small-angle neutron scattering
SAP	superabsorbent polymer
SLS	static light scattering

TEMED	*N,N,N′,N′*-tetramethylethylenediamine
TMS	tetramethyl silane
TXS	thioxanthone-2,7-disulfonate
UV	ultra violet
V-50	2,2’-azobis(2-methylpropionamidine) dihydrochloride
We	Weber number

List of Symbols

Microfluidics

Ca	Capillary number
ΔG	Gibbs free energy
ΔH	Enthalpy
ΔS	Entropy
η	dynamic viscosity
h	height in this case of microfluidic channels
γ_{IF}	interfacial tension
L_0	characteristic size over which the interplay interaction of the inertial and viscous forces is to be calculated
ρ	density
Re	Reynolds number
T	temperature
v_{x}	flow speed in direction x
We	Weber number

Optical microscopy

d	diameter
d_{Abbe}	Abbe limit
d_{Rayleigh}	Rayleigh limit
d_{t}	diameter at time t
d_0	diameter of dried particle
λ	wavelength of light
n	refractive index
NA	numerical aperture
SD	swelling degree
t	time
τ_x	specific swelling times
k	swelling constant
E_a	activation energy

NMR spectroscopy

$\boldsymbol{\gamma}$	gyromagnetic ratio
$\boldsymbol{\omega}_\mathrm{L}$	Larmor frequency
$\boldsymbol{B}_0$	magnetic field
$\boldsymbol{I}$	nuclear spin
μ	dipole moment
$\boldsymbol{E}$	Energy
$\boldsymbol{k}$	Boltzmann constant
$\boldsymbol{M}_0$	total magnetization
$\boldsymbol{\delta}$	chemical shift
$\boldsymbol{f}_2$	mole fraction in the monomer solution
$\boldsymbol{F}_2$	mole fraction in the polymer
$\boldsymbol{r}_1, \boldsymbol{r}_2$	reactivity ratios

Light scattering on gels

$\boldsymbol{\alpha}$	polarizability
$\boldsymbol{k}$	wave vector
$\boldsymbol{\omega}$	frequency
$\boldsymbol{I}$	intensity
$\boldsymbol{R}$	Rayleigh ratio
$\left(\frac{\partial \boldsymbol{n}_\mathrm{D}}{\partial \boldsymbol{c}}\right)$	refractive index increment
$\boldsymbol{c}$	concentration
$\boldsymbol{M}$	molar mass
$\boldsymbol{N}_\mathrm{L}$	Avogadro constant
$\boldsymbol{r}$	radius
$\boldsymbol{V}$	volume
$\boldsymbol{q}$	scattering vector
$\boldsymbol{\delta c_C}$	frozen concentration fluctuations
$\boldsymbol{\delta c_F}$	dynamic thermal concentration fluctuation
$\boldsymbol{I}_\mathrm{E}$	excess scattering intensity
$\boldsymbol{\Xi}$	static correlation length
$\boldsymbol{m}$	slope

$\boldsymbol{b}$	y-intercept
$\boldsymbol{\xi}_{\mathbf{dyn}}$	dynamic correlation length
$\boldsymbol{g}_{\mathbf{T,p}}^{(2)}(\boldsymbol{q},\boldsymbol{\tau})$	second order correlation function
$\boldsymbol{g}_{\mathbf{F}}^{(1)}(\boldsymbol{q},\boldsymbol{\tau})$	field correlation function
$\boldsymbol{X}_{\boldsymbol{p}}$	ratio of intensity of the thermal fluctuations and the total intensity
$\boldsymbol{\tau}$	characteristic relaxation time

Diffusion simulations

$\boldsymbol{\tau}$	simulation steps
$\boldsymbol{dt}$	time laps within simulation
$\boldsymbol{R}_{\boldsymbol{g}}^{\mathbf{2}}$	radius of gyration
$\boldsymbol{M}_{\boldsymbol{a}}$	diffusion distance within the simulation box

Appendix

A1 Supporting Information to Project II.2

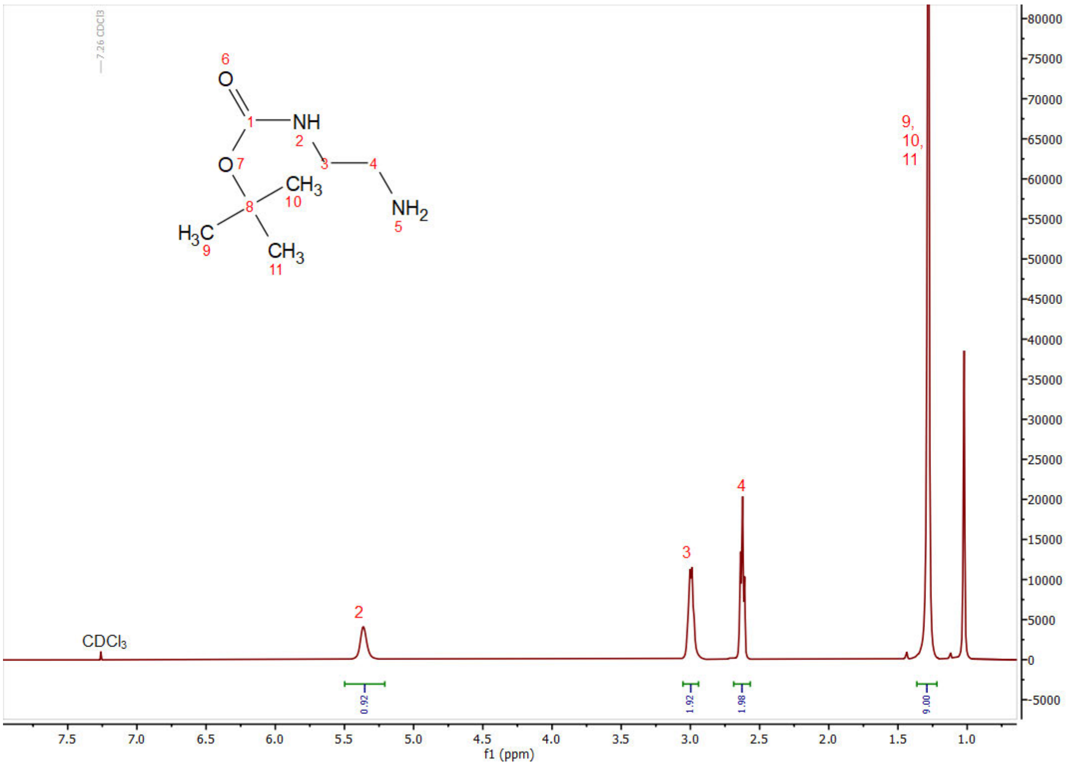

Figure A1.1: ^{1}H-NMR (400 MHz, $CDCl_3$) of tert-butyl (2-aminoethyl) carbamate.

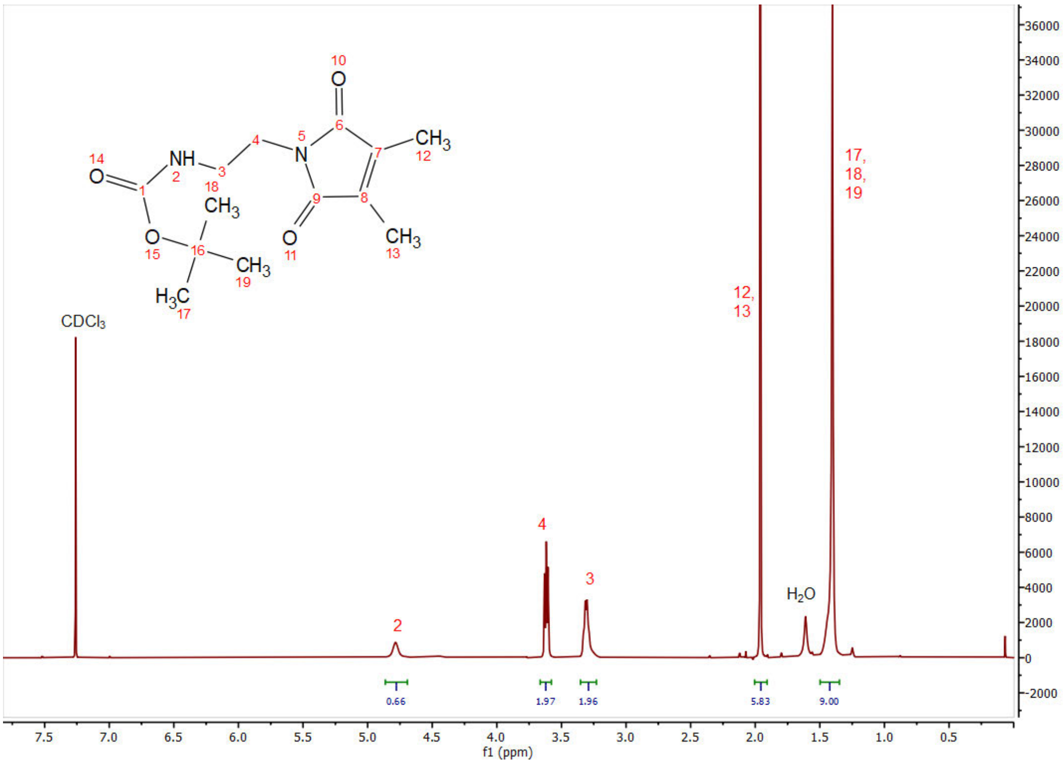

Figure A1.2: ^{1}H-NMR (400 MHz, $CDCl_3$) of tert-butyl (2-(3,4-dimethyl-2,5-dioxo-2,5-dihydro-1H-pyroll-1-yl)ethyl)carbamate.

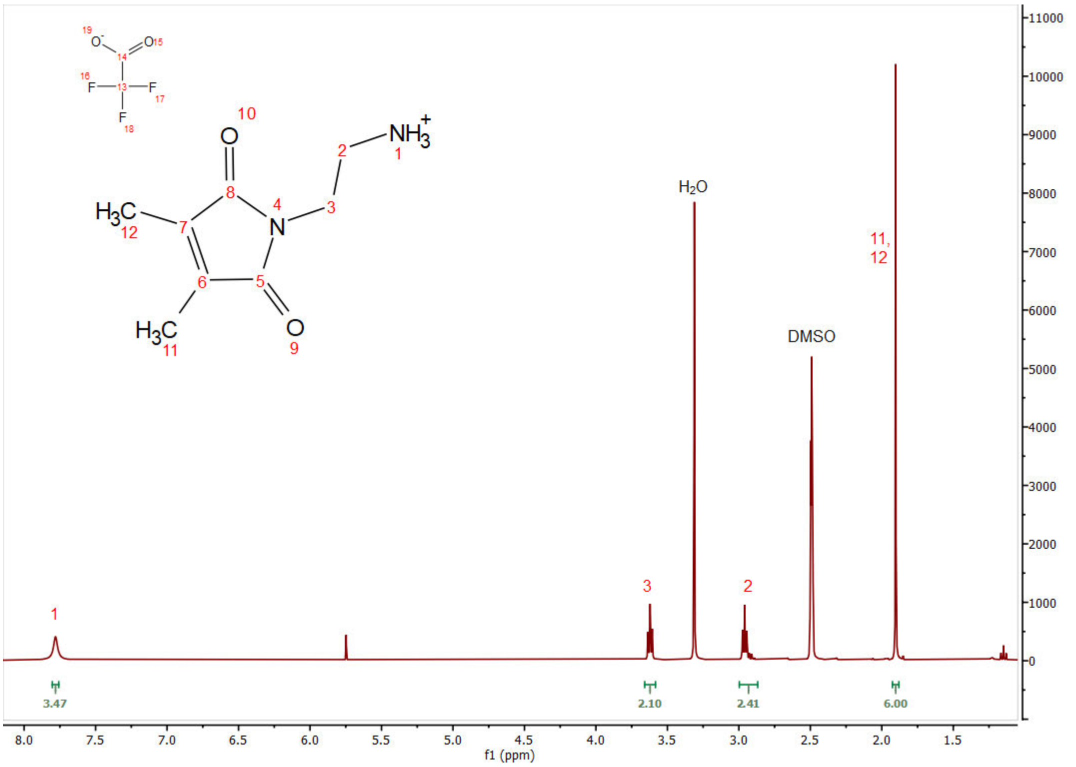

Figure A1.3: ^{1}H-NMR (400 MHz, DMSO-d_6) of 2-(3,4-dimethyl-2,5-dioxo-2,5-dihydro-1H-pyrrol-1-yl)ethan-1-aminium.

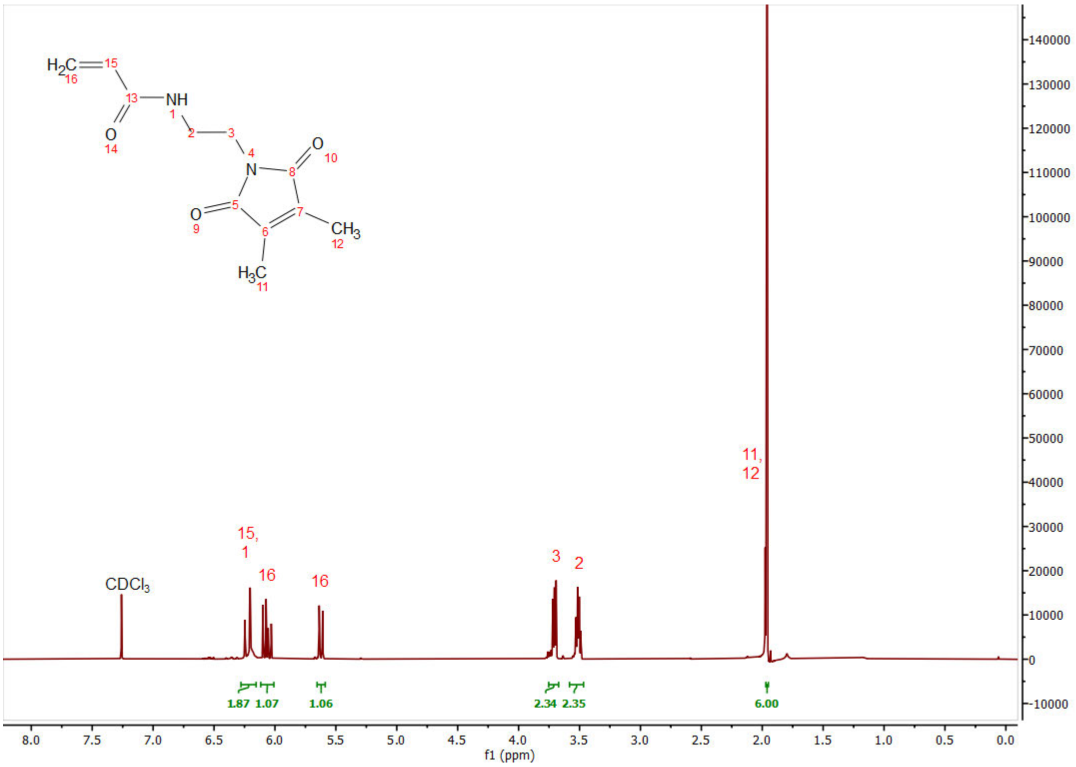

Figure A1.4: ^{1}H-NMR (400 MHz, CDCl$_3$) of N-(2-(3,4-dimethyl-2,5-dioxo-2,5-dihydro-1H-pyrrol-1 yl)ethyl)acrylamide.

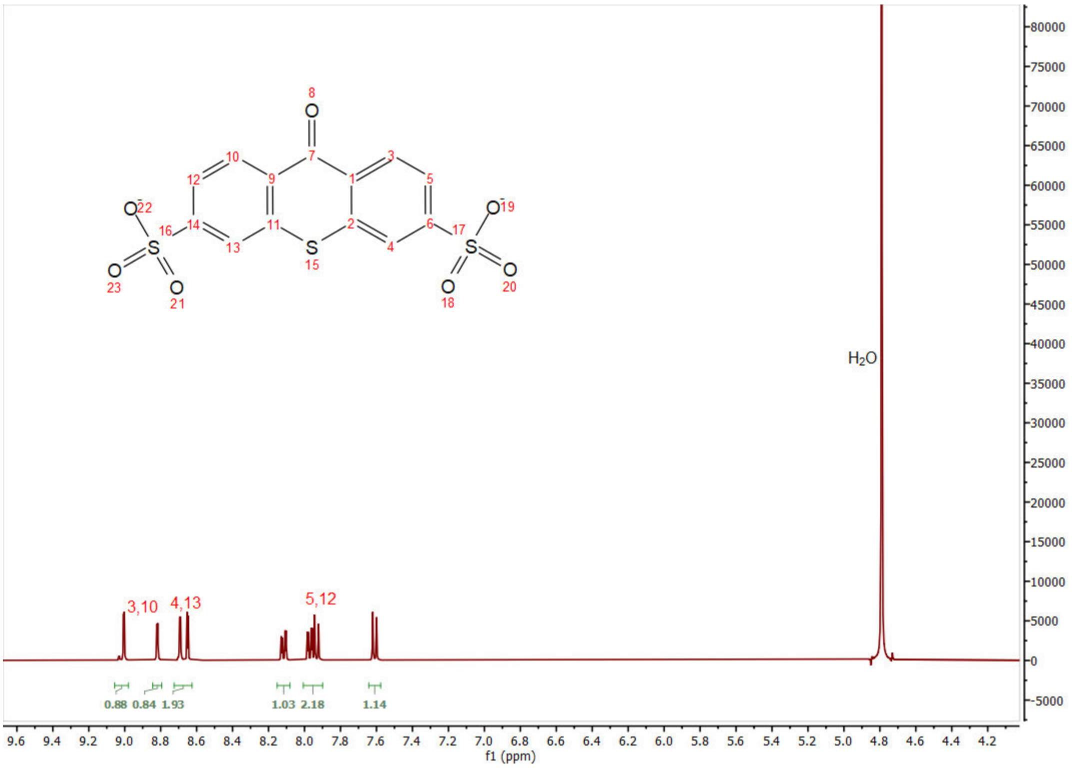

Figure A1.5: ^{1}H-NMR (400 MHz, D_2O) of thioxanthone-2,7-disulfonate.

A2 Supporting Information to Project II.3

python routine used to analyze density profile

```
import numpy as np
import gsd.hoomd
import freud
from tqdm import tqdm
from collections import defaultdict
import csv
import sys

Ntot = int(sys.argv[1])
samples = 11
n_bin = 200
data_jump = 1

##############################################################################
## loading in csv dictionary
##############################################################################

descriptorDict = defaultdict(list)

with open('description_file.csv', 'r') as data:

    csv_reader = csv.reader(data)
    rows = list(csv_reader)
for row in rows:
    descriptorDict[int(row[0])] = row[1]
a = descriptorDict[Ntot]
v=a.strip('][').split(', ')

##############################################################################
## parameters
##############################################################################

volfrac = v[0]
molefrac = v[1]
denseratio = v[2]

##############################################################################
## functions
##############################################################################

def truncate(n):
    n = float(int(n * 100))
    n/= 100
    return n
```

```
##############################################################################
## densityprofile
##############################################################################

datadummy =
gsd.hoomd.open(name='trajectory1_polymerized_network_diffusive_Ndiff_'+str(Nto
t)+'_vol_frac'+str(volfrac)+'_kT_1.000.gsd', mode='rb')

# exit()
time=int(len(datadummy)/data_jump)
samplearray=np.empty((0,time,n_bin,3),dtype=float)


for sample in tqdm(range(1,samples,1)):
    data =
gsd.hoomd.open(name='trajectory'+str(sample)+'_polymerized_network_diffusive_N
diff_'+str(Ntot)+'_vol_frac'+str(volfrac)+'_kT_1.000.gsd', mode='rb')
    print(len(data))

    siml=data[0].configuration.box[0]
    simly=data[0].configuration.box[1]
    simlz=data[0].configuration.box[2]

    sim_s= -(siml/2)
    sim_e=(siml/2)
    box_x=siml/n_bin
    dV = box_x*simly*simlz

    N_den_array = np.zeros((int(len(data)/data_jump),n_bin))
    gel_den_array= np.zeros((int(len(data)/data_jump),n_bin))
    box_mean_array= np.zeros((int(len(data)/data_jump),n_bin))

    #results_density=np.asarray((box_mean_array,gel_den_array,N_den_array)).T



    for frame in range (0,len(data),data_jump):

        i = int((frame-0)/data_jump)
        snap=data[frame]
        pos=snap.particles.position
        arr_polymer=snap.particles.typeid>1
        arr_gel=snap.particles.typeid<2
        polypos=pos[arr_polymer]
        gelpos=pos[arr_gel]
        polypos_x=polypos[:,0]
        gelpos_x=gelpos[:,0]

        for j in range(0,n_bin,1):
            N_poly=(polypos_x>sim_s+j*box_x) & (polypos_x<sim_s+(j+1)*box_x)
```

```
            poly_inN=polypos_x[N_poly]
            N_den_array[i,j] = len(poly_inN)/dV

            N_gel=(gelpos_x>sim_s+j*box_x) & (gelpos_x<sim_s+(j+1)*box_x)
            gel_inN=gelpos_x[N_gel]
            gel_den_array[i,j] = len(gel_inN)/dV

            box_mean_array[i,j] = sim_s+(j*box_x+((j+1)*box_x))/2

    results_density=np.asarray((box_mean_array.T,gel_den_array.T,N_den_array.T
)).T
    print(results_density.shape)
    samplearray = np.append(samplearray,[results_density],axis=0)

avarray = np.nanmean(samplearray,axis=0)
stdarray= np.nanstd(samplearray[:,:,:,1:],axis=0)

finresult =
np.asarray((avarray[:,:,0].T,avarray[:,:,1].T,avarray[:,:,2].T,stdarray[:,:,0]
.T,stdarray[:,:,1].T)).T
print(finresult.shape)
with
open('densityprofiles_polymerized_network_diffusive_Ndiff_'+str(Ntot)+'_vol_fr
ac'+str(volfrac)+'_densratio_'+str(truncate(float(denseratio)))+'_molefrac_'+s
tr(truncate(float(molefrac)))+'_kT_1.000.npy', 'wb') as f:
    np.save(f, finresult)

print("Programm done, File has been saved!")
```

python routine to analyze $R_{g\ perpendicular}$ and $R_{g\ parallel}$

```
import numpy as np
import gsd.hoomd
import freud
#import matplotlib.pyplot as plt
from tqdm import tqdm
from collections import defaultdict
import csv
import sys

Ntot = int(sys.argv[1])
samples = 11
n_bin = 50
data_jump = 1

################################################################################
## loading in csv dictionary
################################################################################
```

```
descriptorDict = defaultdict(list)

with open('description_file.csv', 'r') as data:

    csv_reader = csv.reader(data)
    rows = list(csv_reader)
for row in rows:
    descriptorDict[int(row[0])] = row[1]
a = descriptorDict[Ntot]
print(a)
v=a.strip('][').split(', ')

##############################################################################
## parameters
##############################################################################

volfrac = v[0]
molefrac = v[1]
denseratio = v[2]

##############################################################################
## functions
##############################################################################

def truncate(n):
    n = float(int(n * 100))
    n/= 100
    return n

##############################################################################
##############################################################################

datadummy =
gsd.hoomd.open(name='trajectory1_polymerized_network_diffusive_Ndiff_'+str(Nto
t)+'_vol_frac'+str(volfrac)+'_kT_1.000.gsd', mode='rb')


time=int(len(datadummy)/data_jump)
samplearray_perpen=np.empty((0,time,n_bin,2),dtype=float)
samplearray_para=np.empty((0,time,n_bin,2),dtype=float)


##############################################################################
## functions
##############################################################################

def Center_of_mass(poly_pos):
    arr_polymer_cm = np.nanmean(poly_pos,axis=1)
    return arr_polymer_cm
```

```
def Radius_of_Gyration(polystrands,polymer_Cms):
    cm_poly =
np.repeat((polymer_Cms),80,axis=0).reshape(len(polymer_Cms),80,3)
    y = np.power(np.linalg.norm((np.subtract(polystrands,cm_poly)),axis=2),2)
    x = np.power(((np.subtract(polystrands,cm_poly))),2)

    Rg = np.nanmean(y, axis = 1)
    Rg_xyz = np.nanmean(x,axis = 1)
    return Rg,Rg_xyz

def Rg_perpendicular(rg,rg_x):
    rg_per = (3*rg_x-rg)/(2*rg)
    return rg_per

def Rg_paralell(rg,rg_y,rg_z):
    rg_para = (((3*(rg_z+rg_y))/2)-rg)/(2*rg)
    return rg_para


##############################################################################
## loaded files
##############################################################################

for sample in tqdm(range(1,samples,1)):
    data_par =
gsd.hoomd.open(name='trajectory'+str(sample)+'_polymerized_network_diffusive_N
diff_'+str(Ntot)+'_vol_frac'+str(volfrac)+'_kT_1.000.gsd', mode='rb')


    print(len(data_par))

##############################################################################
##############################################################################

    Lx=data_par[0].configuration.box[0]
    Ly=data_par[0].configuration.box[1]
    Lz=data_par[0].configuration.box[2]


    sim_s= -(Lx/2)
    box_x=Lx/n_bin
    dV = box_x*Ly*Lz


    Av_Rg_perpen_array = np.zeros((int(len(data_par)/data_jump),n_bin))
    box_mean_array_perpen= np.zeros((int(len(data_par)/data_jump),n_bin))
    Av_Rg_para_array = np.zeros((int(len(data_par)/data_jump),n_bin))
    box_mean_array_para= np.zeros((int(len(data_par)/data_jump),n_bin))
```

```
    box = freud.box.Box(Lx=Lx,Ly=Ly,Lz=Lz)

    for frame in range(0,len(data_par),data_jump):

        i = int((frame-0)/data_jump)
        snap = data_par[frame]

        pos = snap.particles.position
        image =snap.particles.image
        real_pos = box.unwrap(pos,image)

        arr_polymer = snap.particles.typeid==2
        polypos = real_pos[arr_polymer]


        standLen = 80
        polystrand = polypos.reshape(int(len(polypos)/standLen),standLen,3)

        Cm_polymers = Center_of_mass(polystrand)

        #print(Cm_polymers)

        Cm_polymers_x=Cm_polymers[:,0]

        Radius_g,Rg_xyz = Radius_of_Gyration(polystrand,Cm_polymers)
        #print(Rg_xyz)
        Rg_x = Rg_xyz[:,0]
        Rg_y = Rg_xyz[:,1]
        Rg_z = Rg_xyz[:,2]
        #print(Rg_z)

        Rg_perpen = Rg_perpendicular(Radius_g,Rg_x)
        Rg_para = Rg_paralell(Radius_g,Rg_y,Rg_z)

        #print(Rg_para.shape)
        #print("space")
        #print(Rg_perpen.shape)


        for j in range(0,n_bin,1):
            N_poly=(Cm_polymers_x>(sim_s+j*box_x)) &
(Cm_polymers_x<(sim_s+(j+1)*box_x))
            Rg_perpen_in_bin=Rg_perpen[N_poly]
            Av_Rg_perpen_in_bin = np.nanmean(Rg_perpen_in_bin)
            Av_Rg_perpen_array[i,j] = Av_Rg_perpen_in_bin

            box_mean_array_perpen[i,j] = sim_s+(j*box_x+((j+1)*box_x))/2

            Rg_para_in_bin=Rg_para[N_poly]
```

```
            Av_Rg_para_in_bin = np.nanmean(Rg_para_in_bin)
            Av_Rg_para_array[i,j] = Av_Rg_para_in_bin

            box_mean_array_para[i,j] = sim_s+(j*box_x+((j+1)*box_x))/2



    results_Rg_perpen =
np.asarray((box_mean_array_perpen.T,Av_Rg_perpen_array.T)).T
    #print(results_Rg_perpen.shape)
    results_Rg_para = np.asarray((box_mean_array_para.T,Av_Rg_para_array.T)).T
    #print(results_Rg_para.shape)



    samplearray_perpen =
np.append(samplearray_perpen,[results_Rg_perpen],axis=0)
    samplearray_para = np.append(samplearray_para,[results_Rg_para],axis=0)

ava_array_perpen = np.nanmean(samplearray_perpen, axis = 0)
print(ava_array_perpen.shape)
#print(ava_array_perpen)
#print(ava_array_perpen[:,:,1])
ava_array_para = np.mean(samplearray_para, axis = 0)
print(ava_array_para.shape)
#print(ava_array_para)

#print(ava_array_perpen)
#print(ava_array_para.shape)

finresults =
np.asarray((ava_array_perpen[:,:,0].T,ava_array_perpen[:,:,1].T,ava_array_para
[:,:,1].T)).T
print(finresults.shape)

with
open('Rgperpendicular_Rgparalell_polymerized_network_diffusive_Ndiff_'+str(Nto
t)+'_vol_frac'+str(volfrac)+'_densratio_'+str(truncate(float(denseratio)))+'_m
olefrac_'+str(truncate(float(molefrac)))+'_kT_1.000.npy', 'wb') as f:
    np.save(f, finresults)

print("all done")
```

python routine used for the determination of the diffusion constants

```
import gsd.hoomd
import math
import freud
```

```
import sys
import math
import numpy
import random
import time as time1
from collections import defaultdict
import csv

Ntot = int(sys.argv[1])
samples = 11
#n_bin = 50
data_jump = 1

##############################################################################
## loading in csv dictionary
##############################################################################

descriptorDict = defaultdict(list)

with open('description_file.csv', 'r') as data:

    csv_reader = csv.reader(data)
    rows = list(csv_reader)
for row in rows:
    descriptorDict[int(row[0])] = row[1]
a = descriptorDict[Ntot]
v=a.strip('][').split(', ')

##############################################################################
## parameters
##############################################################################

volfrac = v[0]
molefrac = v[1]
denseratio = v[2]

##############################################################################
## functions
##############################################################################

def truncate(n):
    n = float(int(n * 100))
    n/= 100
    return n

########################################################################
###Set parameters
#######################################################################
#samples=6
```

```
##############################################################################
begining = time1.perf_counter()
dt = 0.001

#samples=int(sys.argv[1])
#Ntot = sys.argv[1]
#fraction = sys.argv[2]
#densratio = sys.argv[3]
#molefrac  = sys.argv[4]


kbT =1.0
cap_X_avg_list = []
cap_COM_avg_list = []
time_list=[]
period = 2e5

msd_sx=[]
msd_sy=[]
msd_sz=[]
msd_s=[]
dt=0.001
sample=1
filename =
'trajectory'+str(sample)+'_polymerized_network_diffusive_Ndiff_'+str(Ntot)+'_v
ol_frac'+str(volfrac)+'_kT_1.000.gsd'
#filename = "/media/tlinde01/TOSHIBA EXT/trajfiles/old
trajectory/trajectory"+str(sample)+"_diamond_network_diffusive"+"_Ntot_"+str(N
tot)+"_vol_frac"+str(fraction)+"_densratio_"+str(densratio)+"_molfrac_"+str(mo
lefrac)+"_kT_"+str(kbT)+".gsd"

traj=gsd.hoomd.open(name=filename, mode='rb')
#print(len(traj))
Lx=traj[0].configuration.box[0]
Ly=traj[0].configuration.box[1]
Lz=traj[0].configuration.box[2]
Lxby2 = Lx/2.0
Lyby2 = Ly/2.0
Lzby2 = Lz/2.0

box = freud.box.Box(Lx = Lx, Ly= Ly, Lz =Lz)

# Ny = int(Ly/sigma[0][0])
# poly_len = int(Lz/sigma[0][0])
# print(poly_len)

typeid =  numpy.copy(traj[0].particles.typeid)
N_remainz = numpy.count_nonzero(typeid == 2)
N_constraint = numpy.count_nonzero((typeid==0)|(typeid==1))
```

```
# Nx_remainz = int(N_remainz/2/Ny/poly_len)
cutoffx =2.0
lcutoffx =cutoffx
lengthx = int(Lxby2/lcutoffx)

lcx = Lxby2/lengthx

shiftx = int(lengthx)
cellnox= 2*lengthx
totalcell = cellnox
slcx = shiftx*lcx

count_A = numpy.empty(totalcell,dtype=int)
count_B = numpy.empty(totalcell,dtype=int)
count_AB = numpy.empty(totalcell,dtype=int)
bin_val = numpy.empty(totalcell,dtype=float)
#print(len(bin_val))
data1 = numpy.empty((0,len(bin_val),5),dtype=float)
cell=numpy.empty((0),dtype=float)
one=numpy.empty((0),dtype=int)
t=len(traj)
msd_frame = numpy.empty((0,totalcell),dtype=float)
delV = Ly*Lz*cutoffx
cols=totalcell
rows =t
#print(totalcell)
init1=749
for x in range(totalcell):
    bin_val[x] = (x+0.5)*lcutoffx-Lxby2

msd_samplebin = numpy.empty((0,totalcell,3),dtype=float)
msd_samplevar = numpy.empty((0,totalcell,3),dtype=float)
for sample in range(1,samples):
    filename =
'trajectory'+str(sample)+'_polymerized_network_diffusive_Ndiff_'+str(Ntot)+'_v
ol_frac'+str(volfrac)+'_kT_1.000.gsd'
    #filename =
"trajectory"+str(sample)+"_diamond_network_diffusive"+"_Ntot_"+str(Ntot)+"_vol
_frac"+str(fraction)+"_densratio_"+str(densratio)+"_molfrac_"+str(molefrac)+"_
kT_"+str(kbT)+".gsd"
    #print(filename)

    traj=gsd.hoomd.open(name=filename, mode='rb')
    Lx=traj[0].configuration.box[0]
    Ly=traj[0].configuration.box[1]
    Lz=traj[0].configuration.box[2]
    Lxby2 = Lx/2.0
    Lyby2 = Ly/2.0
    Lzby2 = Lz/2.0
```

```
    box = freud.box.Box(Lx = Lx, Ly= Ly, Lz =Lz)


    data1 = numpy.empty((0,len(bin_val),5),dtype=float)
    msd_bintime=numpy.empty((0,totalcell,3),dtype=float)
    for frame in range(init1,len(traj)-1):
        #print(frame)
        msd_bin=numpy.empty((0,3),dtype=float)
        container=[]

        msd_box=[]
        time = frame*dt*period

        posA=traj[frame].particles.position[:N_constraint]
        posB=traj[frame].particles.position[N_constraint:N_constraint+N_remain
z]
        imageB=traj[frame].particles.image[N_constraint:N_constraint+N_remainz
]
        posBplus_1=traj[frame+1].particles.position[N_constraint:N_constraint+
N_remainz]
        imageBplus_1=traj[frame+1].particles.image[N_constraint:N_constraint+N
_remainz]

        pos=traj[frame].particles.position
        count_A.fill(0)
        count_B.fill(0)
        count_AB.fill(0)

        xiB = ((slcx+posB[:,0])/lcx).astype(int)

        xiB=numpy.where(xiB<0,xiB+1,xiB)
        xiB=numpy.where(xiB==cellnox,xiB-1,xiB)


        mB=xiB[:]

        for x in range(totalcell):
            #print(x)
            ids=numpy.where(mB==x)
            ids=numpy.unique(ids[0])

            posx=numpy.empty((0,len(ids),3),dtype=float)
            posy=numpy.empty((0,len(ids),3),dtype=float)
            posz=numpy.empty((0,len(ids),3),dtype=float)

            posx=numpy.append(posx,[numpy.take(posB,ids,axis=0)],axis=0)
            posx=numpy.append(posx,[numpy.take(posBplus_1,ids,axis=0)],axis=0)
            posx[:,:,1:3]=0.
```

```
            posz=numpy.append(posz,[numpy.take(posB,ids,axis=0)],axis=0)
            posz=numpy.append(posz,[numpy.take(posBplus_1,ids,axis=0)],axis=0)
            posz[:,:,0]=0.
            posz[:,:,1]=0.

            posy=numpy.append(posy,[numpy.take(posB,ids,axis=0)],axis=0)
            posy=numpy.append(posy,[numpy.take(posBplus_1,ids,axis=0)],axis=0)
            #print(posy)
            posy[:,:,0]=0.
            posy[:,:,2]=0.


            """
            if posx.size==0:

                posx=numpy.empty((0,len(posB),3),dtype=float)
                posx=numpy.append(posx,[posB],axis=0)
                posx=numpy.append(posx,[posB],axis=0)
            """
            imagex=numpy.empty((0,len(ids),3),dtype=int)
            imagey=numpy.empty((0,len(ids),3),dtype=int)
            imagez=numpy.empty((0,len(ids),3),dtype=int)
            imagex=numpy.append(imagex,[numpy.take(imageB,ids,axis=0)],axis=0)
            imagex=numpy.append(imagex,[numpy.take(imageBplus_1,ids,axis=0)],a
xis=0)

            imagey=numpy.append(imagey,[numpy.take(imageB,ids,axis=0)],axis=0)
            imagey=numpy.append(imagey,[numpy.take(imageBplus_1,ids,axis=0)],a
xis=0)

            imagez=numpy.append(imagez,[numpy.take(imageB,ids,axis=0)],axis=0)
            imagez=numpy.append(imagez,[numpy.take(imageBplus_1,ids,axis=0)],a
xis=0)

            """
            if imagex.size==0:

                imagex=numpy.empty((0,len(imageB),3),dtype=int)
                imagex=numpy.append(imagex,[imageB],axis=0)
                imagex=numpy.append(imagex,[imageB],axis=0)
            """

            imagex[:,:,1:3]=0
            imagez[:,:,0:2]=0
            imagey[:,:,0]=0
            imagey[:,:,2]=0

            real_pos=numpy.array([Lx,Ly,Lz])*imagex+posx
```

```
            real_posy=numpy.array([Lx,Ly,Lz])*imagey+posy
            real_posz=numpy.array([Lx,Ly,Lz])*imagez+posz
            #print(real_posz[1,:]-real_posz[0,:])
            msdx=numpy.nanmean(numpy.power((real_pos[1,:]-
real_pos[0,:]),2),axis=0)
            msdy=numpy.nanmean(numpy.power((real_posy[1,:]-
real_posy[0,:]),2),axis=0)
            msdz=numpy.nanmean(numpy.power((real_posz[1,:]-
real_posz[0,:]),2),axis=0)
            msd_bin=numpy.append(msd_bin,[numpy.asarray((msdx[0],msdy[1],msdz[
2]))],axis=0)
            #print(msdx[0],msdy[0],msdz[0])
            #print(msd_bin.shape,totalcell,msdx[0])
        msd_bintime=numpy.append(msd_bintime,[msd_bin],axis=0)

    msd_samplebin=numpy.append(msd_samplebin,[numpy.nanmean(msd_bintime,axis=0
)],axis=0)
    msd_samplevar =
numpy.append(msd_samplevar,[numpy.nanvar(msd_bintime,axis=0)],axis=0)
data9 =
numpy.asarray((msd_samplebin[:,:,0].T,msd_samplebin[:,:,1].T,msd_samplebin[:,:
,2].T,msd_samplebin[:,:,0].T/(2*period*dt),msd_samplebin[:,:,1].T/(2*period*dt
),msd_samplebin[:,:,2].T/(2*period*dt))).T
data10=
numpy.asarray((msd_samplevar[:,:,0].T,msd_samplevar[:,:,1].T,msd_samplevar[:,:
,2].T,msd_samplevar[:,:,0].T/(2*period*dt),msd_samplevar[:,:,1].T/(2*period*dt
),msd_samplevar[:,:,2].T/(2*period*dt))).T

#print(data9.shape)

#data = numpy.nanmean(msd_samplebin,axis=0)
data = numpy.nanmean(data9,axis=0)
#datastd = numpy.nanstd(msd_samplebin,axis=0)
#datastd = numpy.nanstd(data9,axis=0)
datastd = numpy.sqrt(1/(numpy.nansum(data10,axis=0)))
#print(datastd.shape,data.shape)
#exit()
#print(len(bin_val),len(msd_samplebin[:]))
#data1 =
numpy.array((bin_val,data[:,0],data[:,1],data[:,2],data[:,0]/(2*period*dt),dat
a[:,1]/(2*period*dt),data[:,2]/(2*period*dt))).T
#data2 = numpy.concatenate((data1,datastd[:,1:]),axis=1)

bin_val = bin_val.reshape(totalcell,1)
data2 = numpy.concatenate((bin_val,data,datastd),axis=1)

#print(data2.shape,bin_val.shape)

#print(data1)
```

```
#with open('/media/tlinde01/TOSHIBA EXT/trajfiles/old
trajectory/Bond_vector_polymerized_network_diffusive_Ndiff_'+str(Ntot)+'_vol_f
rac'+str(volfrac)+'_densratio_'+str(truncate(float(denseratio)))+'_molefrac_'+
str(truncate(float(molefrac)))+'_kT_1.000.npy', 'wb') as f:

filename3
='Monomer_Positiondep_diffusionconst_vs_xbox_Ndiff_'+str(Ntot)+'_vol_frac'+str
(volfrac)+'_densratio_'+str(truncate(float(denseratio)))+'_molefrac_'+str(trun
cate(float(molefrac)))+'_kT_1.000.npy'
#filename3 =
"Monomer_Positiondep_diffusionconst_vs_xbox"+"_diamond_network_diffusive"+"_Nt
ot_"+str(Ntot)+"_vol_frac"+str(fraction)+"_densratio_"+str(densratio)+"_molfra
c_"+str(molefrac)+"_kT_"+str(kbT)+".txt"
with open(filename3, 'wb') as f2:
    numpy.save(f2, data2)

end = time1.perf_counter()
print("Programm done")
print(abs(end-begining))
```

A3 Supporting Information to Project III

python routine used to cut videos

```
## Used in Visual studio code ###

import cv2
from tqdm import tqdm
import numpy as np


def Time_to_frame (vidtime,vidfps):
    vidframe =int(vidfps*vidtime)
    return vidframe

def Frame_to_time (vidframe,vidfps):
    vidtime_raw=float(vidframe/vidfps)
    vidtime=float(f'{vidtime_raw:.2f}')
    return vidtime

videos = ('V1','V2','V3','V4','V5','V6','V7','V8') ## Listing of videos to be
cut
t_a_10=(0.976,0.976,0.976,0.976,0.976,0.975,0.976,0.976) ## time in video
after 10 frames
startingtimes= (5.759,7.517,13.762,8.199,6.345,8.003,8.101,7.613) ## start
time at which cutting of frames starts

videoexperiment = input('What is the experiment Name? ') ## Experiment name
videotemp = input('What is the video temperature? ') ## Temperature of
swelling solution

for i in tqdm(range(0,len(videos),1)):
    j = videos[i]
    print (j)
    video = cv2.VideoCapture('Kinetik_Mikrogele/videos/'+j+'.avi')

    width  = int(video.get(cv2.CAP_PROP_FRAME_WIDTH))
    height = int(video.get(cv2.CAP_PROP_FRAME_HEIGHT))
    frames = int(video.get(cv2.CAP_PROP_FRAME_COUNT))
    fps    = int(video.get(cv2.CAP_PROP_FPS))

    video.release()

    print('Video Parameters: ')
    print('width: ',width,'height: ', height,'frames: ', frames, 'fps: ',fps)

    videonumber = j
    fps_raw=(10/t_a_10[i])
    fps=float(f'{fps_raw:.3f}')
```

```
    times = startingtimes[i]


    cap =cv2.VideoCapture('Kinetik_Mikrogele/videos/'+j+'.avi')

    count=0
    end = Time_to_frame(times,fps) # start of the frame you want to save
    start=int(end-25) # end frame number
    end1=100
    end2=200
    end3=250
    end4=1000
    end5=2000
    end6=3600

    Times_saved=np.empty(0,dtype=float)

    #print(Times_saved)

    while(cap.isOpened()):
        ret,frame =cap.read()
        #print('i am here')
        if ret==False:
            break
        if count>start and count<=end:
            #print('A')
            vtime = Frame_to_time(count,fps)
            cv2.imwrite(f'Kinetik_Mikrogele/timecuts/'+j+'/'+videoexperiment+'
_'+videotemp+'_kinetik_'+videonumber+'_'+str(vtime)+'.jpg', frame)
            Times_saved=np.append(Times_saved,[vtime], axis=0)
        if count>end and count<=end1 and count%2==0:
            #print('B')
            vtime = Frame_to_time(count,fps)
            cv2.imwrite(f'Kinetik_Mikrogele/timecuts/'+j+'/'+videoexperiment+'
_'+videotemp+'_kinetik_'+videonumber+'_'+str(vtime)+'.jpg', frame)
            Times_saved=np.append(Times_saved,[vtime], axis=0)
        if count>end1 and count<=end2 and count%5==0:
            #print('B')
            vtime = Frame_to_time(count,fps)
            cv2.imwrite(f'Kinetik_Mikrogele/timecuts/'+j+'/'+videoexperiment+'
_'+videotemp+'_kinetik_'+videonumber+'_'+str(vtime)+'.jpg', frame)
            Times_saved=np.append(Times_saved,[vtime], axis=0)
        if count>end2 and count<=end3 and count%10==0:
            #print('B')
            vtime = Frame_to_time(count,fps)
            cv2.imwrite(f'Kinetik_Mikrogele/timecuts/'+j+'/'+videoexperiment+'
_'+videotemp+'_kinetik_'+videonumber+'_'+str(vtime)+'.jpg', frame)
            Times_saved=np.append(Times_saved,[vtime], axis=0)
        if count>end3 and count<=end4 and count%50==0:
```

```
            #print('B')
            vtime = Frame_to_time(count,fps)
            cv2.imwrite(f'Kinetik_Mikrogele/timecuts/'+j+'/'+videoexperiment+'
_'+videotemp+'_kinetik_'+videonumber+'_'+str(vtime)+'.jpg', frame)
            Times_saved=np.append(Times_saved,[vtime], axis=0)
        if count>end4 and count<=end5 and count%100==0:
            #print('B')
            vtime = Frame_to_time(count,fps)
            cv2.imwrite(f'Kinetik_Mikrogele/timecuts/'+j+'/'+videoexperiment+'
_'+videotemp+'_kinetik_'+videonumber+'_'+str(vtime)+'.jpg', frame)
            Times_saved=np.append(Times_saved,[vtime], axis=0)
        if count>end5 and count<=end6 and count%200==0:
            #print('B')
            vtime = Frame_to_time(count,fps)
            cv2.imwrite(f'Kinetik_Mikrogele/timecuts/'+j+'/'+videoexperiment+'
_'+videotemp+'_kinetik_'+videonumber+'_'+str(vtime)+'.jpg', frame)
            Times_saved=np.append(Times_saved,[vtime], axis=0)
        if count>end6:
            break
        count+=1
        #print(count)



    cap.release()
    cv2.destroyAllWindows()
    np.savetxt("Kinetik_Mikrogele/timecuts/"+j+"/Times_saved_"+j+"_"+videotemp
+".txt", Times_saved)


    print(Times_saved.shape)

print ('Program is done!')
```

Fitting Parameters of the averaged swelling data of the particles crosslinked with MBAA

Parameter	10 °C	25 °C	45 °C	65 °C	85 °C
A	1,49	1,43	1,63	1,44	1,34
$\boldsymbol{\tau_1}$	12,78	9,36	6,83	0,56	0,49
B	1,07	1,09	1,25	1,50	1,35
$\boldsymbol{\tau_2}$	0,97	0,57	0,02	5,43	4,31

Fitting Parameters of the averaged swelling data of the particles crosslinked with EBAA

Parameter	**10 °C**	**25 °C**	**45 °C**	**65 °C**	**85 °C**
A	1,60	1,46	1,50	1,51	1,51
$\boldsymbol{\tau_1}$	1,33	0,70	0,89	6,09	5,24
B	1,45	1,49	1,45	1,28	1,33
$\boldsymbol{\tau_2}$	15,15	10,44	8,24	0,02	0,02

Fitting Parameters of the averaged swelling data of the particles crosslinked with PBAA

Parameter	**10 °C**	**25 °C**	**45 °C**	**65 °C**	**85 °C**
A	1,55	1,65	1,20	1,54	1,54
$\boldsymbol{\tau_1}$	11,57	0,81	6,58	0,81	0,81
B	1,30	1,04	1,54	1,23	1,23
$\boldsymbol{\tau_2}$	1,16	8,19	0,71	5,65	5,65

Fitting Parameters of the averaged swelling data of the particles crosslinked with BBAA

Parameter	**10 °C**	**25 °C**	**45 °C**	**65 °C**	**85 °C**
A	1,75	1,64	1,19	1,55	1,15
$\boldsymbol{\tau_1}$	9,90	7,25	0,37	4,22	0,45
B	1,07	1,13	1,56	1,21	0,97
$\boldsymbol{\tau_2}$	0,89	0,02	5,44	0,01	4,06

Curriculum Vitae

[redacted]